

QUANTITATIVE MICROANALYSIS TECHNIQUES
FOR MAGNETIC NANOSTRUCTURES

by

KAREN TORRES HENRY

A DISSERTATION

Submitted in partial fulfillment of the requirements
for the degree of Doctor of Philosophy
in the Department of Metallurgical Engineering
in the Graduate School of
The University of Alabama

TUSCALOOSA, ALABAMA

2010

Copyright Karen Torres Henry 2010
ALL RIGHTS RESERVED

ABSTRACT

Microanalysis techniques are used to characterize magnetic nanostructures. To advance these materials in many applications, it is necessary to understand the microstructure. For example, subtle compositional fluctuations within a nanostructure can significantly influence the material properties. In this work, microanalysis techniques have been used to quantify composition, volume fraction, and long-range order parameter in magnetic nanostructures. A methodology for determining an optimal voxel dimension range was developed using a model system for the experimentally collected atom probe tomography data. The influence of voxel dimension on volume fraction and composition of chemically partitioned phases is examined.

Atom probe tomography is used to understand the influence of Pt enrichment at grain boundaries in the A1 to $L1_0$ polymorphic phase transformation. The Pt enrichment at grain boundaries in atom probe tomography analysis provides experimental verification of modeling predictions of Pt surface segregation. It is also observed that upon phase transformation to $L1_0$, the Pt grain boundary enrichment decreased. Field ion microscopy and atom probe tomography is used to evaluate the field evaporation behavior of (001) planes in ordered FePt. Both experimental and simulation results have shown that the difference in evaporation field between the two components of the alloy contributed to the trajectory aberrations near the (002) pole and zone axes. The model system shows that chemical order within a structure introduces aberrations in the reconstruction of the atomic planes limiting the spatial and chemical fidelity of characterizing such structures using current reconstruction methodologies.

Finally, a comparison of the experimental results to simulations is used to assess the viability of electron diffraction in the quantification of S in FePt thin films and nanoparticles. A multislice approach was used to simulate CBED patterns of FePt films with various thicknesses, compositions, orientations, and S values. In general, electron diffraction provides a technique to determine order parameter of small volumes with the implementation of multislice simulations.

DEDICATION

This dissertation is dedicated to my husband, family, and close friends who helped and encouraged me throughout the creation of this manuscript.

LIST OF ABBREVIATIONS AND SYMBOLS

α	Semi-convergence angle
APT	Atom probe tomography
bct	body-center tetragonal
CBED	Convergent-beam electron diffraction
C_i	Concentration of selected ion
C_s	Spherical aberration coefficient
C_x^0	Global concentration of element X
C_x^m	Concentration of element X in matrix
C_x^n	Concentration of element X in nanocrystal
ΔC_f	Length of composition profile
FIB	Focus ion beam
FIM	Field ion microscopy
f_v^x	Volume fraction of element X
IVAS	Imago's visualization and analysis software
k_b	Boltzmann's constant
K_u	Uniaxial magnetocrystalline anisotropy
N_b	Number of ions per voxel
N_i	Number of ions i
N_t	Total number of ions in selected volume
r_α	Fraction of A type lattice sites occupied by A
r_β	Fraction of B type lattice sites occupied by B

σ	Standard error for concentration
σ_c	Standard error for counting statistics
σ_e	Standard error within a voxel
S	Long-range order parameter
SAED	Selected area electron diffraction
SDM	Spatial distribution map
STEM	Scanning transmission electron microscopy
T	Temperature
TEM	Transmission electron microscopy
V	Volume
x_α	atom fraction of element A
x_β	atom fraction of element B
XRD	X-ray diffraction
y_α	Fraction of A lattice sites
y_β	Fraction of B lattice sites

ACKNOWLEDGMENTS

I would like to take this opportunity to thank my colleagues, friends, and faculty members who have helped me with this research project. I would like to express my deepest gratitude to Dr. Gregory Thompson, the chairman of this dissertation, for sharing his expertise regarding quantitative microanalysis techniques. The author would also like to thank him for the guidance and support during the completion of this dissertation. I am also grateful to the members of my committee, Dr. Viola Acoff, Dr. Gregg Janowski, Dr. Gary Mankey, and Dr. Mark Weaver for their input and interest in this research project.

A portion of this research was possible through the use of the National Synchrotron Light Source at Brookhaven National Laboratory. The author would like to thank Dr. Jean Jordan-Sweet for her collaboration efforts at Brookhaven. Likewise, the author would like to thank Dr. Claudiu Muntele for scientific and technical support at the Center for Irradiation of Materials at Alabama A&M University. Sincere thanks to Drs. Michael Moody and Simon Ringer at the Australia Center for Microscopy and Microanalysis at the University of Sydney New South Wales, Australia for providing fruitful discussions. The author would like to thank Brian Geiser at Imago Scientific Instruments for helpful discussions. Lastly, the author would like to express her appreciation for the collaboration and help received from Dr. Richard Vanfleet at Brigham Young University.

Sincere thanks to the members of my research group. They have truly made the journey more enjoyable. I would also like to thank the staff of the Central Analytical Facility at the University of Alabama for the many hours spent training and helping me with the microscopes.

A special thanks to my husband Patrick for his support and encouragement. I am most thankful to my family for their constant encouragement and help during this time.

This research was supported by the National Science Foundation (NSF) under grant NSF-DMR05-29369. As well as the University of Alabama and the IMI program of the National Science Foundation under grant NSF-DMR04-09848.

CONTENTS

ABSTRACT.....	ii
DEDICATION.....	iv
LIST OF ABBREVIATIONS AND SYMBOLS	v
ACKNOWLEDGMENTS	vii
LIST OF TABLES	xi
LIST OF FIGURES	xii
CHAPTER 1 INTRODUCTION	1
1.1 Motivation	1
1.2 Chemically partitioned soft magnetic ribbons.....	2
1.3 The A1 to $L1_0$ polymorphic phase transformation	3
1.4 Dissertation Organization.....	5
CHAPTER 2 THE INFLUENCE OF VOXEL SIZE ON ATOM PROBE TOMOGRAPHY DATA	6
CHAPTER 3 GRAIN BOUNDARY ENRICHMENT IN THE FEPT POLYMORPHIC A1 TO $L1_0$ PHASE TRANSFORMATION	21
CHAPTER 4 FIELD EVAPORATION BEHAVIOR IN [001] FEPT THIN FILMS	36
CHAPTER 5 DYNAMICAL DIFFRACTION SIMULATIONS IN CHEMICALLY ORDERED FEPT	51

CHAPTER 6 COMPARISON OF SIMULATED AND EXPERIMENTAL ORDER PARAMETERS IN FEPT	66
CHAPTER 7 CONCLUSIONS AND FUTURE WORK.....	84
7.1 Data binning in atom probe tomography.....	84
7.2 Grain boundary enrichment.....	85
7.3 Field evaporation behavior of [001] FePt.....	85
7.4 Electron diffraction order parameter determination.....	86
REFERENCES	88
APPENDICES	91
APPENDIX A: MULTISLICE SIMULATION GUIDE.....	92
APPENDIX B: EXPERIMENTAL CBED PATTERNS.....	97
APPENDIX C: ATOM PROBE TOMOGRAPHIC RECONSTRUCTIONS.....	103

LIST OF TABLES

2. 1	Results of composition and volume fraction for the analysis of the Co-Fe model system. The error given was associated with the number of ions within a given voxel.....	11
2. 2	Compositional results from the APT experimental analysis.....	16
2. 3	Volume fraction, ions per voxel, and error results from the experimental analysis of APT. The error given is associated with the number of ions within a given voxel.....	16
3. 1	Summary of the times, temperatures, c/a ratios, and order parameters for the samples presented.	25
3. 2	Summary of the average grain boundary Pt concentration for Fe _{54+/-1} Pt _{46+/-1} thin films analyzed in the atom probe.	27
5. 1	The influence of pixel size on CPU time for 4 nm and 20 nm films. Simulations were performed on a 32 bit system with an Intel Atom processor.	60
6. 1	The nominal compositions and thicknesses for the FePt films used in this study. The substrate temperature, T _s , the <i>ex situ</i> annealing temperature, T _A and time were also tabulated.	68
C.1	The x- and y- coordinates for each pole identified from the detector event histogram. The distance and angle between pole 1 and the other poles are also tabulated.....	105
C.2	The plane spacing for each pole using the initial values for ICF and <i>K</i> are tabulated. The pole combination used for this sample is also provided. The theoretical angle between the 002 pole and each pole identified is given along with the new calculated ICF value.....	106
C.3	The d-spacing observed using the new ICF value of 1.43 and corresponding <i>K</i> is tabulated along with the theoretical value for the pole.	107

LIST OF FIGURES

2.1	A proximity histogram of Co and Fe in the sample with respect to the Fe 7 atomic percent isoconcentration surface. The bin size was 0.1 nm. The calculation was made over a volume 30 nm x 30 nm x 60 nm and includes 54 crystallites	10
2.2	The length of the composition profile, ΔC_f , plotted as a function of ion count.....	12
2.3	Results of composition, volume fraction, and ion count for the Co-Fe model system. The highlighted band is the optimal range for voxel edge length in the system consisting of 8 nm diameter crystals.	13
2.4	(a) Fe atom map. (b) Hf atom map. (c) Zr atom map.....	14
2.5	(a) Proximity histogram of Fe with respect to the 6 atomic percent Fe isoconcentration surface. The bin size was 0.1 nm. (b) Isoconcentration surfaces of 6 atomic percent Fe isolating the crystallite phase.....	14
2.6	(a) Diffraction pattern used for dark field imaging. (b) Compiled micrograph using Image J software of all dark field images.....	17
3.1	(a) <i>In-situ</i> micromanipulator tungsten-needle attached to an atom probe micro-tip. The base of the tip is subsequently FIB milled to liberate the tip from the base. (b) Attachment of the FIB cut-out/lift-out tip to a TEM grid. <i>In-situ</i> Pt-deposition from the FIB provided the adhesion material between the tip and grid. (c) FIB removal of the micro-tip from tungsten-needle (d) TEM image of an as-deposited tip.....	27
3.2	(a) XRD scans of the as-deposited $Fe_{54\pm 1}Pt_{46\pm 1}$ thin film and $Fe_{54\pm 1}Pt_{46\pm 1}$ thin films annealed for 1 minute. The asterisk indicates a peak associated with the glass slide used to hold the sample for XRD (b) Electron diffraction pattern of the $Fe_{54\pm 1}Pt_{46\pm 1}$ thin film annealed at 400°C for 1 minute.....	29
3.3	A one-dimensional concentration profile through a grain boundary in (a) the as-deposited $Fe_{54\pm 1}Pt_{46\pm 1}$ thin film and (b) the $Fe_{54\pm 1}Pt_{46\pm 1}$ thin film annealed at 400°C for 1 minute. The solid red line is Fe and the dotted green line is Pt. A Pt atom map indicating the analysis direction and grain boundary used for (c) the as-deposited $Fe_{54\pm 1}Pt_{46\pm 1}$ thin film viewed in-plane and (d) the $Fe_{54\pm 1}Pt_{46\pm 1}$ thin film annealed at 400°C for 1 minute viewed in cross-section. The strips are the high density variations along the columnar grain boundaries. (e) Under- and over-focused in-plane TEM images of the as-deposited thin film. The white arrows indicate the grain boundary. The defocus length was +/- 1.11 μm	30

3.4	(a) XRD scans of the as-deposited $\text{Fe}_{54\pm 1}\text{Pt}_{46\pm 1}$ thin film and $\text{Fe}_{54\pm 1}\text{Pt}_{46\pm 1}$ thin films annealed for 30 minutes. (b) XRD scans of the as-deposited $\text{Fe}_{54\pm 1}\text{Pt}_{46\pm 1}$ thin film and $\text{Fe}_{54\pm 1}\text{Pt}_{46\pm 1}$ thin films annealed for 100 minutes.	31
3.5	A one-dimensional concentration profile through a grain boundary in (a) the $\text{Fe}_{54\pm 1}\text{Pt}_{46\pm 1}$ thin film annealed at 400°C for 30 minutes and (b) the $\text{Fe}_{54\pm 1}\text{Pt}_{46\pm 1}$ thin film annealed at 350°C for 100 minutes. The solid red line is Fe and the dotted green line is Pt. A Pt atom map indicating the analysis direction and grain boundary used for (c) the $\text{Fe}_{54\pm 1}\text{Pt}_{46\pm 1}$ thin film annealed at 400°C for 30 minutes viewed in plane and (d) the $\text{Fe}_{54\pm 1}\text{Pt}_{46\pm 1}$ thin film annealed at 350°C for 100 minutes viewed in cross-section. The strips are the high density variations along the columnar grain boundaries.....	32
3.6	A one-dimensional concentration profile through a grain boundary in (a) the film annealed at 600°C for 30 minutes and (b) the film annealed at 400°C for 100 minutes. The solid red line is Fe and the dotted green line is Pt. A Pt atom map indicating the analysis direction and grain boundary used for (c) the $\text{Fe}_{54\pm 1}\text{Pt}_{46\pm 1}$ thin film annealed at 600°C for 30 minutes viewed in plane and (d) the $\text{Fe}_{54\pm 1}\text{Pt}_{46\pm 1}$ thin film annealed at 400°C for 100 minutes viewed in cross-section. The strips are the high density variations along the columnar grain boundaries.....	33
4.1	(a) Fe atom map showing depletion at the (002) pole and the zone axes. (b) APT analysis of FePt film along the [001]-direction.....	40
4.2	(a) Total number of atoms as a function of radial distance from the (002) pole. (b) Fe concentration as a function of radial distance away from the pole.....	41
4.3	(a) Fe atom map with sharp planes observed. (b) Pt atom map with blurred planes observed. (c) 1-D composition profile along the ordered direction. Fe is depicted in red and Pt is depicted in green.	42
4.4	Spatial distribution maps from an 8 nm diameter region centered at the (002) pole. (a) The SDM shows the z-distance from Pt to Pt planes using a solid black line and Fe to Fe planes in a dashed black line. (b) The z-distances of Pt planes with respect to Fe atoms.....	43
4.5	FIM images of the (002) FePt pole at (a) 30K, (b) 50K, (c) 70K, (d) 90K, (e) 110K. Only the Pt atoms are imaged in these micrographs.....	44
4.6	(a) Initial tip shape with the first 3000 atoms evaporated highlighted in black. (b) Final tip shape with the last 3000 atoms evaporated highlighted in black. (c) FIM image after field evaporation demonstrating faceting of the tip surface.....	45

4.7	(a) Image of the high evaporation field species (Pt) in an ordered alloy. (b) Same image obtained for the low evaporation field species (Fe). The images exhibit bright lines within the zone axes. Also note the low atomic density at the (002) pole.....	47
4.8	The evaporation sequence of an atomic terrace. The low evaporation atoms (Fe) are shown in grey and the high evaporation atoms (Pt) are shown in black. The grey (Fe) atoms are shown to exhibit the crystal structure and are located below the black (Pt) atoms. Evaporated Pt atoms are represented by black squares. (a) The twelve Pt atoms on the atomic terrace. (b) Four corner atoms have been removed from the terrace. (c) Four kink site atoms have been removed from the terrace. (d) Final Pt atom after 3 kink site Pt atoms were evaporated.....	47
4.9	(a) 3D reconstruction of FePt obtained from simulated trajectories. Approximately 20 atomic (001) planes were evaporated. The high evaporation atoms (Pt) are shown in green and the low evaporation atoms (Fe) are shown in red. (b) An experimental reconstruction of FePt. The image exhibits the same aberrations as simulations.....	48
5.1	Intensity of the superlattice (110) and fundamental (220) reflections vs. thickness for an order parameter of 0.5 in the (a) [001] orientation and (b) [111] orientation.	53
5.2	A CBED configuration with a convergence angle 2α . The diameter of the disk is a and b is the 2θ angle between the central disk and a specified reflection.....	54
5.3	[001] orientation viewed in cross-section to demonstrate the flat layers along the z-direction which is parallel to the optic axis.	56
5.4	(a) (111) planes are aligned perpendicular to the optic axis. The atoms in-depth do not line up. Fe atoms are represented by the unfilled circles and Pt atoms are represented by the solid circles. (b) The crystal is tilted 90 degrees. The layers are flat along the optic axis in this orientation. (c) The [111] direction is aligned with the optic axis and atoms lineup in-depth. (d) The crystal is tilted 90 degrees which reveals the layers are not flat along the optic axis.....	57
5.5	CBED patterns for accelerating voltages at (a) 120 keV (b) 160 keV (c) 200 keV and (d) 300 keV. The convergence angle is 8 mrad for all images. The disks significantly overlap in Figure 5(d).....	58
5.6	Intensity ratio as a function of S. Three compositions for a 4 nm film are shown.....	61
5.7	The intensity ratio as a function of S for a 20.4 nm film. The optic axis was aligned with either the {111} plane normal or <111> direction. Oscillations were observed in the shape of the curve for the <111> direction. The shape of the curve was monotonic in nature with alignment of the optic axis with the <111> direction.....	62

5.8	Trends of thermal configurations for $S= 0.2, 0.5,$ and 0.9 for a 7.2 nm film thickness....	63
6.1	STEM image of intact regions of FePt film surrounded by the MgO substrate. The MgO windows are etched with hot phosphoric acid.....	69
6.2	(a) CBED patterns with overlapping disks where the semi-convergence angle was greater than 4 mrad. (b) CBED patterns without overlapping disks with a semi-convergence angle of 4 mrad.....	71
6.3	The Si-K line and Pt-L line plotted as a function of distance. The Si-K was plotted with a solid line and the Pt-L line was plotted with a dashed line.....	71
6.4	Intensity ratio as a function thickness for the $[001]$ orientation and $S=0.3$	74
6.5	The Experimental CBED patterns for (a) specimen A and (b) specimen B. The intensity ratio as a function of S for (c) specimen A and (d) specimen B. The dashed line indicates the experimentally obtained intensity ratio for the specimen. The curves were determined by multislice simulations.....	75
6.6	The simulated CBED patterns for (a) specimen A at $S=0.2$ and (b) specimen B at $S=0.4$	75
6.7	Intensity ratio as a function of S , determined by multislice simulation, for specimens C and D. Three film thicknesses close to the film thickness are shown to account for error in measurement. The horizontal lines correspond to experimentally obtained intensity ratios.	77
6.8	An experimental CBED pattern for (a) specimen C and (b) specimen D.....	77
6.9	Possible slicing schemes for the (111) orientation. (a) The optic axis is aligned with the $[111]$ direction. Note the atoms align in-depth for this orientation. However, the atomic layers are tilted. (b) The optic axis is aligned perpendicular to the (111) planes. The atomic layers are flat along the optic axis. However, the atoms do not align in-depth.....	79
6.10	The intensity ratio as a function of S for specimen E with the optic axis (a) along the $[111]$ direction and (b) perpendicular to the (111) planes.....	79
6.11	The intensity ratio as a function of S for (a) specimen F and (b) specimen G. The curves were determined by multislice simulations.....	80
6.12	(a) The experimental SAED pattern for specimen F. The pattern included reflections from the FePt film and MgO substrate. (b) The experimental SAED pattern for specimen G with reflections from the FePt film and Si substrate.....	81

B.1	The STEM button is highlighted in yellow. This button is toggled to activate and deactivate STEM mode in the Tecnai F20.....	98
B.2	(a) Proper alignment of the probe with the hot spot located at the center of the circular halo. (b) An example of a misaligned aperture. The illuminated halo is symmetric. (c) Another example of a misaligned aperture. The probe is astigmatic with a circular halo.....	99
B.3	An example of aCBED pattern where the reflection disks overlap.....	99
B.4	The flap-out tab is used to change the operating conditions from standard to non-standard. Under the focus tab, the Intensity & Objective focus is selected for non-standard operation.....	100
B.5	The STEM detector tab is controls the insertion and removal of the HAADF detector. The button highlighted in yellow is toggled to perform this process. The camera length can also be changed in this tab.....	101
C.1	The detector event histogram for an Al specimen. The region highlighted in red will allow a user to unsample the data. This will display all events detected during acquisition. The region highlighted in blue displays the x- and y-coordinates of the cursor position.....	104
C.2	A diagram of the poles where the x- and y- coordinates were identified	104
C.3	Step 7 of 8 display with the reconstruction explorer highlighted by the red box.....	105
C.4	The z-SDM for an ICF value of 1.65 and a value of 3.3 for <i>K</i> . The spacing for Pole 1 is 0.135 nm for these reconstruction values.....	106
C.5	The final SDM for the (002) pole using a value of 1.43 for ICF and 3.35 for <i>K</i>	108
C.6	The figure is an extracted cube from the (002) pole to illustrate the visualization of planes at the (002) pole.....	108

CHAPTER 1

INTRODUCTION

1.1 Motivation

The characterization of nanostructured materials in an effort to improve the magnetic performance by controlling the microstructure has been a research interest in recent years [1-11]. Magnetic properties are a function of grain size, composition, and crystal structure. Subtle compositional fluctuations within a nanostructure can significantly influence the material properties. Thus, quantifying compositional fluctuations at the atomic-scale is essential in understanding the structure-property relationship. The focus of this work was to assess the viability of several microanalysis techniques for quantification of composition and order parameter in nanoscale materials.

Atom probe tomography (APT) has the spatial resolution to detect slight variations experimentally and provide a quantitative assessment for nanoscale features [12]. An atom probe experiment generates both spatial coordinates and the mass-to-charge-state ratio for chemical identification. A reconstructed rendering of the analyzed volume can be produced from the raw data using a 3D visualization software package. Features such as interfaces and precipitates can be easily observed. With recent advances in larger area detectors [12], APT can be used to quantify cluster size, composition, and volume fraction because of the larger number of atoms collected [2, 13-14].

Magnetic properties can also be influenced by the degree of chemical order. To chemically order a material from a disordered to an ordered state, atoms must physically diffuse from random lattice sites to specific lattice sites. The degree of order depends upon the number of atoms occupying the correct lattice sites which can be described by the order parameter, S [15]. Quantifying long-range order parameter is necessary in understanding the magnetic properties of many intermetallic systems such as FePt, CoPt, AlMn, and FePd. In these intermetallics, the high uniaxial magnetocrystalline anisotropy, K_u , is only obtained when the material is chemically ordered [16-18]. Order parameter can be determined by a number of methods. The most readily available technique is X-ray diffraction (XRD). However, the amount of x-ray scattering from thin films can be very small and difficult to measure. In contrast, electron scattering can be more amenable to diffraction studies from small volumes. However, the strong interaction between electrons and the film results in multiple scattering events making S determinations more complex. When determining the order parameter by electron diffraction, a low intensity of the reflections may not be indicative of a low order parameter. To quantify S , electron scattering simulations are needed to predict the electron diffraction intensities for the superlattice and fundamental reflections for various film thicknesses [6,19].

1.2 Chemically partitioned soft magnetic ribbons

In efforts to improve the soft magnetic performance of nanocrystalline materials alloying element combinations [1] have been adjusted to control the microstructure. It has been shown that the morphology of the material, whether it is rods, particles, thin films, or bulk polycrystalline alloys, can influence the magnetic properties [20-21]. Soft magnetic materials are used in a wide range of application and can be classified by the operation frequency. For sub-MHz applications crystalline, nanocrystalline, and amorphous alloys are permissible. However,

for applications above 1 MHz highly resistive spinel ferrites are used to reduce eddy current losses [1]. Recent demand to miniaturize active components in power electronic devices has been the motivation for the development of advanced soft magnetic materials with high magnetization and low losses at frequencies above 1 kHz. The use of Finemet-type alloys for this application demonstrates the need for characterization of nanocrystalline materials for power-conditioning applications [22]. The alloy is an example of a nanocomposite which consists of nanocrystalline grains surrounded by an intergranular amorphous matrix [2]. The material exhibits combinations of high saturation induction and low core losses unobtainable in conventional amorphous or large-grained crystalline alloys [2]. Compositional quantification of the two phases is necessary to understand the influence of chemical partitioning on magnetic properties. Analysis of compositional gradients and intermixing of phases can be performed using the APT technique. The influence of voxel size on data analysis is considered in composition quantification of chemically partitioned nanostructures.

1.3 The A1 to L1₀ polymorphic phase transformation

Intermetallics have a wide range of applications which are strongly dependent upon the atomistic ordering in the crystal lattice. One specific application is thin film magnetic storage media [23-25]. The demand to continuously increase storage capacity requires the development of a new high density storage medium. The energy needed to maintain the direction of magnetization in a magnetic grain is proportional to the volume of the grain, i.e. $K_u V / k_B T$ where V is the volume of the grain, k_B is Boltzmann's constant and T is temperature. As the bit density increases, V becomes smaller therefore K_u must increase to maintain a thermally stable magnetization energy barrier [17, 23]. As the magnetic volume (bit size) continues to decrease to accommodate higher storage densities, the magnetization direction randomly fluctuates

because of thermal energy, $k_B T$, effects. This instability phenomenon is known as superparamagnetism [18]. The thermal stability of very small magnetic volumes can be improved if the material has a large uniaxial magnetocrystalline anisotropy, K_u . Intermetallic systems such as FePt, CoPt, AlMn, and FePd have been identified as candidate materials because of their high K_u ($\sim 10^7$ - 10^8 ergs/cc) [16-18]. However, the high K_u is only obtained when the material is chemically ordered. These alloys need the $L1_0$ phase of the previously mentioned intermetallic systems.

When FePt is sputter-deposited as a thin film, it nominally adopts the high temperature, soft-magnetic A1 phase. Subsequent annealing is required to phase transform FePt into the desired, hard magnetic $L1_0$ phase. The A1 phase is a random solid solution face-centered-cubic (fcc) structure and $L1_0$ is an ordered body centered tetragonal (bct) structure with alternating Fe and Pt atomic planes along the [001] c-axis [26-27]. Though A1 to $L1_0$ is a simple polymorphic phase transformation (a change in crystal symmetry and not composition), recent modeling predictions have suggested preferential segregation events at the nanometer length scale [28-30]. Moreover, the mechanism for A1 to $L1_0$ ordering can be complex.

A majority of the reports suggest that ordering is a first order phase transformation [31] with Fe-rich films being easier to phase transform at lower temperatures [3]. The nucleation and growth of the $L1_0$ phase proceeds by discontinuous precipitation [32-33]. In general, the $L1_0$ phase transformation in the FePt alloy begins behind an existing grain boundary and ordering occurs at the advancing grain boundary. Hence, precipitation does not occur continuously within a region, rather it occurs discontinuously as the grain boundary pass through the region. Farrow *et al.* [34] have suggested, given sufficient undercooling, the nucleation may even be of a continuous type rather than a first order phase transformation. Li *et al.* [4] recently reported dark

field transmission electron microscopy images for FePt thin films annealed in time scales of seconds that indicated that the ordering initiated at the grain boundaries. Grain boundaries are sources and sinks for vacancy migration [35] which would assist in the diffusion processes necessary for atomistic rearrangement. Since long range diffusion would not be required for this phase transformation, quantifying the subtle compositional fluctuations at or near grain boundaries is critical in understanding how the phase transformation initiates and evolves. APT analysis is used to quantify these subtle deviations in composition. Furthermore, it is essential to quantify the degree of chemical order in the nanoscale material to understand the structure-property relationship. In this work, electron diffraction techniques for order parameter determination are examined.

1.4 Dissertation Organization

The remainder of this work describes key findings of quantitative microanalysis techniques for magnetic nanostructures. Chapter 2 is a discussion on the influence of voxel size on atom probe tomography data using a chemically partitioned nanostructure as the model material system. A methodology for determining the appropriate voxel size for phase thresholding is described. Chapter 3 describes the role of Pt enrichment at grain boundaries in the $A1$ to $L1_0$ phase transformation in FePt thin films using TEM and APT microanalysis techniques. Chapter 4 provides insight into the field evaporation behavior in of FePt [001] thin films. Simulations are compared to experimental results to understand the aberrations observed in the 3D reconstruction. Finally, chapters 5 and 6 discuss the viability of electron diffraction for quantifying long-range order parameter in small volumes of ordered intermetallics.

CHAPTER 2

THE INFLUENCE OF VOXEL SIZE ON ATOM PROBE TOMOGRAPHY DATA¹

Abstract

A methodology for determining the optimal voxel size for phase thresholding in nanostructured materials was developed using an atom simulator and a model system of a fixed two-phase composition and volume fraction. The voxel size range was banded by the atom count within each voxel. Some voxel edge lengths were found to be too large, resulting in an averaging of compositional fluctuations. Others were too small with concomitant decreases in the signal-to-noise ratio for phase identification. The simulated methodology was then applied to the more complex experimentally determined data set collected from a $(\text{Co}_{0.95}\text{Fe}_{0.05})_{88}\text{Zr}_6\text{Hf}_1\text{B}_4\text{Cu}_1$ two-phase nanocomposite alloy to validate the approach. The Zr and Hf segregated to an intergranular amorphous phase while Fe preferentially segregated to a crystalline phase during the isothermal annealing step that promoted primary crystallization. The atom probe data analysis of the volume fraction was compared to transmission electron microscopy (TEM) dark field imaging analysis and a lever rule analysis of the volume fraction within the amorphous and crystalline phases of the ribbon.

¹ A manuscript has been prepared for the work in this chapter for publication in Ultramicroscopy as: K.L. Torres, M. Daniil, M.A. Willard, and G.B. Thompson, “The influence of voxel size on atom probe tomography data.”

2.1. Introduction

Subtle changes in local chemistry can significantly alter the properties of many materials. Atom probe tomography (APT) has the spatial resolution to detect these slight variations experimentally and provide a quantitative assessment for nanoscale features [1]. An atom probe experiment generates both spatial coordinates and the mass-to-charge-state ratio for chemical identification and a reconstructed rendering of the analyzed volume can be produced from the raw data using a 3D visualization software package. Features such as interfaces and precipitates can be easily observed. With recent advances in larger area detectors [1], APT can be used to quantify cluster size, composition, and volume fraction because of the larger number of atoms collected.

Previous works have shown how fluctuation in composition measurements are dependent on the number of atoms in the voxel [2,3], which is the three-dimensional banded volume metric for reconstruction. The error in measuring solute concentration in the voxel is inversely proportional to the square root of the number of atoms sampled [2]. As a result, the selection of voxel size can have a considerable impact on the results of the analysis. For example, a large voxel size can maximize the signal-to-noise ratio but can also average out compositional fluctuations. Conversely, too small of a voxel can lead to inadequate statistics in identifying a compositional microstructure feature. In this study, the influence of voxel dimension on the volume fraction and composition of chemically partitioned phases was examined.

A nanocomposite comprised of a crystallites, about 8 nm in diameter, embedded in an intergranular amorphous matrix, approximately 2 nm in thickness, was selected. This system was ideal for quantifying volume fraction using atom probe tomography and transmission electron microscopy (TEM) techniques, due to the size scale of the microstructural features and the

compositional differences between the two phases. The use of cross-correlative techniques provided a means of validating the atom probe determined volume fraction. Although composition and volume fraction have been studied in similar systems using APT [4-5], the aim of this study was to provide a method for evaluating the optimal voxel size for atom probe data analysis.

2.2. Experimental procedure

Amorphous alloy ribbons with composition $(\text{Co}_{0.95}\text{Fe}_{0.05})_{88}\text{Zr}_6\text{Hf}_1\text{B}_4\text{Cu}_1$ were produced using the single roller melt-spinning technique. The ribbons were subsequently annealed at 475°C for 1 hour to promote partial primary crystallization. X-ray diffraction (XRD) was performed using a Philips APD 3520 diffractometer with $\text{Cu K}\alpha$ radiation to identify phases and determine crystallite size. Details of the processing and correlation between structure and magnetic properties are discussed in references [6-7]. TEM foils were prepared by ultrasonically cutting 3 mm discs using a SiC abrasive. The discs were then mechanically ground and subsequently dimple polished using 3 μm diamond paste to a final thickness of 10 μm . The foil was ion milled in a Gatan PIPS at 3.5 keV until perforation and/or electron transparency. TEM microstructural characterization was performed in a FEI Tecnai F20 (S)TEM operated at 200kV. Atom probe tomography (APT) specimens were prepared from the annealed ribbons in a FEI Quanta 3D dual electron beam - focus ion beam (FIB) microscope using the *in-situ* technique described in reference [8]. APT analysis was performed in an Imago Scientific Instruments LEAP-3000XSiTM [9]. The experiments were performed at 60 K in ultrahigh vacuum conditions ($< 1 \times 10^{-9}$ Pa) using a pulse fraction of 0.15 and a pulse repetition rate of 200 kHz.

Analysis of the APT data was performed with Imago's Visualization and Analysis Software (IVAS) 3.4.1. Obtaining an optimal voxel size using experimental data can be difficult because many factors influence this selection. The concentration of a selected element in an analyzed volume was given in atomic percent by $C_i = N_i/N_t$, where N_i is the number of atoms of the element i and N_t is the total number of atoms in the volume. The standard error of the concentration because of counting statistics is $\sigma_c = \sqrt{C_i(1 - C_i)/N_t}$. In both the simulated and experimental data analysis, the error associated with the number of ions within a voxel is $\sigma_e = 1/\sqrt{N_t}$. To mitigate the experimental factors, the atom simulator included in IVAS was used to generate a data set with crystallites similar in dimension to those experimentally collected. Subsequently, a methodology for obtaining an optimal voxel size for the experimental data was developed.

2.3. Methodology

Initially, a simulated data set was generated to model the experimentally collected data. Spherical Fe enriched crystallites with a radius of 4 nm were embedded in a $\text{Co}_{95}\text{Fe}_5$ matrix. The body-centered cubic crystallites were randomly distributed within the matrix. An isoconcentration surface was used to identify the precipitates. In this type of analysis, the data was divided into voxels and the composition of each voxel was determined by counting the atoms of each type within the voxel. By selecting a concentration intermediate of the two phases, a surface was constructed to outline regions of constant concentration [2]. The proximity histogram [10] shown in Figure 2.1 was used to evaluate the phase composition. In this example, the isoconcentration surface of 7 atomic percent Fe defines the interface between the two phases.

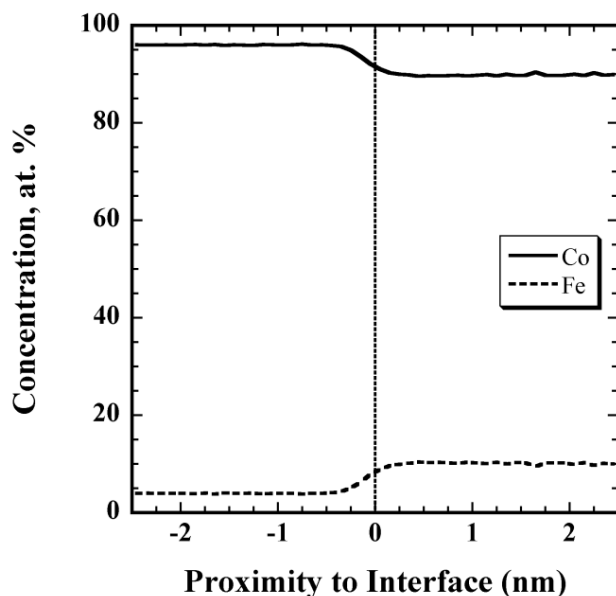


Figure 2.1. A proximity histogram of Co and Fe in the sample with respect to the Fe 7 atomic percent isoconcentration surface. The bin size was 0.1 nm. The calculation was made over a volume 30 nm x 30 nm x 60 nm and includes 54 crystallites.

In this simulated study, cubic voxels with edge lengths between 0.4 nm and 2.0 nm were analyzed in increments of 0.2 nm. For each reconstruction, the parameters of voxel edge length and delocalization were maintained at a constant ratio of 1:2. The phase compositions were determined for each voxel size by isolating the phase with an isoconcentration surface of 7 atomic percent Fe and generating a new mass spectrum. Next, a bounded volume was used to determine the volume fraction of each phase. Finally, a sampling of voxels was taken to determine the atom count distribution for each edge length. A summary of these results is tabulated in Table 2.1.

By varying the voxel edge length in the analysis of the model system, parameters such as phase composition, ion count, and volume fraction were identified as being most influenced by voxel size selection. Results in Table 2.1 identify a range of voxel edge lengths between 0.6 nm and 2.0 nm where the composition of the crystallite was within 5 percent error of the nominal

crystallite composition of 10 atomic percent Fe. The nominal volume fraction for the generated data set was 0.23. In Table 2.1, edge lengths between 0.6 nm and 1.2 nm yielded a volume fraction of 0.21.

Table 2. 1. Results of composition and volume fraction for the analysis of the Co-Fe model system. The error given was associated with the number of ions within a given voxel.

Voxel Edge Length (nm)	Composition (atomic %)						Ions per voxel	Error, σ_e (%)
	Matrix			Crystallite				
	Co	Fe	Volume Fraction	Co	Fe	Volume Fraction		
0.4	96.21	3.79	0.80	88.63	11.37	0.20	11	30.2
0.6	95.96	4.04	0.79	89.83	10.17	0.21	32	17.7
0.8	95.89	4.11	0.79	89.91	10.09	0.21	76	11.5
1.0	95.86	4.14	0.79	89.95	10.05	0.21	144	8.3
1.2	95.75	4.25	0.79	89.98	10.02	0.21	256	6.3
1.4	95.66	4.34	0.80	90.02	9.98	0.20	415	4.9
1.6	95.80	4.2	0.80	89.98	10.02	0.20	614	4.0
1.8	95.48	4.52	0.82	90.08	9.92	0.18	875	3.4
2.0	95.48	4.52	0.83	90.12	9.88	0.17	1205	2.9

Miller and Hetherington introduced a useful parameter for the selection of block size defined by the length of the composition profile [2]. This length is written as,

$$\Delta C_f = \langle |c(i, N_b) - c(i + 1, N_b)| \rangle, \quad (2.1)$$

where the angle brackets indicates the mean value, N_b is the number of ions per voxel, and i is a parameter that represents the voxel index. This length was not the distance over which the composition profile was taken rather it was an average of compositional differences between neighboring voxels. Figure 2.2 illustrates this length as a function of ion count. Miller and Hetherington observed three regions of scaling in the ΔC_f curves with ion count [2]. As observed in Figure 2.2, the initial decrease in ΔC_f was because the noise within the phase decreased with an increase in sample size. Next, in the flat regime, the voxel size sampled the number of ions on the order of the fluctuations in the two phases. Finally, the ΔC_f value decreases which was

contributed to the averaging of the compositional fluctuations in the two phases as the voxel size was increased. The flat regime in Figure 2.2 provided a voxel range where the sampling size was on the order of the compositional fluctuations. The voxel edge lengths in the model system were limited between 0.8 nm and 1.8 nm with sampling sizes between 77 and 875 ions per voxel, respectively. The edge length was selected from the overlapped bandwidth in Figure 2.3. In the model system, a voxel edge length between 0.8 nm and 1.2 nm was identified as being optimal for this simulated analysis.

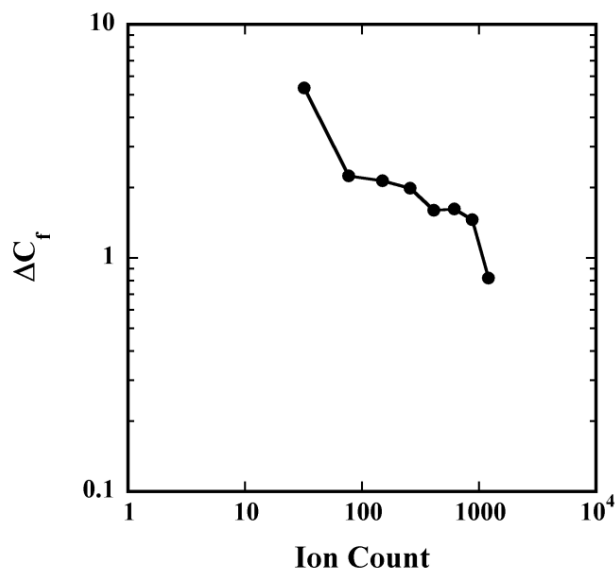


Figure 2.2. The length of the composition profile, ΔC_f , plotted as a function of ion count.

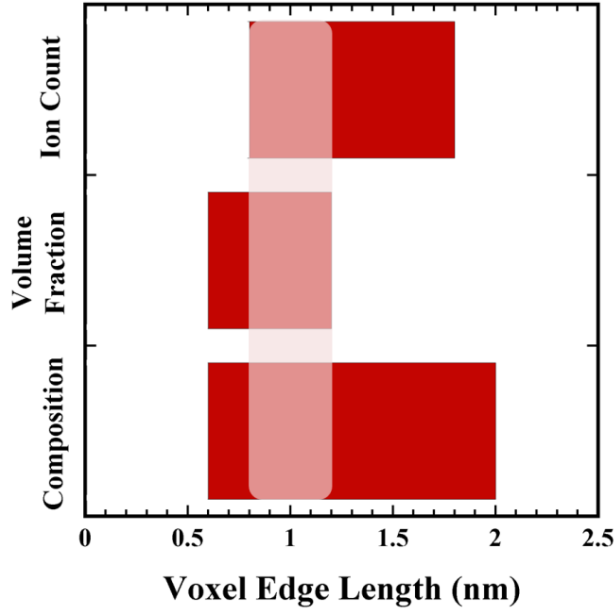


Figure 2.3. Results of composition, volume fraction, and ion count for the Co-Fe model system. The highlighted band is the optimal range for voxel edge length in the system consisting of 8 nm diameter crystals.

2.4. Results and Discussion

The experimental data sets were taken from melt spun ribbons which were amorphous in the as-spun condition. An isothermal annealing step was used to promote primary crystallization, Zr and Hf segregate to the remaining, intergranular amorphous phase while Fe segregates to the forming crystalline phase [4] as shown in Figure 2.4. The compositional segregation provided an experimental system for identifying the two phases easily using isoconcentration surfaces and proximity histograms. To quantify volume fraction crystallized, a cylinder with a diameter of 27 nm and a length of 65.5 nm was extracted from the center of the APT reconstruction providing a known volume for analysis. This truncated data set used for analysis contained 6.5 million atoms. An isoconcentration surface of 6 atomic percent Fe was used to create an interface to separate the two phases as seen in the proximity histogram in Figure 2.5(a). The isolated Fe crystallites are shown in Figure 2.5(b). The differences between

the simulated data and the experimental Fe isoconcentration surface can be attributed to multi-component nature of the experimental data.

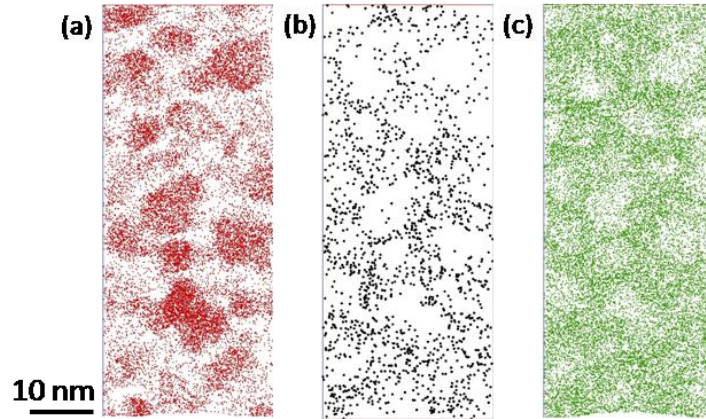


Figure 2.4. (a) Fe atom map. (b) Hf atom map. (c) Zr atom map.

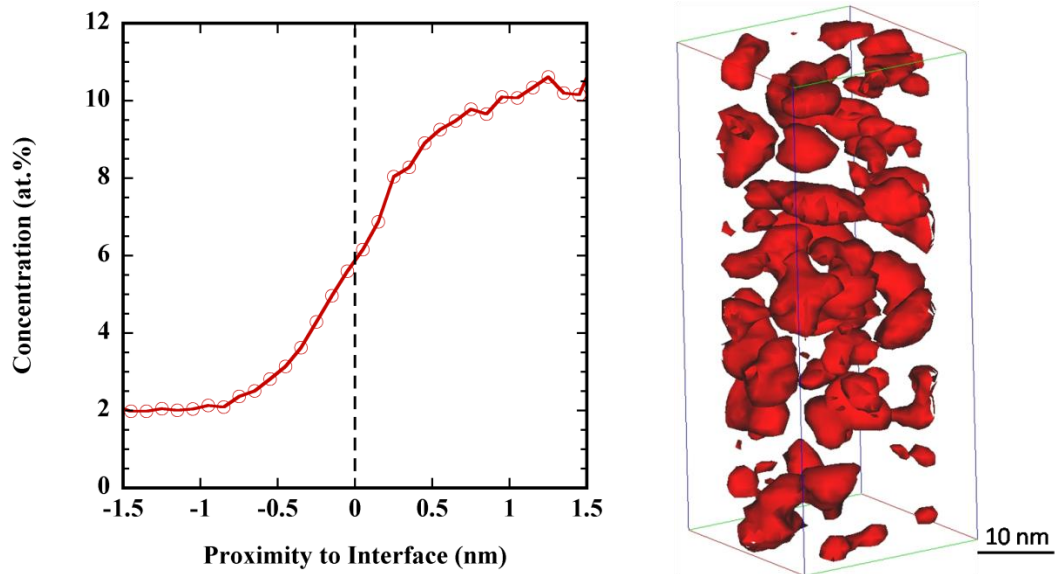


Figure 2.5. (a) Proximity histogram of Fe with respect to the 6 atomic percent Fe isoconcentration surface. The bin size was 0.1 nm. (b) Isoconcentration surfaces of 6 atomic percent Fe isolating the crystallite phase.

The voxel edge length was varied between 0.4 nm and 2.2 nm in increments of 0.2 nm to determine its effect on phase composition, volume fraction, and ion count per voxel for this experimental data set. The composition of the two phases was calculated after isolating the crystallites from the amorphous matrix. From this information, a bounded volume was used to determine the volume fraction of each phase. Table 2.2 is a summary of compositional results and Table 2.3 is a summary of results for volume fraction and atom count per voxel. Note the compositional analysis breaks down at edge lengths 0.4 nm, 0.6 nm, and 2.2 nm. The composition of the phases varies drastically for these three voxel edge lengths. For small voxel edge lengths (0.4 and 0.6 nm), the deviation can be attributed to the error associated with composition determination within the voxel (e.g. not enough ion counts per voxel). The error, σ_e , within the voxel was inversely proportional to the square root of the number of atoms in the voxel. As shown in Table 2.3, the error increases with a decrease in voxel dimension. For the large voxel edge length (2.2 nm), the error due to counting statistics was greatly diminished. However, the compositional variance in this case was attributed to a loss in fidelity in identifying the interface between the two phases. For voxel lengths greater than 0.6 nm and less than 2.2 nm, the composition difference between edge lengths varied less than 2 atomic percent. This suggests robustness in the compositional analysis for adequate voxel lengths.

Table 2. 2. Compositional results from the APT experimental analysis.

	Voxel	Composition (atomic %)					
	Edge Length (nm)	Co	Fe	Zr	B	Cu	Hf
Amorphous Phase	0.4	84.13	0.84	7.03	5.28	1.36	1.36
	0.6	83.09	1.60	7.15	5.38	1.38	1.40
	0.8	82.38	2.11	7.21	5.47	1.41	1.43
	1.0	82.23	2.19	7.20	5.45	1.40	1.43
	1.2	82.24	2.38	7.13	5.44	1.40	1.41
	1.4	82.25	2.48	7.08	5.41	1.40	1.40
	1.6	82.29	2.49	7.05	5.39	1.39	1.39
	1.8	82.41	2.66	6.91	5.31	1.37	1.35
	2.0	82.44	2.67	6.90	5.28	1.36	1.35
	2.2	82.63	2.85	6.72	5.17	1.33	1.29
Crystalline Phase	0.4	83.59	10.09	3.32	2.37	0.28	0.36
	0.6	85.16	8.68	3.25	2.31	0.27	0.32
	0.8	86.14	7.77	3.25	2.26	0.27	0.31
	1.0	86.23	7.69	3.25	2.27	0.26	0.30
	1.2	86.35	7.39	3.36	2.29	0.27	0.34
	1.4	86.35	7.27	3.42	2.33	0.27	0.35
	1.6	86.35	7.31	3.41	2.31	0.27	0.35
	1.8	86.18	7.07	3.61	2.42	0.30	0.41
	2.0	86.21	7.15	3.56	2.40	0.29	0.39
	2.2	85.94	6.90	3.81	2.56	0.33	0.46

Table 2. 3. Volume fraction, ions per voxel, and error results from the experimental analysis of APT. The error given is associated with the number of ions within a given voxel.

Voxel Edge Length (nm)	Volume Fraction				Ions per voxel	Error, σ_e (%)
	APT Analysis		Lever Rule			
	Amorphous	Crystalline	Amorphous	Crystalline		
0.4	0.67	0.33	0.02	0.98	5	44.7
0.6	0.67	0.33	0.75	0.25	18	23.6
0.8	0.66	0.34	0.68	0.32	48	14.4
1.0	0.66	0.34	0.67	0.33	73	11.7
1.2	0.65	0.35	0.67	0.33	119	9.2
1.4	0.65	0.35	0.67	0.33	189	7.3
1.6	0.66	0.34	0.68	0.32	288	5.9
1.8	0.66	0.34	0.68	0.32	419	4.9
2.0	0.66	0.34	0.69	0.31	578	4.2
2.2	0.66	0.34	0.71	0.29	765	3.6

TEM imaging was used to evaluate volume fraction and crystallite size in this sample. A series of dark field images were taken completely around the $\{110\}$ body-centered cubic Fe ring in Figure 2.6(a) using the technique described in reference [11]. These images were then compiled into a single image, seen in Figure 2.6(b), using the Image J software. To simplify the analysis, the foil thickness in the region of interest was assumed to be constant. The average crystallite size was ~ 8 nm in diameter and was consistent with the crystallite size determined by the x-ray diffraction Scherrer analysis [12]. A volume fraction analysis was performed on the compiled image by determining the area occupied by the crystallites compared to the total area of the micrograph. The volume fraction of the crystalline phase was 0.39. These results are in agreement with APT results which reported 0.35 at the optimal voxel length. The discrepancy between the two techniques was attributed to assuming that the two phases span the entire thickness of the foil and the foil was of constant thickness. The agreement between the two techniques suggests that the bounded volume approach was robust and the volume fraction estimates using this method were not significantly altered by voxel size selection once optimized.

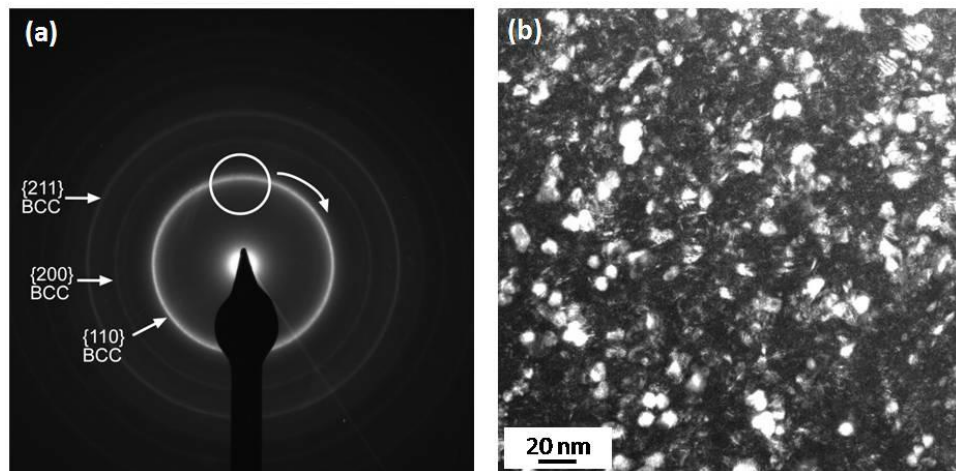


Figure 2.6. (a) Diffraction pattern used for dark field imaging. (b) Compiled micrograph using Image J software of all dark field images.

The average composition of the crystallite and amorphous regions determined by atom probe analysis provides another means for calculating the volume fraction of the nanocrystals according to the lever rule [5]. This was given as

$$f_v^X = \left(\frac{C_X^0 - C_X^m}{C_X^n - C_X^m} \right), \quad (2.2)$$

where C_X^0 is the global concentration in element X, C_X^m is the concentration of element X in the amorphous matrix and C_X^n is the concentration of element X in the nanocrystals [6]. This expression of the volume fraction assumes that the molar volumes are equal in the amorphous phase and in the nanocrystals. The major element Co was considered in this analysis. For edge lengths 0.4 nm and 0.6 nm, the lever rule would not apply because the dimension of the voxel was approaching atomic dimensions. The error associated with the phase composition is large thus the volume fraction calculated was inaccurate. The lever rule analysis was also inappropriate for edge lengths greater than 2.2 nm because of the loss of fidelity in identifying the interfaces between the phases; consequently, inaccurate composition measurements of the phases results. For edge lengths greater than 0.6 nm and less than 2.2 nm, the lever rule results tabulated in Table 3 are in good agreement with the bounded volume approach and TEM results. The limiting factor for applying the lever rule was the error associated with estimating the composition. This method assumed sharp interfaces between phases and could influence the composition of the phases and thus the volume fraction. However, the composition does not vary greatly with respect to changes in voxel edge length within the optimal range. This approach provided a secondary means for determining volume fraction.

2.5. Conclusions

In this study, the influence of voxel dimension on the volume fraction and composition of chemically partitioned phases was examined. A methodology for determining an optimal voxel dimension range was developed by using a model system for the experimental data set. For a spherical particle with an 8 nm diameter, a voxel edge length between 0.8 nm and 1.2 nm was determined to yield the most reliable composition and volume fraction results. The composition and volume fraction were determined from an experimental nanocrystallite in an amorphous ribbon using this method. A breakdown of the analysis was observed at edge lengths of 0.6 nm or smaller because the large error in composition determination within the voxel. At voxel edge lengths of 2.2 nm or greater, errors in composition are observed because of a loss in fidelity identification of the interface. These errors result in incorrect phase compositions and erroneous volume fractions as determined by the lever rule. The APT determined volume fraction was compared to a dark-field TEM analysis of the experimental crystallites and a compositional bases lever rule approach [5]. The optimized voxel length was in good agreement with the APT results.

2.6. References

- [1] T.F. Kelly and M.K. Miller, *Review of Scientific Instruments* 78 (2007) 031101.
- [2] M.K. Miller, A. Cerezo, M.G. Hetherington, and G.D.W. Smith, *Atom Probe Field Ion Microscopy*, Clarendon Press, Oxford, 1996.
- [3] M.P. Moody, L.T. Stephenson, P.V. Liddicoat, and S.P. Ringer, *Microscopy Research & Technique* 70 (2007) 258.
- [4] P.R. Ohodnicki, Y.L. Qin, D.E. Laughlin, M.E. McHanry, M. Kodzuka, T. Ohkubo, K. Hono, and M.A. Willard, *Acta Materialia* 57 (2009) 87.

- [5] W. Lefebvre, S. Morin-Grognet, and F. Danoix, *Journal of Magnetism and Magnetic Materials* 301 (2006) 343.
- [6] T.M. Heil, K.J. Wahl, A.C. Lewis, J.D. Mattison, and M.A. Willard, *Applied Physics Letters* 90 (2007) 212508.
- [7] M. Daniil and M. A. Willard, *Journal of Applied Physics* 103 (2008) 07E727.
- [8] K. Thompson, D. Lawrence, D.J. Larson, J.D. Olson, T.F. Kelly, and B. Gorman, *Ultramicroscopy* 107 (2007) 131.
- [9] T.F. Kelly, T.T. Gribb, J.D. Olson, R.L. Martens, J.D. Shepard, S.A. Wiener, T.C. Kunicki, R.M. Ulfig, D.R. Lenz, E.M. Strennen, E. Oltman, J.H. Bunton, and D.R. Strait, *Microscopy and Microanalysis* 10 (2004) 373.
- [10] O.C. Hellman, J.A. Vandenbroucke, J. Rusing, D. Isheim, and D.N. Seidman, *Microscopy and Microanalysis* 6 (2000) 437.
- [11] B. Yao and K.R. Coffey, *Journal of Applied Physics* 105 (2009) 033901.
- [12] A.L. Patterson, *Physical Review Letters* 56 (1939) 978-982.

CHAPTER 3

GRAIN BOUNDARY ENRICHMENT IN THE FEPT POLYMORPHIC A1 TO $L1_0$ PHASE TRANSFORMATION²

Abstract

A series of $\text{Fe}_{54\pm 1}\text{Pt}_{46\pm 1}$ thin films have been sputter-deposited and annealed at various times and temperatures to facilitate the A1 to $L1_0$ polymorphic phase transformation. The annealing times span one minute to tens of minutes over temperatures of 300°C to 800°C. The films were characterized by x-ray and electron diffraction and atom probe tomography. This time-temperature regime provides ‘snap-shots’ into the compositional segregation evolution at the grain boundaries during the polymorphic phase transformation. The as-deposited A1 phase showed a preferential segregation of Pt to the grain boundaries. The reduction of Pt enrichment at the boundaries was observed for all $L1_0$ ordered films.

² The work in this chapter has been reprinted from Ultramicroscopy, 109/5, K. L. Torres and G.B. Thompson, ‘Grain boundary enrichment in the FePt polymorphic A1 to $L1_0$ phase transformation,’ 606-611, (2009), with permission from Elsevier.

3.1 Introduction

A significant challenge for next-generation computer hard drive technology is developing the class of materials which can overcome the superparamagnetic limit for small bit-size media [1]. As the magnetic volume decreases, the magnetization can randomly fluctuate because of thermal energy, $k_B T$; a phenomenon referred to as superparamagnetism [2]. The energy needed to maintain the direction of magnetization in a magnetic grain is proportional to the volume of the grain, i.e. $K_u V / k_B T$ where K_u is the uniaxial magnetocrystalline anisotropy, V is the volume of the grain, k_B is Boltzmann's constant and T is temperature. As the bit density increases, V becomes smaller therefore K_u must increase to maintain a thermally stable magnetization energy barrier.

The high K_u of $L1_0$ FePt has made this material a leading candidate for thermally stable magnetic storage media [3]. When FePt is sputter-deposited as a thin film, it nominally adopts its high temperature, soft-magnetic A1 phase. A subsequent anneal is required to phase transform FePt into the desired, hard magnetic $L1_0$ phase. The A1 phase is a random solid solution face-centered-cubic structure and $L1_0$ is an ordered body centered tetragonal (bct) structure with alternating Fe and Pt atomic planes along the [001] c-axis [4-5]. Though A1 to $L1_0$ is a simple polymorphic phase transformation (a change in crystal symmetry and not composition), recent modeling predictions have suggested preferential segregation events at the nanometer length scale [6-8]. Moreover, the mechanism for A1 to $L1_0$ ordering can be complex. A majority of the reports suggest that the ordering is a first order phase transformation [9-10] with Fe-rich films being easier to phase transform at lower temperatures [11]. The nucleation and growth of the $L1_0$ phase proceeds by discontinuous precipitation [12]. Farrow *et al.* [13] has suggested, given sufficient undercooling, the nucleation may even be of a continuous type rather than a first order phase transformation. Li *et al.* [14] recently reported dark field transmission electron microscopy

images for FePt thin films annealed in time scales of seconds that indicated that the ordering initiated at the grain boundaries. Grain boundaries are sources and sinks for vacancy migration [15] which would assist in the diffusion processes necessary for atomistic rearrangement. Since long range diffusion would not be required for this phase transformation, quantifying the subtle compositional fluctuations at or near grain boundaries would be critical in order to understand how the phase transformation initiates and evolves.

The time scales for the A1 to $L1_0$ phase transformation has been modeled to be on the order of tens of milliseconds for temperatures ranging from $\sim 500^\circ\text{C}$ to $\sim 1100^\circ\text{C}$ [16,17]. To capture these initial stages of ordering, there are several experimental challenges to anneal in this time and temperature range. Recently Berry and Barmak [16] published time-temperature-transformation curves for this phase transformation. These curves serve as a guide to capture the early ordering behavior. The initial ordering could be facilitated by annealing the thin films at lower temperatures and longer times (tens of seconds to minutes). By quantifying the microstructure behavior in this time-temperature regime, the influence of potential compositional fluctuations in this phase transformation could be characterized.

There have been very limited experimental reports that quantify the minute *atomic-level* compositional segregation and its influence on the microstructural stability of the FePt thin film. Rather, most reports have addressed the phase transformation in terms of the grain size stability and growth [4,5; 18 -20]. The atom probe is an ideal instrument to quantify subtle compositional fluctuations that occur during this polymorphic phase transformation.

3.2 Experimental Details

A series of 30 nm $\text{Fe}_{54\pm 1}\text{Pt}_{46\pm 1}$ thin films were DC magnetron deposited onto an ambient temperature [001] Si substrate using elemental 99.5% Fe and 99.5% Pt targets in an AJA ATC 1500-F sputtering system. The 30 nm film was comprised of 66 bi-layers of Pt and Fe with 0.20 nm and 0.26 nm thicknesses, respectively. The sputtering rate for Fe was 0.052 nm/sec. and for Pt was 0.071 nm/sec and the substrate was rotated during deposition to ensure compositional and thickness uniformity over the substrate surface. The nominal composition and standard deviation in the composition for the thin film was verified by averaging seven atom probe data sets with each data set comprising a minimum of 1.0 million ions. All the annealing experiments and all of these data sets were taken from the same thin film deposited at the same time to ensure consistent compositional control. The atom probe verified composition of $\text{Fe}_{54\pm 1}\text{Pt}_{46\pm 1}$ matched very well with the intended $\text{Fe}_{55}\text{Pt}_{45}$ targeted composition.

To prevent potential silicide formation of the film with the substrate during the annealing studies, a 10 nm silicon nitride diffusion-barrier layer was RF sputter-deposited from a Si_3N_4 composite target. To eliminate the potential oxidation of the $\text{Fe}_{54\pm 1}\text{Pt}_{46\pm 1}$ film during furnace annealing, a 10 nm silicon nitride capping layer was also deposited onto the surface of the $\text{Fe}_{54\pm 1}\text{Pt}_{46\pm 1}$ thin film. Prior to deposition, the sputtering chamber was evacuated to a base pressure of $< 5 \times 10^{-8}$ Torr. Ultra-high purity Ar, which served as the working gas for sputtering, was flowed into the chamber at 10 sccm to a pressure of 2.0 mTorr during sputtering.

Post-deposition, the thin film/wafer was scribed into 8 mm x 10 mm samples for annealing. Again, this assured that all microstructure comparisons were performed on the same thin film deposited at the same time. These smaller samples were encapsulated in a quartz tube with a Ti foil (used as a getter for residual oxygen) and evacuated to $< 1 \times 10^{-4}$ Torr then back-

filled with Ar/4% H_2 gas mixture to 30 Torr. The evacuation and gas purging was done for five-cycles. The annealing was conducted in a standard laboratory tube furnace. The time for annealing was taken to start when the specimen reached the set-point temperature as measured by an *in-situ* type K thermal couple that was attached to a wafer which was placed alongside the sample of interest. The heating and cooling rates of the samples were determined prior to annealing and were on the order of 110°C/min. for heating up and 180°C/min. for cooling. Table 3.1 is a tabulation of the various time and temperatures that have been investigated.

Table 3. 1. Summary of the times, temperatures, c/a ratios, and order parameters for the samples presented.

Treatment	c/a ratio	Order Parameter, S
400°C/1 min.	1.000	--
600°C/1 min.	0.964	0.38
800°C/1 min.	0.960	0.59
400°C/30 min.	0.966	0.42
600°C/30 min.	0.960	0.51
800°C/30 min.	0.957	0.66
300°C/100 min.	1.000	--
350°C/100 min.	0.967	0.39
400°C/100 min.	0.961	0.43
600°C/100 min.	0.957	0.51

The phase identification of the films was determined by electron diffraction in the TEM and X-ray Diffraction (XRD) using a Phillips APD 3830 X-ray diffractometer operating at 40kV and 35 mA with Cu K_{α} radiation as the source. The order parameter, S , of the thin films was determined by measuring the peak intensities of the (001) and (002) reflections given below [21]

$$S^2 = \frac{\left[\frac{(001)}{(002)} \right]_{\text{exp}}}{\left[\frac{(001)}{(002)} \right]_{\text{theory}}} \quad (3.1)$$

The theoretical peak intensities of (001)/(002) are based upon the JCPDS intensities for random orientation [22]. In order to accommodate possible texture influence, the peak intensity ratio is based on reflections in the same crystallographic direction. Table 3.1 is a summary of the order parameters determined with their corresponding heat treatments.

Atom probe samples were prepared by annular Focus Ion Beam (FIB) milling based on the *in-situ* lift-out technique described by Thompson *et al.* [23]. The FIB milling was performed using a FEI Quanta 3D dual beam FIB with initial milling at 30keV and final milling at 5keV. The ‘low keV clean up’ of the surface resulted in < 0.7 at.% Ga damage on the outer surface of the sample. Initially, the thin film with substrate was extracted by FIB milling from the wafer and mounted in an orientation that required the field evaporation of the silicon nitride layer then the Fe_{54+/-1}Pt_{46+/-1} layer. This resulted in a propensity of fracture failures because of the different evaporation fields of these materials. In a modified geometry, the sample was mounted orthogonal to this original direction allowing both the silicon nitride and Fe_{54+/-1}Pt_{46+/-1} layers to evaporate simultaneously. This resulted in a significant increase in successful evaporations of the sample and data collection. Moreover, the orthogonal mount allows FIB milling from the back side of the Si wafer which increased the probability of capturing the thin film region of interest during the preparatory milling sequences. In this orientation, particular care in the atom probe reconstruction was performed by selecting the Fe_{54+/-1}Pt_{46+/-1} film region that was sandwiched between the silicon nitride layers and comparing the curvature data from TEM imaging of an atom probe tip extracted post field evaporating using the FIB lift out procedure, as seen in Figure 3.1. The TEM was performed using a 200keV FEI Tecnai F20.

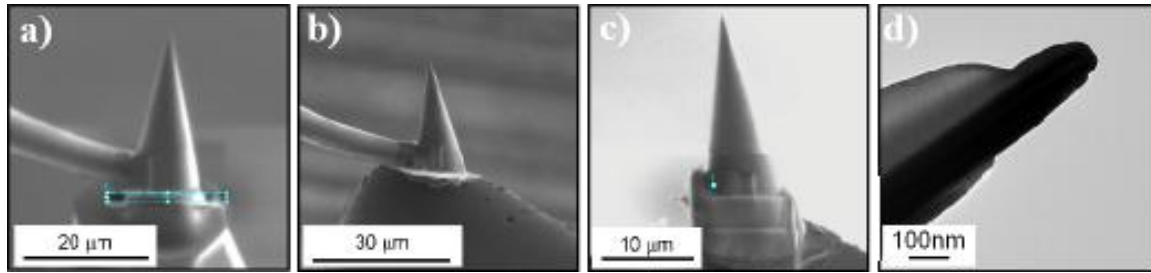


Figure 3. 1. (a) *In-situ* micromanipulator tungsten-needle attached to an atom probe micro-tip. The base of the tip is subsequently FIB milled to liberate the tip from the base. (b) Attachment of the FIB cut-out/lift-out tip to a TEM grid. *In-situ* Pt-deposition from the FIB provided the adhesion material between the tip and grid. (c) FIB removal of the micro-tip from tungsten-needle (d) TEM image of an as-deposited tip.

The atom probe tips were analyzed in an Imago Scientific Instruments Local Electrode Atom Probe (LEAP®) 3000XSi in a laser pulsing mode. The pulse energy ranged from 0.4 to 0.6 nJ with a pulse rate of 250 kHz, target evaporation of 1.0% and a specimen temperature of 80K. One-dimensional compositional profiles were taken from the data sets with the standard error values based upon $\sigma = \sqrt{n_i}/n_t$, where n_i is the number of i atoms and n_t is the total number of atoms [24]. Ten to twenty-five different grain boundaries were analyzed for each sample. Table 3.2 provides the average Pt concentration observed in the grain boundaries for all analyzed atom probe samples.

Table 3. 2. Summary of the average grain boundary Pt concentration for $\text{Fe}_{54\pm 1}\text{Pt}_{46\pm 1}$ thin films analyzed in the atom probe.

Treatment	No. of Grain Boundaries	Pt at%	σ , (+/-)
As deposited	25	53.0	2.5
400°C/1min.	10	51.7	2.1
400°C/30min.	10	49.7	2.3
600°C/30min	13	48.5	1.9
350°C/100min.	13	49.2	1.9
400°C/100min.	20	49.9	2.3

3.3 Results and Discussion

The XRD scans for the as-deposited and 400°C/1 min. annealed thin films are shown in Figure 3.2 (a) and indicate only the A1 phase with a strong {111} fiber texture. No silicon nitride peaks were observed. This is likely a result of the low volume fraction and sputter-deposited induced amorphous structure. The as-deposited thin film and the 400°C/1 min. annealed film had similar A1 lattice parameters, 0.383 nm and 0.381 nm respectively. In agreement with the XRD results, the electron diffraction pattern of the 400°C/1 min. annealed film indicated no $L1_0$ superlattice reflections, as seen in Figure 3.2(b). Atom probe samples were made from these two films as described above. The one-dimensional compositional profiles through the reconstructed grain boundaries of each film are shown in Figures 3.3(a) and 3(b). The films showed a 2σ increase in Pt enrichment at the grain boundary as compared to the nominal 46 at.% Pt of the film. The Pt atom maps of the reconstructed data are shown in Figures 3.3(c) and 3.3(d). Grain boundaries, observed as high density regions of Pt, are observed in both figures. The stripes observed in the cross-sectional view of the atom map of Figure 3.3(d) are the density variations along the columnar grain boundary. These grain boundaries are somewhat parallel in the cross-sectional view because this is the growth direction of the film. The variation of the spacing of the stripes in the cross-section is an artifact of viewing a 2D serial section of a 3D microstructural feature. TEM Frensel contrast imaging of the FePt in-plane grain boundaries was performed, as seen in Figure 3.3(e). This technique, described in reference [25], provided confirmation that density variations do exist along the grain boundaries [26-28]. The size and shape of the grains in the TEM micrographs matched the size and shapes enclosed by the density variations in the atom maps.

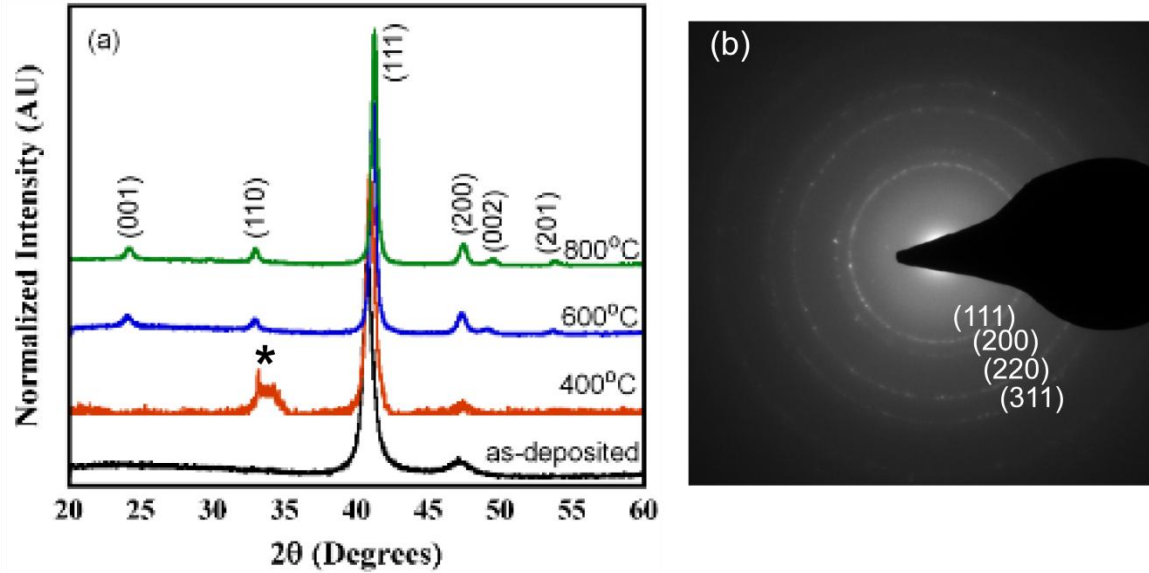


Figure 3. 2. (a) XRD scans of the as-deposited $\text{Fe}_{54\pm 1}\text{Pt}_{46\pm 1}$ thin film and $\text{Fe}_{54\pm 1}\text{Pt}_{46\pm 1}$ thin films annealed for 1 minute. The asterisk indicates a peak associated with the glass slide used to hold the sample for XRD (b) Electron diffraction pattern of the $\text{Fe}_{54\pm 1}\text{Pt}_{46\pm 1}$ thin film annealed at 400°C for 1 minute.

Though the as-deposited film was Fe-rich, the atom probe compositional profiles clearly indicated a preference of Pt to the grain boundaries. There have been a few modeling simulations that have suggested that Pt tends to migrate to the free surface in Al nanostructures in order to reduce the surface energy [6-8]. Though these studies were for either nanoparticles or limited volumes, and not explicitly thin films, they do demonstrate a tendency for the free surface to have a thermodynamic preference for Pt. The segregation of Pt, even for this as-deposited Fe-rich film, demonstrates that the driving force for surface migration to the boundaries is significant.

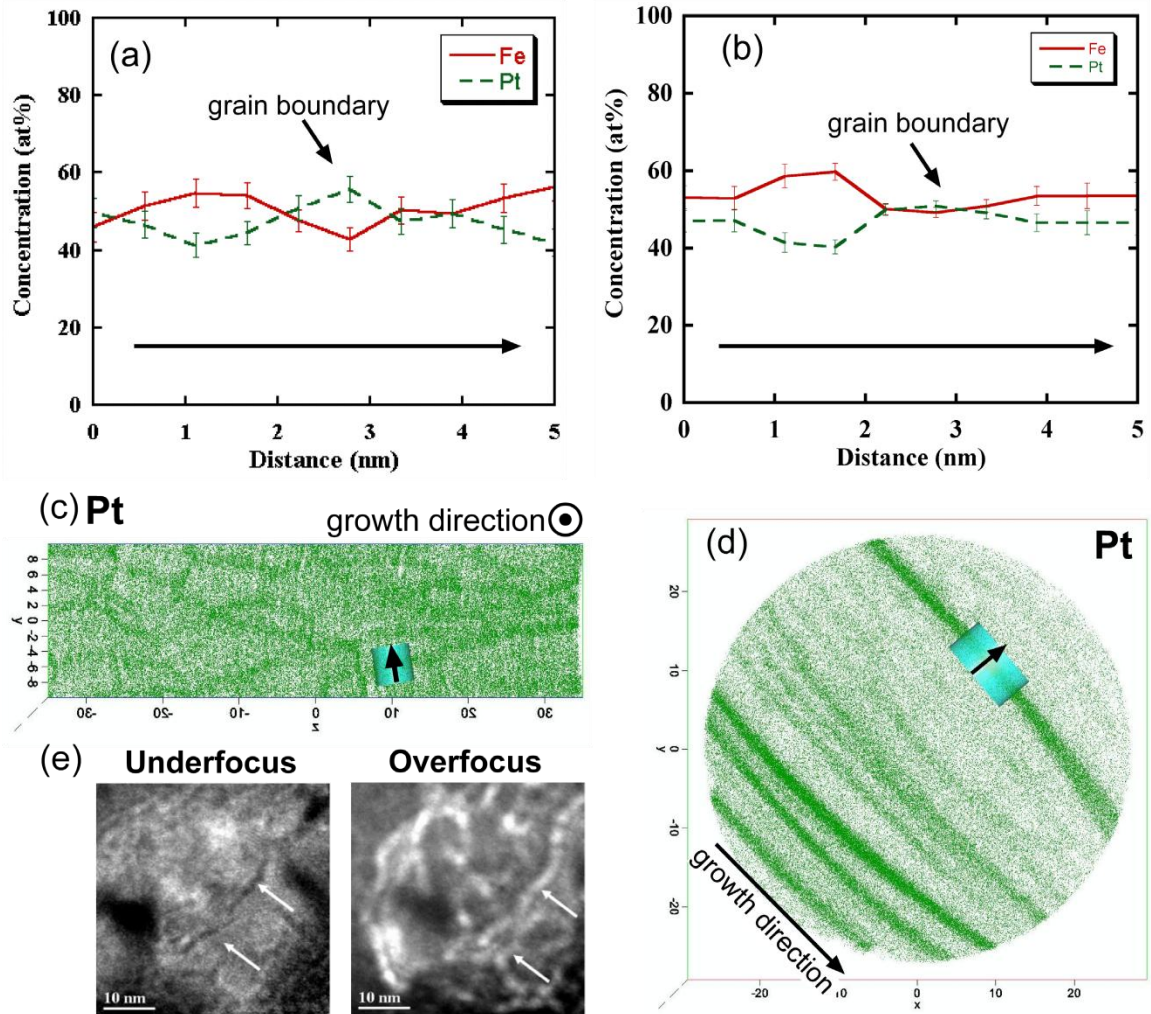


Figure 3. 3. A one-dimensional concentration profile through a grain boundary in (a) the as-deposited $\text{Fe}_{54\pm 1}\text{Pt}_{46\pm 1}$ thin film and (b) the $\text{Fe}_{54\pm 1}\text{Pt}_{46\pm 1}$ thin film annealed at 400°C for 1 minute. The solid red line is Fe and the dotted green line is Pt. A Pt atom map indicating the analysis direction and grain boundary used for (c) the as-deposited $\text{Fe}_{54\pm 1}\text{Pt}_{46\pm 1}$ thin film viewed in-plane and (d) the $\text{Fe}_{54\pm 1}\text{Pt}_{46\pm 1}$ thin film annealed at 400°C for 1 minute viewed in cross-section. The strips are the high density variations along the columnar grain boundaries. (e) Under- and over- focused in-plane TEM images of the as-deposited thin film. The white arrows indicate the grain boundary. The defocus length was $\pm 1.11 \mu\text{m}$.

The XRD scans for the thin films annealed at 400°C , 600°C and 800°C for 30 minutes all indicated the presence of the $L1_0$ phase as seen in Figure 3.4(a). This is shown by the onset of the superlattice (001) and (110) reflections and the split in the (200) and (002) reflection. The XRD

scans for 300°C, 350°C, 400°C and 600°C temperatures annealed for 100 minutes are plotted in Figure 3.4(b). Superlattice reflections were evident for films annealed at 350°C or higher. This suggests that the 300°C film/100 min. may be a lower bound in temperature for initiating ordering for these annealing times. The thin films annealed at 400°C /30 min. and 350°C/100 min. have a similar c/a ratio, 0.966 and 0.967, respectively. The c/a ratio for each film was calculated from the (001) and (200) reflections. The films annealed at 600°C/30 min. and 400°C/100 min. have a similar c/a ratio, 0.960 and 0.961 respectively. The increase in tetragonality was in agreement with the increase in the order parameter tabulated in Table 3.1.

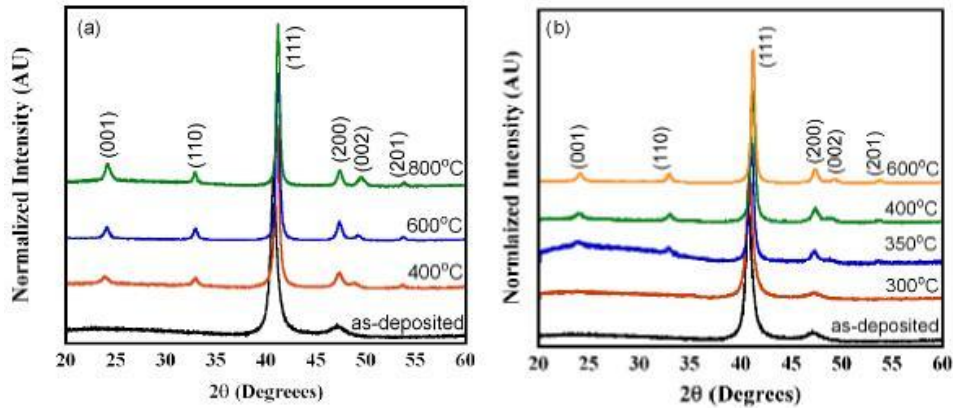


Figure 3. 4. (a) XRD scans of the as-deposited $\text{Fe}_{54\pm 1}\text{Pt}_{46\pm 1}$ thin film and $\text{Fe}_{54\pm 1}\text{Pt}_{46\pm 1}$ thin films annealed for 30 minutes. (b) XRD scans of the as-deposited $\text{Fe}_{54\pm 1}\text{Pt}_{46\pm 1}$ thin film and $\text{Fe}_{54\pm 1}\text{Pt}_{46\pm 1}$ thin films annealed for 100 minutes.

In all of the $L1_0$ ordered films, a Pt enrichment at the boundaries of 1σ above the nominal 46 at.% Pt composition exists, as seen in Figures 3.5 and 3.6 and tabulated in Table 3.2. The decreases in this mean value of Pt enrichment followed the increase in the higher order parameters. As more Pt is incorporated back into the bulk of the grain, a higher degree of chemical order would be expected because of the availability of the correct atom type to be in the correct lattice site. Though a subtle decrease in enrichment at the boundaries is observed upon

ordering, each ordered film still maintained some preference of Pt enrichment above the nominal composition. This may be a result that the order parameter did not achieve values near unity.

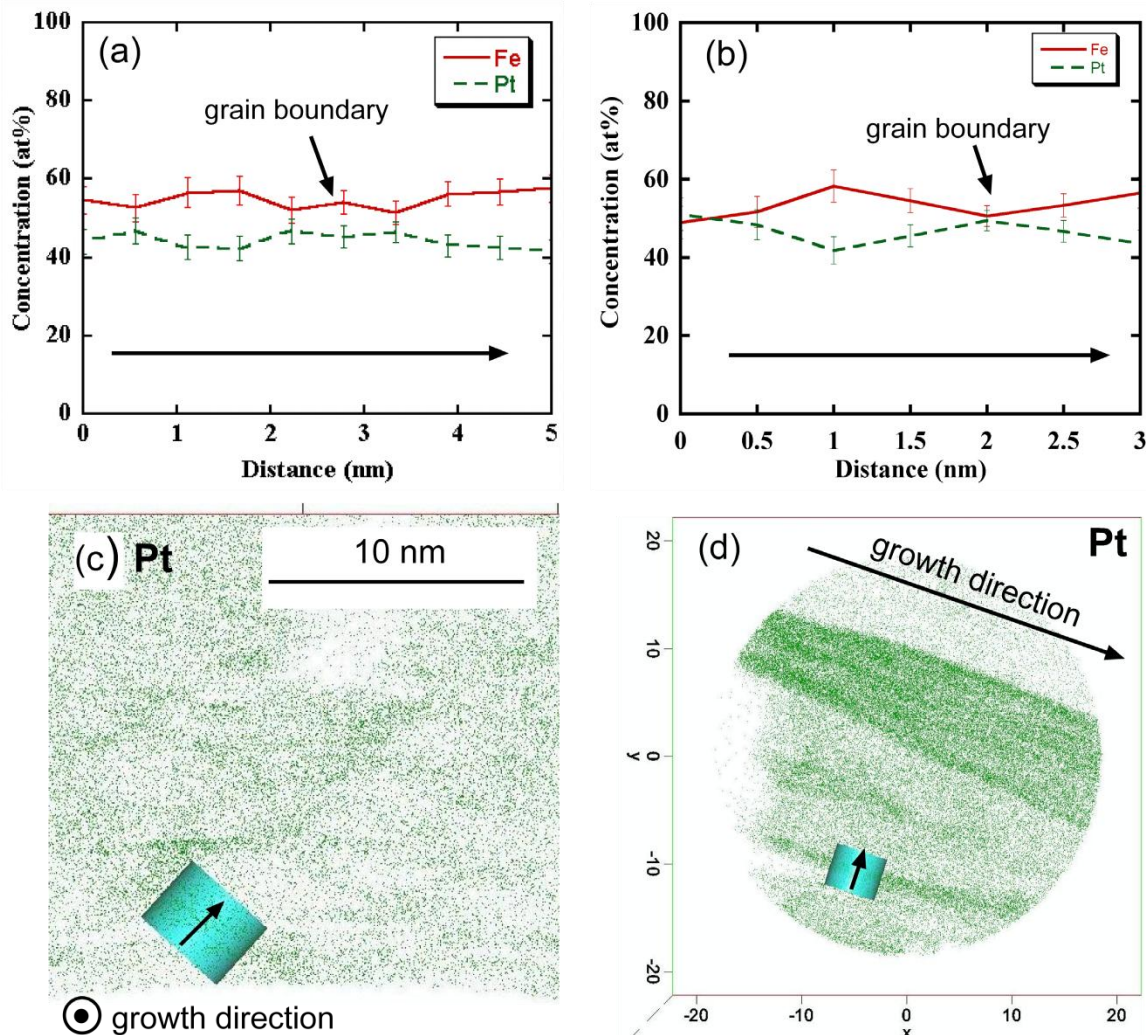


Figure 3. 5. A one-dimensional concentration profile through a grain boundary in (a) the $\text{Fe}_{54\pm 1}\text{Pt}_{46\pm 1}$ thin film annealed at 400°C for 30 minutes and (b) the $\text{Fe}_{54\pm 1}\text{Pt}_{46\pm 1}$ thin film annealed at 350°C for 100 minutes. The solid red line is Fe and the dotted green line is Pt. A Pt atom map indicating the analysis direction and grain boundary used for (c) the $\text{Fe}_{54\pm 1}\text{Pt}_{46\pm 1}$ thin film annealed at 400°C for 30 minutes viewed in plane and (d) the $\text{Fe}_{54\pm 1}\text{Pt}_{46\pm 1}$ thin film annealed at 350°C for 100 minutes viewed in cross-section. The strips are the high density variations along the columnar grain boundaries.

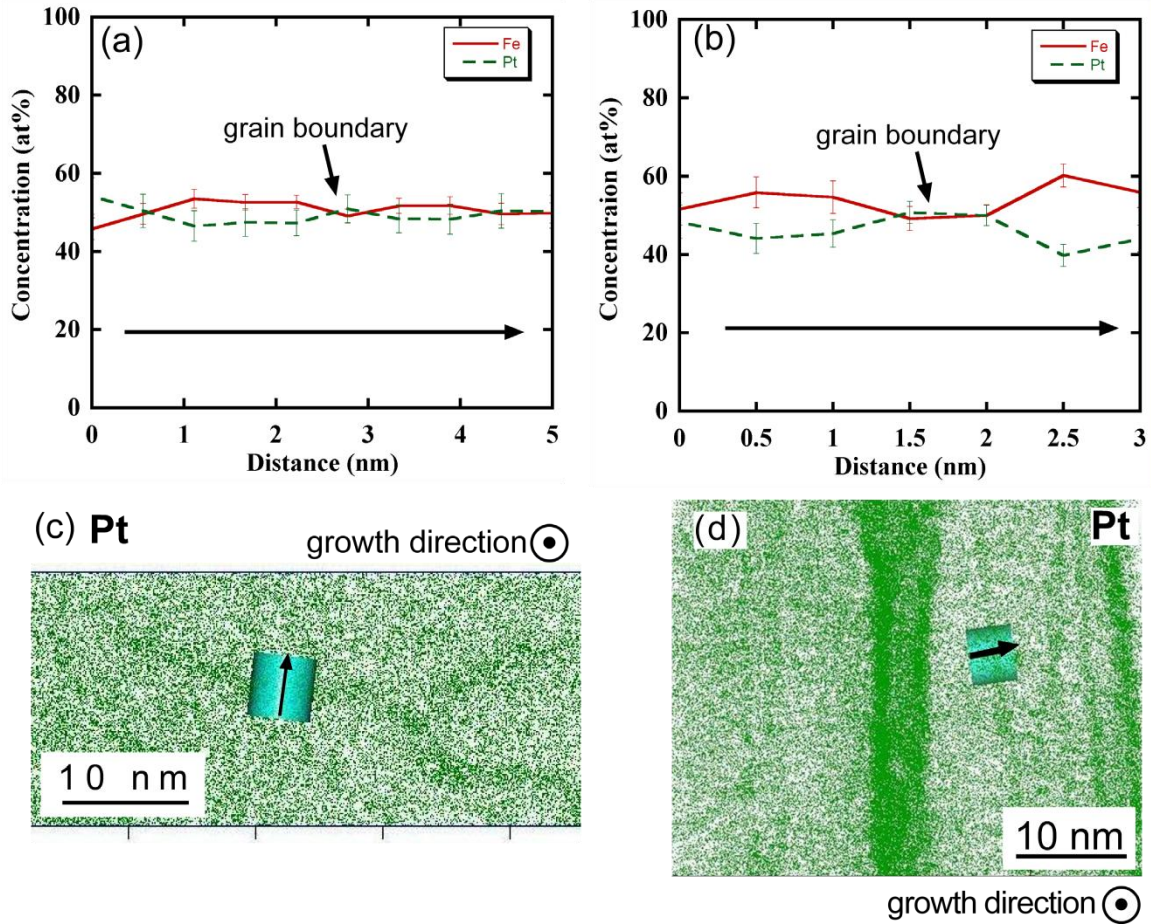


Figure 3. 6. A one-dimensional concentration profile through a grain boundary in (a) the film annealed at 600°C for 30 minutes and (b) the film annealed at 400°C for 100 minutes. The solid red line is Fe and the dotted green line is Pt. A Pt atom map indicating the analysis direction and grain boundary used for (c) the $\text{Fe}_{54\pm 1}\text{Pt}_{46\pm 1}$ thin film annealed at 600°C for 30 minutes viewed in plane and (d) the $\text{Fe}_{54\pm 1}\text{Pt}_{46\pm 1}$ thin film annealed at 400°C for 100 minutes viewed in cross-section. The strips are the high density variations along the columnar grain boundaries.

3.4 Conclusion

A series of $\text{Fe}_{54\pm 1}\text{Pt}_{46\pm 1}$ films were sputter-deposited between silicon nitride layers. The films were characterized by x-ray and electron diffraction and atom probe tomography in the as-deposited and annealed conditions. The annealing was done at various times and temperatures that facilitated the A1 to $L1_0$ phase transformation. The as-deposited A1 phase indicated a preferential segregation of Pt to the grain boundaries of 2σ above that of the nominal 46 at.% Pt

concentration within the film. This enrichment of Pt at the grain boundaries is in agreement to modeling predictions for Pt surface segregation. The atom probe data sets provide experimental verification of these modeling predictions. Upon phase transforming to $L1_0$, the Pt grain boundary enrichment decreased. The extent of Pt depletion from the grain boundaries was dependent upon the annealing times and temperatures, with longer times and higher temperatures resulting in less Pt at the boundary.

3.5 References

- [1] D. Weller, A. Moser, L. Folks, M.E. Best, W. Lee, M.F. Toney, M. Schwickert, J.U. Thiele, and M.F. Doerner, *IEEE Transactions on Magnetics* 36 (2000) 10.
- [2] D. Weller and A. Moser, *IEEE Transactions on Magnetism* 35 (1999) 4423.
- [3] B. Zhang and W.A. Soffa, *Scripta Metallurgica et Materialia* 30 (1994) 683.
- [4] M.F. Toney, W. Lee, J.A. Hedstrom, and A. Kellock, *Journal of Applied Physics* 93 (2003) 9902.
- [5] C.M. Kuo, P.C. Kuo, and H.C. Wu, *Journal of Applied Physics* 85 (1999) 2264.
- [6] B. Yang, M. Asta, O.N. Mryasov, T.J. Klemmer and R.W. Chantrell, *Scripta Materialia* 53 (2005) 417.
- [7] R.V. Chepulskii and W.H. Butler, *Physical Review B* 72 (2005) 134205- 1.
- [8] C. Srivastava, J. Balasubramanian, C. Turner, J. Wiest, H. Bagaria, and G. Thompson, *Journal of Applied Physics* 102 (2007) 104310-1.
- [9] T.J. Klemmer, C. Liu, N. Shukla, X.W. Wu, D. Weller, M. Tanase, D.E. Laughlin, and W.A. Soffa, *Journal of Magnetism and Magnetic Materials* 266 (2003) 79.
- [10] W.A. Soffa and D.E. Laughlin, *Acta Materialia* 37 (1989) 3019.
- [11] K. Barmak, J. Kim, D.C. Berry, W.N. Hanani, K. Wierman, E.B. Svedberg, and J.K. Howard, *Journal of Applied Physics* 97 (2005) 024902-1.
- [12] Y.K. Takahashi and K. Hono, *Scripta Materialia* 53 (2005) 403.

- [13] R.F.C. Farrow, D. Weller, R.F. Marks, M.F. Toney, S. Hom, G.R. Harp, and A. Cebollada, *Applied Physics Letters* 69 (1996) 1166.
- [14] X.H. Li, B.T. Liu, W. Li, H.Y. Sun, D.Q. Wu, and X.Y. Xhang, *Journal of Applied Physics* 101 (2007) 093911-1.
- [15] D.A. Porter and K.E. Eaterling, *Phase Transformations in Metals and Alloys*, CRC Press, Boca Raton (2004) 98.
- [16] D.C. Berry and K. Barmak, *Journal of Applied Physics* 101 (2007) 014905-1.
- [17] B. Rellinghaus, E. Mohn, L. Schultz, T. Gemming, M. Acet, A. Kowalik, and B. Kock, *IEEE Trans. Mag.* 42 (2006) 3048.
- [18] Y.K. Takahashi, T. Ohkubo, M. Ohnuma, and K. Hono, *Journal of Applied Physics* 93 (2003) 7166.
- [19] Y.K. Takahashi, T. Koyama, M. Ohnuma, T. Ohkubo, and K. Hono, *Journal of Applied Physics* 95 (2004) 2690.
- [20] T. Saito, O. Kitakami, and Y. Shimada, *Journal of Magnetism and Magnetic Materials* 239 (2002) 310.
- [21] C.-B. Rong, D. Li, V. Nandwana, N. Poudyal, Y. Ding, Z.L. Wang, H. Zeng, and J. P. Liu, *Advanced Materials* 18 (2006) 2984.
- [22] JCPDS-International Center for Diffraction Data, Card No. 03-065-9121 (2005).
- [23] K. Thompson, D. Lawrence, D.J. Larson, J.D. Olson, T.F. Kelly and B. Gorman, *Ultramicroscopy* 107 (2007) 131.
- [24] M.K. Miller, *Atom Probe Tomography: Analysis at the Atomic Level*, Kluwer Academic/Plenum Publishers, New York (2000) 161.
- [25] K.L. Torres, C. Srivastava, R.L. Martens, and G.B. Thompson, *Materials Research Society Proceedings* 1032E (2008) 1032-I14
- [26] M.K. Miller, A. Cerezo, M.G. Hetherington, and G.D.W. Smith, *Atom Probe Field Ion Microscopy*, Clarendon Press, Oxford (1996) 196.
- [27] M.K. Miller and M.G. Hetherington, *Surface Science* 246 (1991) 442.
- [28] M. Thuvander and H.-O. Andrén, *Materials Characterization* 44 (2000) 87.

CHAPTER 4

FIELD EVAPORATION BEHAVIOR IN [001] FEPT THIN FILMS³

Abstract

Though the atom probe has provided unprecedented atomic identification and spatial imaging capability, the basic reconstruction assumption of a smooth hemispherical tip shape creates significant challenges in yielding high fidelity chemical information for atomic species with extreme differences in fields required for field evaporation. In the present study, the evaporation behavior and accompanying artifacts are examined for the super-cell lattice structure of $L1_0$ FePt, where alternating Fe and Pt planes exist in the [001] orientation. Elemental Fe and Pt have extreme differences in field strengths providing a candidate system to quantify these issues. The reconstruction of field evaporation experiments has shown a depletion of Fe at the (002) pole and zone axes. Compositional profiles revealed an increase in Fe and atom count moving outward from the pole. Field ion microscopy images between 30 K and 110 K revealed little to no surface migration or depletion of Fe at the (002) pole. Thus, the depletion at the low indexed pole and zone axes was determined to be the result of local magnification and electrostatic effects. The experimental results are compared to an electrostatic simulation model.

³ A manuscript has been prepared for the work in this chapter for publication in *Ultramicroscopy* as: K.L. Torres, B. Geiser, M.P. Moody, S.P. Ringer, and G.B. Thompson, "Field Evaporation Behavior in [001] FePt Thin Films."

4.1. Introduction

Atom probe tomography is a three-dimensional reconstruction technique which, in general, is based upon a simple reconstruction procedure that incorporates a hemispherical field emitter and homogeneous evaporation rates at the tip surface [1-2]. As a consequence, atomic species that require dramatically different evaporation field strengths within the same tip suffer from trajectory aberrations, local magnification effects and preferential evaporation artifacts [1-5]. To improve the fidelity of reconstructions, atom probe data sets can be compared to TEM tomography reconstructions and/or simulations of the evaporation sequence [5-9]. In terms of the latter, simulations provide insights into how the aberrations develop. This allows for the development of new reconstruction procedures that can be applied to the experimental data to minimize, or even eliminate, the artifacts in the reconstruction. Previously, it has been observed that morphology and orientation between phases has an effect on the ion trajectory aberrations [7-9]. Angenete *et al.* [3] observed enrichment of Ni near the {001} pole in β -NiAl; Vurpillot *et al.* [5] observed trajectory overlaps of magnifications in FeCo/Cu multilayers; Marquis and Vurpillot [7] observed small shifts in relative positions of matrix and precipitate atoms; and Blavette *et al.* [8] studied trajectory overlaps of Cu precipitates in an irradiated Fe-Cu system. In this work, the authors use atom probe tomography, field ion microscopy, and simulations to understand how the aberrations in crystallographically oriented FePt thin films develop and degrade chemical-structure quantification.

The ordered $L1_0$ phase of FePt was selected because the elemental species of Fe (33 V/nm) and Pt (44 V/nm) have sufficiently large differences in elemental evaporation fields, which would promote the aforementioned issues [1]. The $L1_0$ structure consists of alternating atomic planes of Fe and Pt in the [001] providing an atomic scale superlattice structure. Though

$L1_0$ FePt can be considered a simple lattice structure, the results below reveal significant aberrations and reconstruction issues in providing atomic scale quantification. An advantage of thin films, for this type of study, is that the crystallographic texture can be controlled through proper substrate selection and deposition conditions and the degree of order can be controlled by the annealing temperature. Collectively, this provides tunable variables to study materials dependent field evaporation behavior.

4.2 Materials and Methods

A 200 nm FePt film was co-sputter deposited using commercially pure elemental Fe and Pt targets in an AJA ATC 1500-F chamber. Prior to deposition, the sputtering chamber was evacuated to a base pressure of $< 6 \times 10^{-6}$ Pa. Ultra-high purity Ar, which served as the working gas for sputtering, was flowed into the chamber at 10 standard cubic centimeters per minute to a pressure of 0.27 Pa during sputtering. To promote the [001] $L1_0$ orientation, a 2 μm Cr(Ru) seed layer was deposited onto an MgO [001] substrate heated to 350°C. A subsequent 5 nm Pt diffusion barrier layer, also deposited at temperature to promote the [001] orientation, was grown between the Cr(Ru) and FePt films to prevent a reaction of Cr into the FePt film. The Cr(Ru) film provided a conductive, thick film which could be easily extracted off the MgO substrate and mounted as a standalone atom probe tip. The final structure was MgO/Cr(Ru)/Pt/FePt.

To prepare the specimens appropriate for atom probe tomography (APT) and field ion microscopy (FIM) analysis, a focused ion beam (FIB)-based lift-out technique was used [10-11]. The procedure was performed in an FEI Quanta 3D dual electron beam – focus ion beam (FIB) microscope with initial milling at 30 keV and final milling at 5 keV. The low keV milling

reduces the Ga implantation damage in the film. FIM and APT collection were done in an Imago Scientific Instruments LEAP-3000XSiTM [12]. The FIM images were acquired using ultra-high purity He imaging gas at a pressure of 1.0×10^{-6} Pa. The tip temperature was adjusted from 30K to 110K to investigate thermal assisted surface migration. Initially, APT analysis was performed using voltage pulsing at 80K with a pulse fraction of 25% and a pulse repetition of 200 kHz. A propensity of fracture failures occurred during these experiments resulting in small data acquisitions. Subsequently, APT analysis was performed at 30K with pulse energy of 0.2 nJ and a pulse repetition rate of 250 kHz.

4.3 Results and Discussion

An in-depth slice of the reconstructed Fe positions shown in Figure 4.1(a) reveals a depletion of Fe near the (002) pole and along the zone lines extending from the pole. A 1-D compositional profile along the [001] is shown in Figure 4.1(b) that quantifies the amount of Fe depletion within a 5 nm x 5 nm region centered on the pole. Rational for these density fluctuations will be discussed in the subsequent simulation section below. Aberrations, such as the observed depletion, are expected to occur when evaporation fields between elemental species differ more than 10% [5], which is the case for elemental Fe and Pt. The depletion of Fe at the (002) pole in Figure 4.1(a) may be explained in terms of this evaporation field strength. The lower evaporation field of Fe could cause Fe atoms near the low indexed pole to experience uncontrolled DC evaporation after the removal of Pt atoms [13]. To elucidate the mechanisms of Fe depletion near the (002) pole and along the zone axes, APT analysis, FIM imaging and simulations of the field evaporation of [001] FePt were utilized.

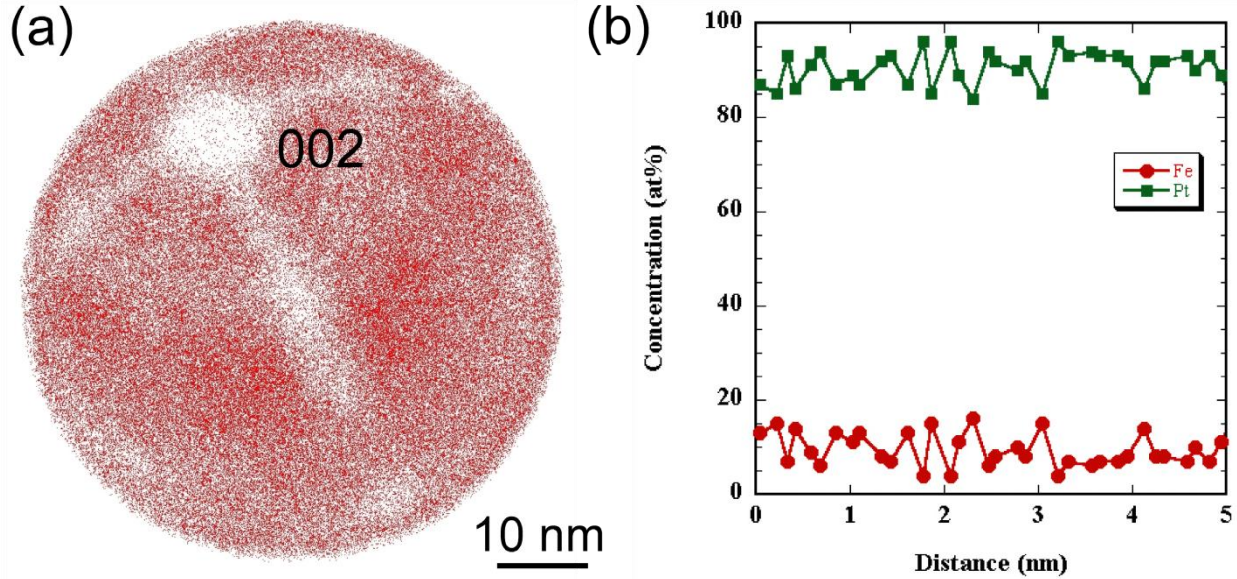


Figure 4. 1. (a) Fe atom map showing depletion at the (002) pole and the zone axes. (b) APT analysis of FePt film along the [001]-direction.

4.3.1 Field Evaporation of (001) planes

The methodology presented by Gault *et al.* [14] was utilized for the APT reconstructions. The density of atoms at the (002) pole was considerably lower than regions away from the pole as shown in Figure 4.2(a). These atomic density fluctuations can be attributed to local magnification effects near the low index pole. As the atomic terrace diameter decreases during field evaporation, the divergence of ion trajectories increases [1,15]. Additionally, measurements of the total average concentration of atoms within a cylinder centered on the (002) pole with an increasing cross-sectional radius were obtained. In Figure 4.2(b), a linear increase in Fe concentration towards the nominal $\text{Fe}_{51}\text{Pt}_{49}$ film composition was observed away from the pole. Again, local magnification effects contribute to the displacement of Fe from the (002) pole. Highly depleted regions of low evaporation field species have been observed in FeAl ordered alloys [16] and β -NiAl alloyed with Pt [3] which is consistent with our experimental results.

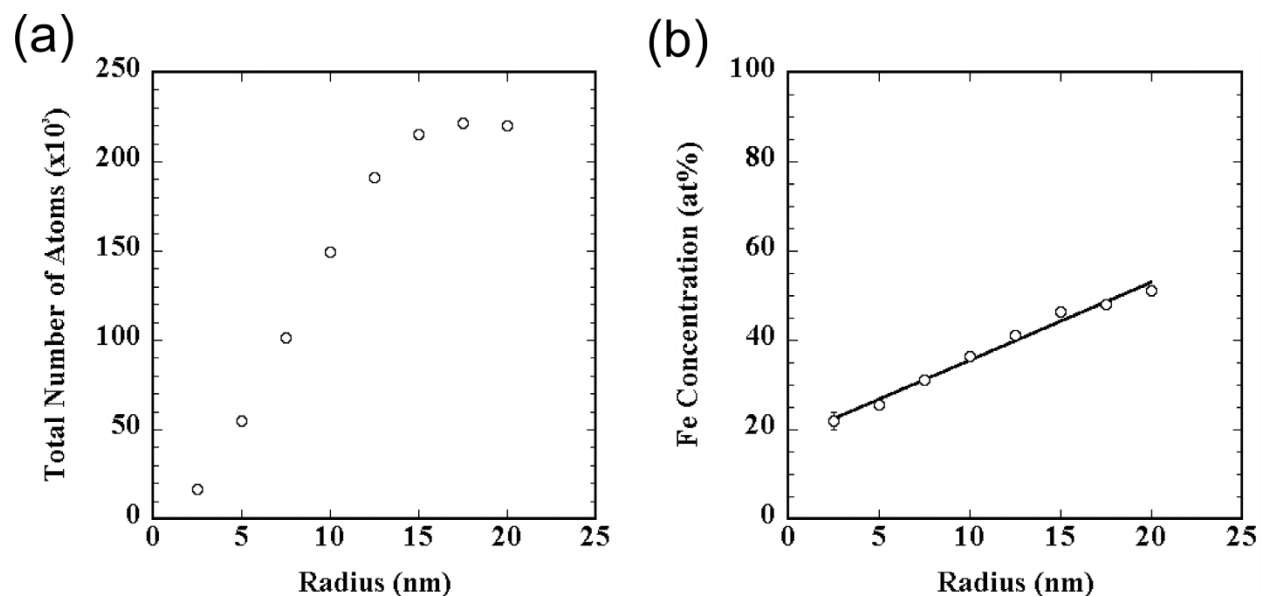


Figure 4. 2. (a) Total number of atoms as a function of radial distance from the (002) pole. (b) Fe concentration as a function of radial distance away from the pole.

The images in Figure 4.3(a) and Figure 4.3(b) show the reconstructed positions of Fe and Pt at a location away from the pole. The Pt planes are not as sharp as the Fe planes in the reconstruction. This is attributed to the drastically different evaporation fields of the two species. Others have noted this observation in the reconstruction of alloys with differing evaporation fields [3-4]. The blurring of the Pt planes is an effect of these planes being bent, while the Fe planes remain flat [15]. The observed effect is caused by the inability to select a single geometrical field factor to appropriately account for the difference in evaporation fields of the two species in the 3D reconstruction model. A 1-D compositional profile, shown in Figure 4.3(c), along the [001]-direction was evaluated for compositional variations within the planes. The analysis did not reveal individual layers of Pt and Fe. To evaluate the chemical environment surrounding the atoms near the (002) pole, spatial distribution maps (SDMs) were used. The methodology for obtaining the SDMs is described in a previous publication by Moody *et al.* [17]. SDM analysis shown in Figure 4.4(a) indicates Pt planes are well resolved with respect to Pt

atoms. Fe planes are also well resolved with respect to Fe atoms. However, in Figure 4.4(b) Pt planes are not well resolved with respect to Fe atoms. The analysis also indicates plane spacing has a directional dependence in-depth; Pt planes in the negative z-direction are spaced closer than the adjacent Pt planes in the negative z-direction with respect to the Fe reference plane. Furthermore, the analysis reveals that there are no individual planes of Fe and Pt. The apparent mixing of the planes does not represent a disordered alloy. Rather this ‘mixing’ is caused by the inability to correctly reconstruct the acquired data.

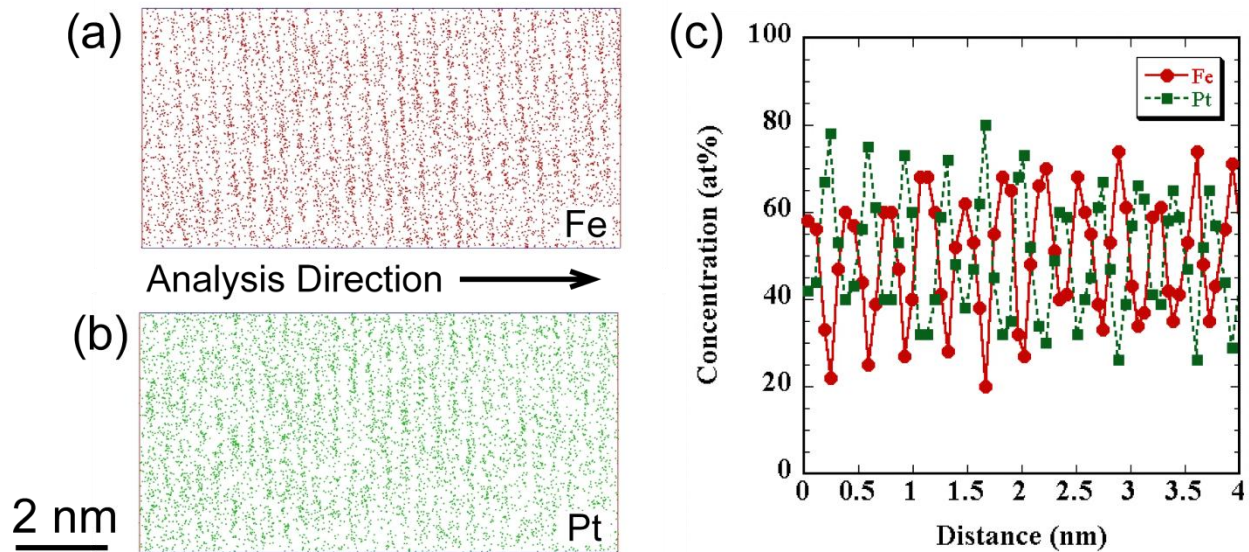


Figure 4. 3. (a) Fe atom map with sharp planes observed. (b) Pt atom map with blurred planes observed. (c) 1-D composition profile along the ordered direction. Fe is depicted in red and Pt is depicted in green.

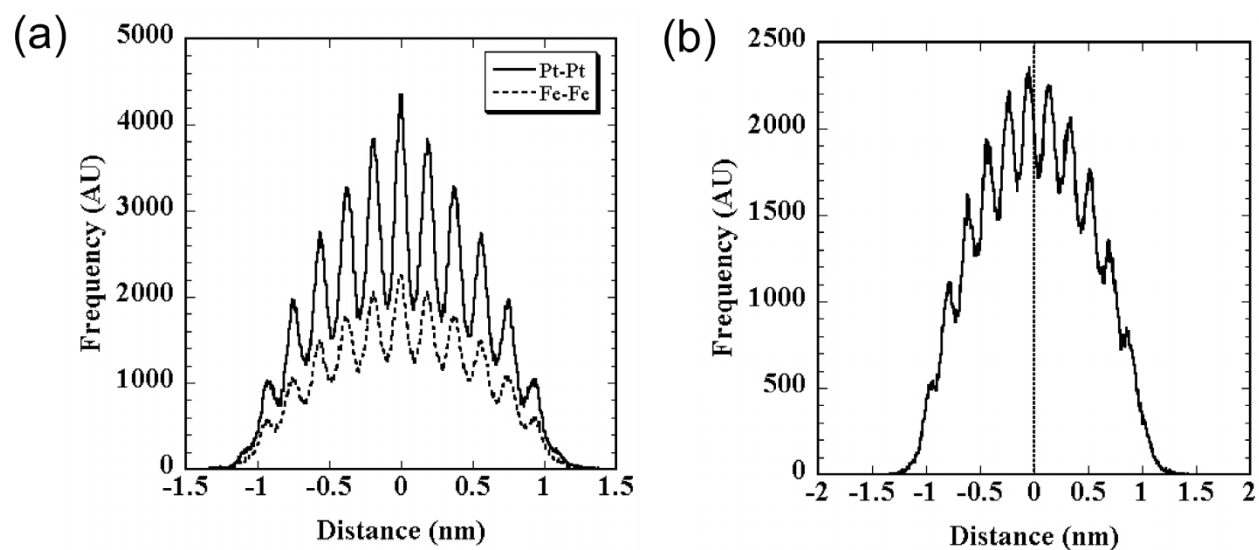


Figure 4. 4. Spatial distribution maps from an 8 nm diameter region centered at the (002) pole. **(a)** The SDM shows the z-distance from Pt to Pt planes using a solid black line and Fe to Fe planes in a dashed black line. **(b)** The z-distances of Pt planes with respect to Fe atoms.

To determine if surface migration of either Fe or Pt could contribute to the observed depletion, a series of FIM experiments were performed on the surface evolution of the tip. The tip temperatures for this study ranged from 30K to 110K. The alternating bright and dim rings are visible close to the (002) pole in Figure 4.5. Previous studies of ordered FePt have shown that at the (002) pole, the bright rings correspond to Pt planes and the dim rings to Fe planes [18]. The brighter appearance of the Pt atoms is attributed to the higher evaporation field of Pt. However, a depletion of Fe at the (002) pole and zone axes was not observed in these experiments. Surface migration was considered not to be a contributing factor in the Fe depleted regions in the above reconstruction.

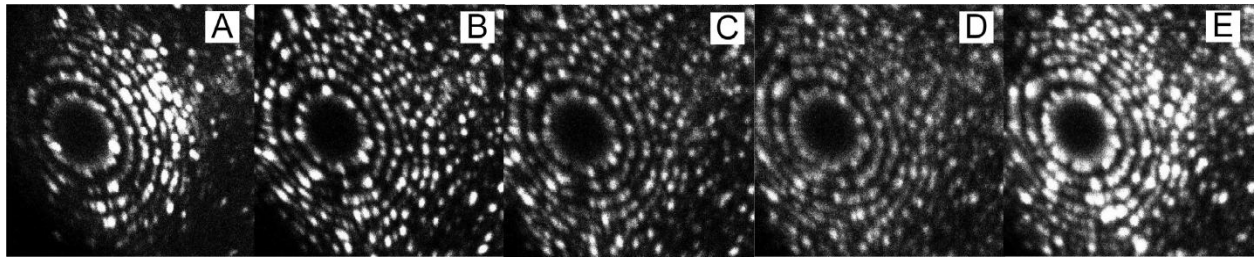


Figure 4. 5. FIM images of the (002) FePt pole at (a) 30K, (b) 50K, (c) 70K, (d) 90K, (e) 110K. Only the Pt atoms are imaged in these micrographs.

4.3.2 Simulation of Atom Probe Images

The TipSIM software tool by Cameca Instruments was used to simulate an atom probe data acquisition during field evaporation and investigate the trajectory aberration reconstruction artifacts in the ordered FePt alloy. The TipSIM model is based on a three-dimensional representation of a needle-shaped geometry with a hemispherical end form. The primary evaporation simulation is an evolving electrostatic simulation based on a finite difference relaxation solution of Poisson's equation [1]. The initial radius of curvature was 20 nm. To simplify the model geometry, the FePt alloy was assumed to have a face centered cubic structure rather than the tetragonal $L1_0$ lattice structure. Note that the ordered FePt has a c/a ratio of 0.97 making this a reasonable assumption. To emulate the experiment, the crystal structure of the tip was oriented in the [001]-direction. With this orientation, the tip surface consisted of a stack of alternating (001) terraces of Fe and Pt with a single atom occupying a cubic grid. After the tip geometry was defined, the electric potential distribution within the simulation volume was calculated using a multi-grid method. More detailed discussion of this method can be found in reference [19]. To determine the atoms to evaporate, a maximum field method was used. Thus, the atom submitted to the highest field was considered to be the first to field evaporate. The atom was virtually removed after which the electric field potential on the new created tip surface was

updated and the new field distribution above the tip surface was recalculated. The ion trajectory was then calculated and the impact position on the simulated detector was determined. After the trajectory of the ion was calculated, the next atom with the highest electric field was considered and the process repeated.

The simulation evaporated 30,000 atoms from the field emitter. This accounts for approximately 12 atomic layers. The initial 3D representation of the morphology of the tip surface and the first 3000 atoms successively evaporated are shown in Figure 4.6(a). The atoms originate from the defined zones of the sample surface where the electric field is the highest. Figure 4.6(b) also shows the last 3000 atoms evaporated. With successive evaporations, the tip gradually changed to a faceted geometry. The results demonstrate that the equilibrium shape of the tip, when evaporated, is not a hemispherical cap. Rather, the emitter has developed faceted features which are consistent with experimental results shown in Figure 4.6(c). The radius of curvature becomes larger for high atom density planes. These regions experience lower evaporation fields, thus yielding larger facets. Vurpillot *et al.* [20] have reported similar results in simulations of ordered alloys using a simple cubic geometry oriented in the [001].

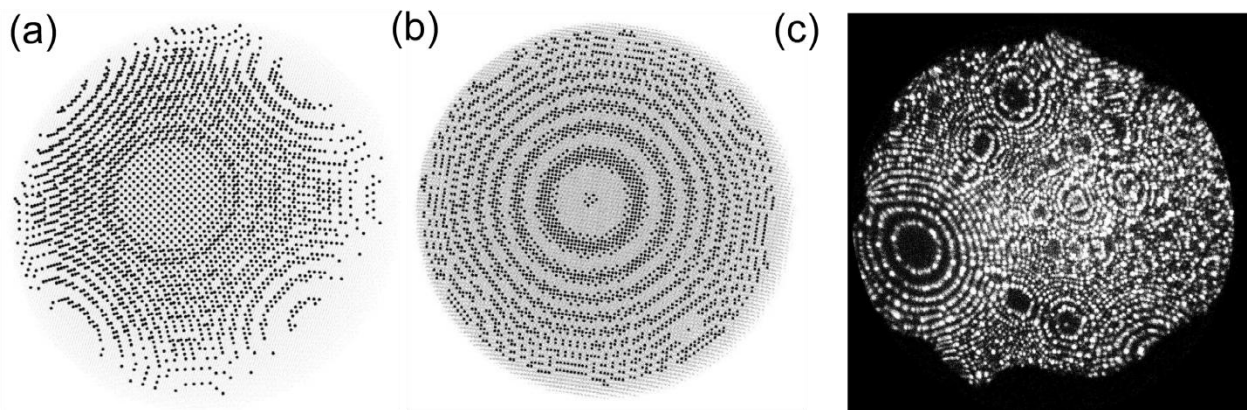


Figure 4. 6. (a) Initial tip shape with the first 3000 atoms evaporated highlighted in black. (b) Final tip shape with the last 3000 atoms evaporated highlighted in black. (c) FIM image after field evaporation demonstrating faceting of the tip surface.

The 2D distribution of the ion impacts of Pt and Fe are represented in Figure 4.7 (a) and (b) respectively. The model predicts the presence of depleted zones at the center of the low index pole. Denuded lines were also observed along the zone axes which are characteristic of the crystallography of the long-range order of the alloy [13,20]. The depleted and enriched zones are attributed to the evaporation sequence. In pure metals, depleted zone axes observed along the $\langle 001 \rangle$ directions are a result of edge atoms evaporating from $\langle 100 \rangle$ rows [13]. Deviations of the ion are caused by neighbors in edge positions in the row. The bright lines in the center of the depleted zone are attributed to the last atoms to be evaporated from the row. These atoms have no neighbors in the row and will have no deviations from the $\langle 001 \rangle$ direction. This can also be extended to the FePt alloy. For example, Figure 4.8 is the evaporation sequence of the final 12 Pt atoms on a single Pt terrace in our simulation. The kink sites are observed to evaporate first. Eventually, a single Pt atom remains on the atomic terrace. Thus, the ion will not be significantly deviated from the $\langle 001 \rangle$ direction. This would also extend to Fe atoms on the subsequent layer. The face centered cubic model geometry has qualitatively reproduced experimental findings without a binding term or thermal effects.

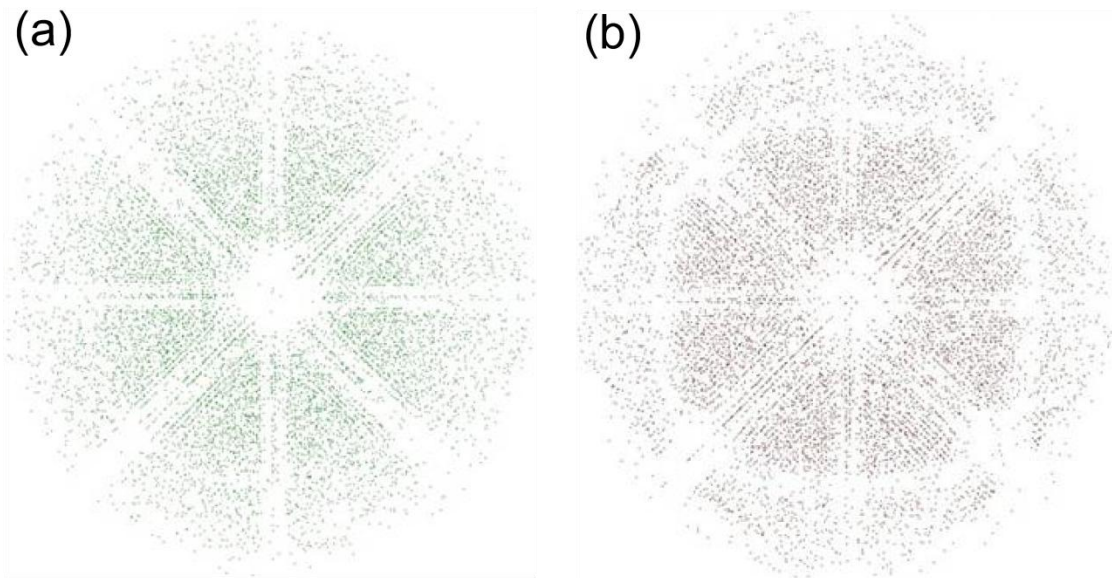


Figure 4. 7. (a) Image of the high evaporation field species (Pt) in an ordered alloy. (b) Same image obtained for the low evaporation field species (Fe). The images exhibit bright lines within the zone axes. Also note the low atomic density at the (002) pole.

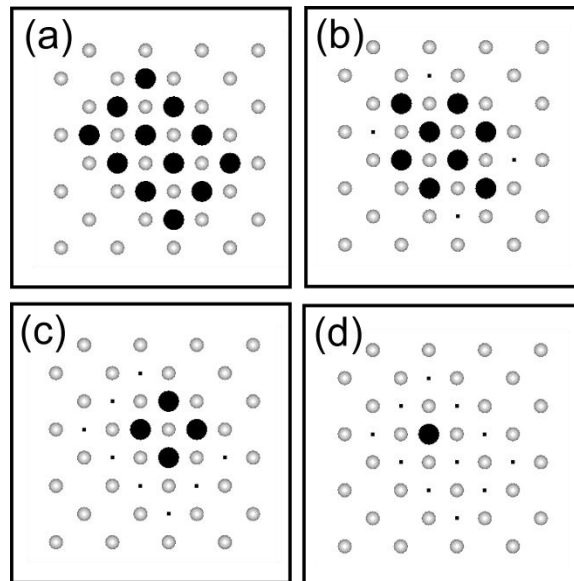


Figure 4. 8. The evaporation sequence of an atomic terrace. The low evaporation atoms (Fe) are shown in grey and the high evaporation atoms (Pt) are shown in black. The grey (Fe) atoms are shown to exhibit the crystal structure and are located below the black (Pt) atoms. Evaporated Pt atoms are represented by black squares. (a) The twelve Pt atoms on the atomic terrace. (b) Four corner atoms have been removed from the terrace. (c) Four kink site atoms have been removed from the terrace. (d) Final Pt atom after 3 kink site Pt atoms were evaporated.

In Figure 4.9, small reconstructed volumes of both the simulation and experiment are shown. The volumes are oriented to display the stacking sequence of (001) planes. In good agreement with experiment, the planes of the high and low evaporation atoms are observed to merge with one another. The uncontrolled evaporation of Fe immediately following Pt could contribute to the overlay of Fe atoms on the Pt planes. Furthermore, small perturbations from the ideal hemispherical tip shape imposed during reconstruction could also contribute to the merging of the planes in the FePt reconstruction.

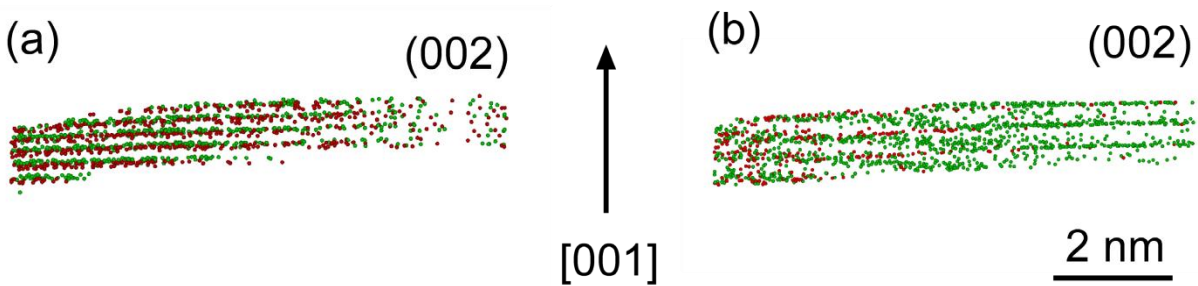


Figure 4. 9. (a) 3D reconstruction of FePt obtained from simulated trajectories. Approximately 20 atomic (001) planes were evaporated. The high evaporation atoms (Pt) are shown in green and the low evaporation atoms (Fe) are shown in red. (b) An experimental reconstruction of FePt. The image exhibits the same aberrations as simulations.

4.4 Conclusions

Ordered FePt was investigated using FIM and APT to study the field evaporation behavior of the (001) planes. During field evaporation, it was found that close to the (002) pole, the number density of Fe ions detected was significantly lowered because of ion trajectory aberration effects. Simulations incorporating a face center cubic structure have qualitatively reproduced the experimental findings without the inclusion of a binding term or thermal effects. Both experimental and simulation results have shown that the difference in evaporation field

between the two components of the alloy contributed to the trajectory aberrations near the (002) pole and zone axes. The modeled system used in this paper has shown that chemical order within a structure introduces aberrations in the reconstruction of the atomic planes limiting the spatial and chemical fidelity of characterizing such structures using current reconstruction methodologies.

4.5 References

- [1] M.K. Miller, A. Cerezo, M.G. Hetherington, and G.D.W. Smith, *Atom Probe Field Ion Microscopy*, Oxford Science Publications, Oxford, 1996.
- [2] P. Bas, A. Bostel, B. Deconihout, and D. Blavette, *Appl. Surf. Sci.* 87/88 (1995) 298-304.
- [3] J. Angenete, K. Stiller, and F. Danoix. *Mater. Sci. Eng.* A353 (2003) 68-73.
- [4] T. Boll, T. Al-Kassab, Y. Yuan, Z.G. Liu, *Ultramicroscopy* 107 (2007) 796-801.
- [5] F. Vurpillot, D. Larson, and A. Cerezo, *Surf. Interface Anal.* 36 (2004) 552-558.
- [6] E.A. Marquis, M.K. Miller, D. Blavette, S.P. Ringer, C.K. Sudbrack, and G.D.W. Smith, *Mater. Res. Bull.* 34 (2009) 725-730.
- [7] E.A. Marquis and F. Vurpillot, *Microscopy and Microanalysis* 14 (2008) 561-570.
- [8] D. Blavette, F. Vurpillot, P. Pareige, and A. Menand, *Ultramicroscopy* 89 (2001) 145-153.
- [9] F. Vurpillot, A. Bostel, and D. Blavette, *Appl. Phys. Lett.* 76 (2000) 3127-3129.
- [10] M.K. Miller, K.F. Russell, and G.B. Thompson, *Ultramicroscopy* 102 (2005) 287-298.
- [11] K. Thompson, D. Lawrence, D.J. Larson, J.D. Olson, T.F. Kelly, and B. Gorman, *Ultramicroscopy* 107 (2007) 131-139.
- [12] T.F. Kelly, T.T. Gribb, J.D. Olson, R.L. Martens, J.D. Shepard, S.A. Wiener, T.C. Kunicki, R.M. Ulfing, D.R. Lenz, E.M. Strennen, E. Oltman, J.H. Bunton, and D.R. Strait, *Microscopy and Microanalysis* 10 (2004) 373-383.
- [13] F. Vurpillot, A. Bostel, E. Cadel, and D. Blavette, *Ultramicroscopy* 84 (2000) 213-224.

- [14] B. Gault, M.P. Moody, F. de Geuser, G. Tsafnat, A. La Fontaine, L.T. Stephenson, D. Haley, and S.P. Ringer, *J. Appl. Phys.* 105 (2009) 034913.
- [15] M.K. Miller, *Atom Probe Tomography – Analysis at the Atomic Level*, Kluwer Academic / Plenum Publishers, New York, 2000.
- [16] F. Vurpillot, A. Bostel, A. Menand, and D. Blavette, *European Physical Journal of Applied Physics* 6 (1999) 217-221.
- [17] M.P. Moody, B. Gault, L.T. Stephenson, D. Haley, and S.P. Ringer, *Ultramicroscopy* 109 (2009) 815-824.
- [18] U.T. Son and J.J. Hren, *Surface Science* 23 (1970) 177-197.
- [19] W. Hackbusch, *Multi-grid Methods and Applications*, Springer-Verlag, Berlin, 1985.
- [20] Vurpillot, A. Bostel, and D. Blavette, *J. Microscopy* 196 (1999) 332-336.

CHAPTER 5

DYNAMICAL DIFFRACTION SIMULATIONS IN CHEMICALLY ORDERED FEPT⁴

Abstract

A series of multislice simulations to quantify the effect of various degrees of order, composition and thickness on the electron diffracted intensities were performed using the $L1_0$ FePt system as the case study. The dynamical diffraction studies were done in both a convergent electron beam diffraction (CBED) and selected area electron diffraction (SAED) condition. The $L1_0$ symmetry demonstrated some peculiar challenges in the simulation, in particular between the $\{111\}$ plane normal and the $\langle 111 \rangle$ direction, which are not equivalent because of tetragonality. A hybrid weighting function atom was constructed to account for $S < 1$ or non-equiatomic compositions. This statistical approach reduced the complexity of constructing a crystal with the probability that a particular atom was at a particular lattice site for a given order parameter and composition. Considerations of accelerating voltage, convergent angle and thermal effects are discussed. The simulations revealed significant differences in intensity ratios between films of various compositions but equivalent unit cell numbers and degree of order.

⁴ A manuscript has been prepared for the work in this chapter for publication in *Microscopy & Microanalysis* as: K.L. Torres, R.R. Vanfleet, and G.B. Thompson, "Dynamical diffraction simulations in chemically ordered FePt."

5.1 Introduction

The $L1_0$ phase of FePt has been identified as a leading candidate for ultrahigh-density magnetic storage media because of its high magnetocrystalline anisotropy, K_u [1]. The K_u of this alloy was strongly dependent on the long-range order parameter, S , where K_u decreases with decreases in S [2-4]. The most readily available technique to determine S was x-ray diffraction. Unfortunately, for ultra-thin films or nanoparticles, acquiring adequate x-ray diffracted intensities from these small volumes without a synchrotron source can be problematic. Electron scattering can be more amenable for diffraction studies of small volumes, though the strong interaction of electrons with the material results in multiple scattering events. Consequently, the traditional methodology of taking the ratio of the total integrated peak intensities of the superlattice and fundamental reflections according to kinematical scattering theory [5], as done in x-ray diffraction, no longer applies, and S determination becomes more complex. Simulations of electron transmission in crystalline specimens including dynamical scattering are necessary to determine S [6-7]. Figure 5.1 demonstrates the difficulty of predicting S for [001] and [111] directions in FePt using transmission electron microscopy (TEM). Over a thickness of 45 nm in Figure 5.1(a), several oscillations were observed in the intensities of the superlattice and fundamental reflections for $S=0.50$ in the [001] orientation. In Figure 5.1(b), only oscillations of the fundamental reflection in the [111] orientation were observed. Nevertheless, both orientations introduced complexities in quantifying S .

In this study, the multislice simulation approach was used to simulate electron transmission in crystalline thin films including dynamical scattering to determine S . The initial arrangement of the crystal to incorporate composition and S was described. Slicing schemes for $L1_0$ FePt in the [001] and [111] orientations were considered. Finally, the influence of composition, thermal configurations, pixel size, and sampling size on S determination using a

multislice method was discussed. The simulations were done for convergent electron beam diffraction (CBED) and selected area electron diffraction (SAED) conditions.

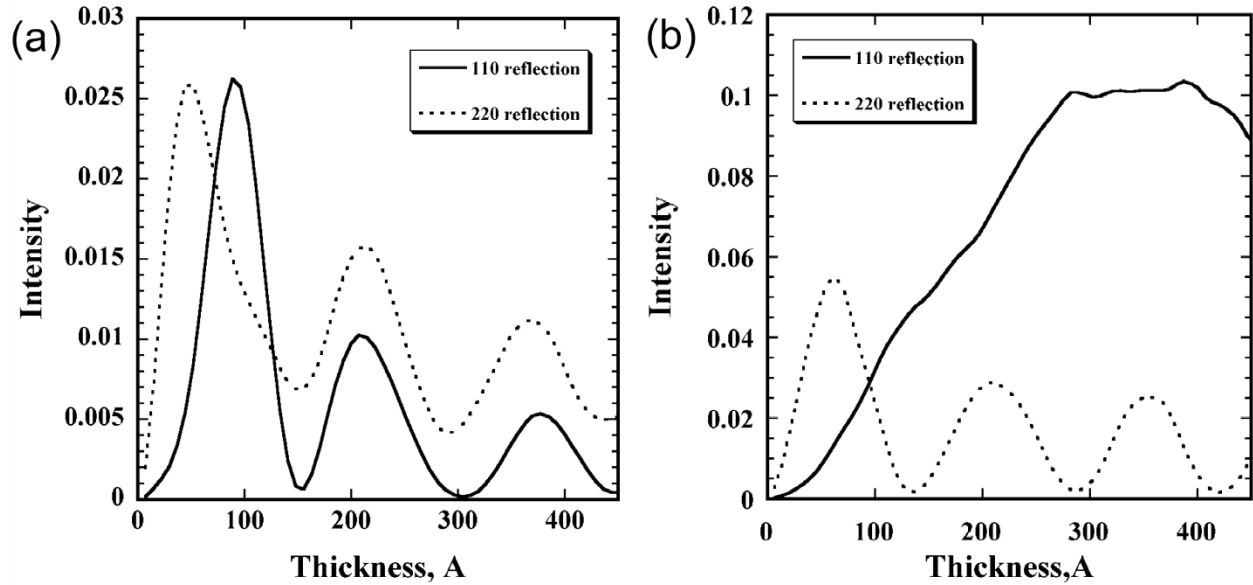


Figure 5. 1. Intensity of the superlattice (110) and fundamental (220) reflections vs. thickness for an order parameter of 0.5 in the (a) [001] orientation and (b) [111] orientation.

5.2 Methods

To simulate dynamical diffraction patterns, a multislice algorithm as outlined by Kirkland [8] was used. The multislice method was first derived by Cowley and Moodie [9] for spot patterns of small, single crystals with no defects. Cowley and Spence extended the multislice methodology to include the simulation of convergent-beam electron diffraction (CBED) patterns [10]. In both approaches the dynamical scattering of electrons was considered from a physical optics viewpoint. Before implementing the Kirkland algorithm, a description of the specimen was required. This was followed by the division of the specimen into thin two dimensional slices along the electron beam direction. The slice must be thin enough to be a weak phase object. In

general, and in the presented approach, this was one atomic layer. The following sections outline simulation input parameters for S quantification.

5.2.1 *Electron Probe*

The focused probe used to form the CBED pattern was represented by a disk in reciprocal space. The angular diameter of the disk was the same as the angular spread of the incident beam as shown in Figure 5.2. The diameter of the disk was determined by the convergence angle, 2α , of the illuminating beam and was taken as the same size of the objective aperture. In the CBED simulations, a focused probe was used as the initial wave function. In the SAED simulations, the initial wave function was taken as a plane wave. The wave function was transmitted through the specimen and the Fourier transform of the exit wave function was the resultant diffraction pattern. The image generated was a rectangular grid of $N_x \times N_y$ pixels. The image was sampled at N_x discrete points along the x-direction and N_y points along the y-direction within the $a \times b$ supercell in real space. Selecting an appropriate sampling size was necessary to reduce computational time and mitigate intensity losses.

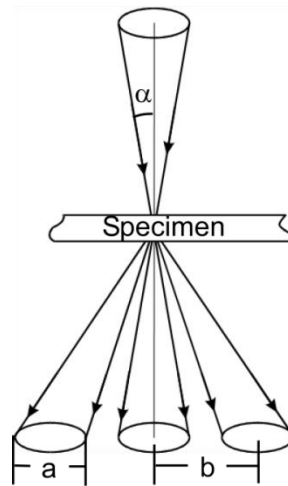


Figure 5. 2. A CBED configuration with a convergence angle 2α . The diameter of the disk is a and b is the 2θ angle between the central disk and a specified reflection.

5.2.2 Specimen Description

The $L1_0$ symmetry was a tetragonal crystal structure consisting of alternating planes of A and B atoms along the c-axis [11]. This has been described as an ordered body centered tetragonal structure [12] and referred, incorrectly, as an ordered face centered tetragonal structure [13], which is not one of the Bravais lattices. Since the phase was tetragonal, the common use of $\{ \}$ or $\langle \rangle$ to represent families of planes or directions cannot be used for all hkl 's. When appropriate, we have designated specific planes, $(\)$, or directions, $[\]$, by the proper notation for hkl 's that are not in the equivalent family. When in the hkl 's are in the equivalent family, the general notation of $\{ \}$ for planes and $\langle \rangle$ for directions was used.

In this study, three parameters alter the description of the $L1_0$ FePt crystal: S , composition, and lattice parameter [14-15]. To properly incorporate S and composition, the implementation of a statistical order parameter was used. The statistical order parameter was based on a hybrid weighted average atom of Fe-Pt, when $S < 1$, on each lattice site rather than assigning an individual Fe or Pt atom to a particular lattice site. In this approach, the exception was for $S=1$ and a stoichiometric $Fe_{50}Pt_{50}$ alloy where pure Fe and Pt are placed at the appropriate lattice sites. This methodology allows easy generation of the structure without the need to consider the probability of a particular atom on a particular lattice site at a specific order parameter. The statistical approach also easily accommodates for non-equiatomic binary compositions. Finally, the lattice parameter was adjusted for composition using Vegard's Law [16].

5.2.3 Slicing Methods

Generating a description of the specimen in slices for implementation of a multislice algorithm can be challenging. There is no general procedure as each specimen may require a

different approach to generate the slicing scheme. The specimen was described by a sequence of layers (x,y planes) perpendicular to the optic axis and the spacing between each layer. Once the specimen was sliced, the atoms within the slice (z to $z+\Delta z$) were compressed into a plane at z . When viewed along the optic axis, it is optimal that each slice be aligned with its natural periodicity in the $x-y$ plane. If the slice does not meet this requirement, artifacts may be generated [8]. However, it is not necessary for the slices to be periodic along the z - or optic axis.

To demonstrate the significance of the slicing procedure, two orientations for $L1_0$ FePt were considered. Initially, the $[001]$ direction was aligned parallel with the optic axis. In this orientation, flat layers of atoms were spaced evenly along z as shown in Figure 5.3. The natural procedure in this orientation was to divide the specimen into atomic layers.

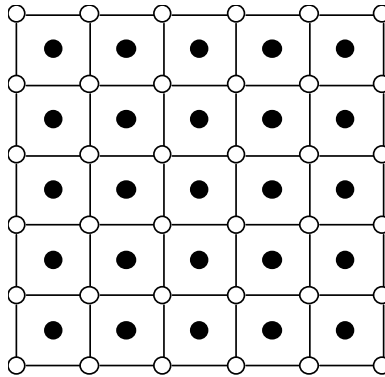


Figure 5. 3. $[001]$ orientation viewed in cross-section to demonstrate the flat layers along the z -direction which is parallel to the optic axis.

The slicing procedure for the $\{111\}$ orientation becomes more complicated because of the tetragonality of the system; the $\{111\}$ plane normal and $\langle 111 \rangle$ direction are not the same crystallographically. The two are more than a degree apart depending on the c/a ratio. Thus, the $\{111\}$ orientation has two possibilities. If the $\{111\}$ planes were aligned perpendicular to the optic axis, the atoms in-depth do not line up as shown in Figure 5.4(a). However, tilting the

crystal 90 degrees in Figure 5.4(b) revealed the layers in this orientation were flat. If the $\langle 111 \rangle$ direction was aligned with the optic axis, the atoms lineup in-depth as seen in Figure 5.4(c). However, when the crystal was tilted 90 degrees, Figure 5.4(d), the layers were slightly tilted along the optic axis. Each option introduced challenges for the multislice simulations. If the $\{111\}$ plane normal was aligned with the optic axis, the periodic boundaries were more difficult to determine, but the slices were flat along the beam direction. Conversely, if the $\langle 111 \rangle$ direction was aligned with the optic axis, the layers of atoms were tilted slightly along z . We have considered both cases below.

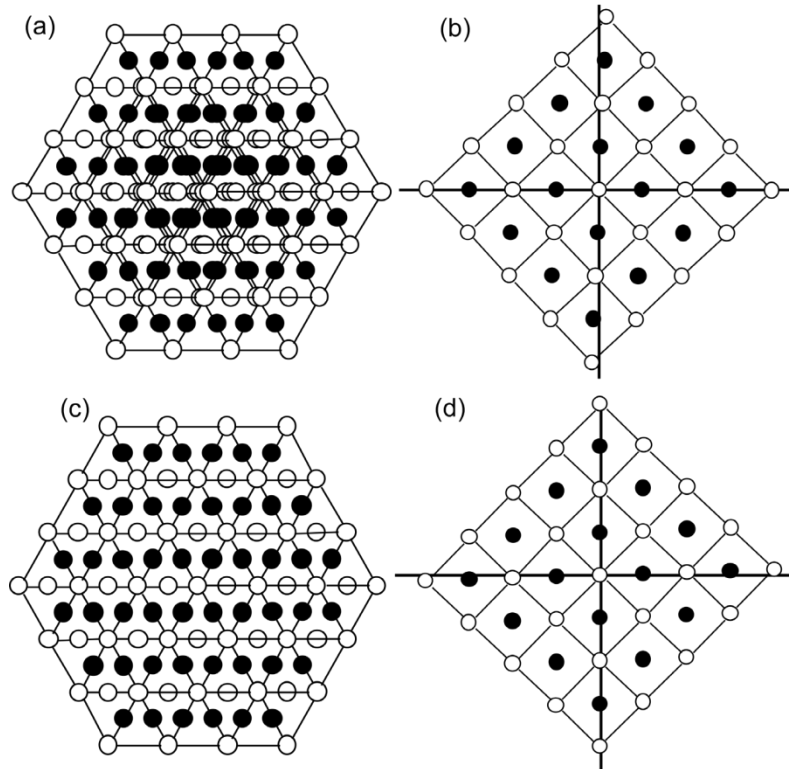


Figure 5. 4. (a) $\{111\}$ planes are aligned perpendicular to the optic axis. The atoms in-depth do not line up. Fe atoms are represented by the unfilled circles and Pt atoms are represented by the solid circles. (b) The crystal is tilted 90 degrees. The layers are flat along the optic axis in this orientation. (c) The $[111]$ direction is aligned with the optic axis and atoms lineup in-depth. (d) The crystal is tilted 90 degrees which reveals the layers are not flat along the optic axis.

5.3 Results and Discussion

As stated previously, the diameter of the disks observed in CBED patterns was related to the convergence angle. However, the convergence angle and accelerating voltage must be considered simultaneously. With a change in accelerating voltage, the spacing between disks also changes. Figure 5.5 illustrates the necessity for choosing an appropriate convergence angle for S quantification. In this case, a convergence angle of 8 mrad was too large for 300 keV. However, the convergence angle was appropriate for 120 keV, 160 keV, and 200 keV. The convergence angle was reduced to 6 mrad at 300 keV to ensure the disks do not significantly overlap and S determination was possible.

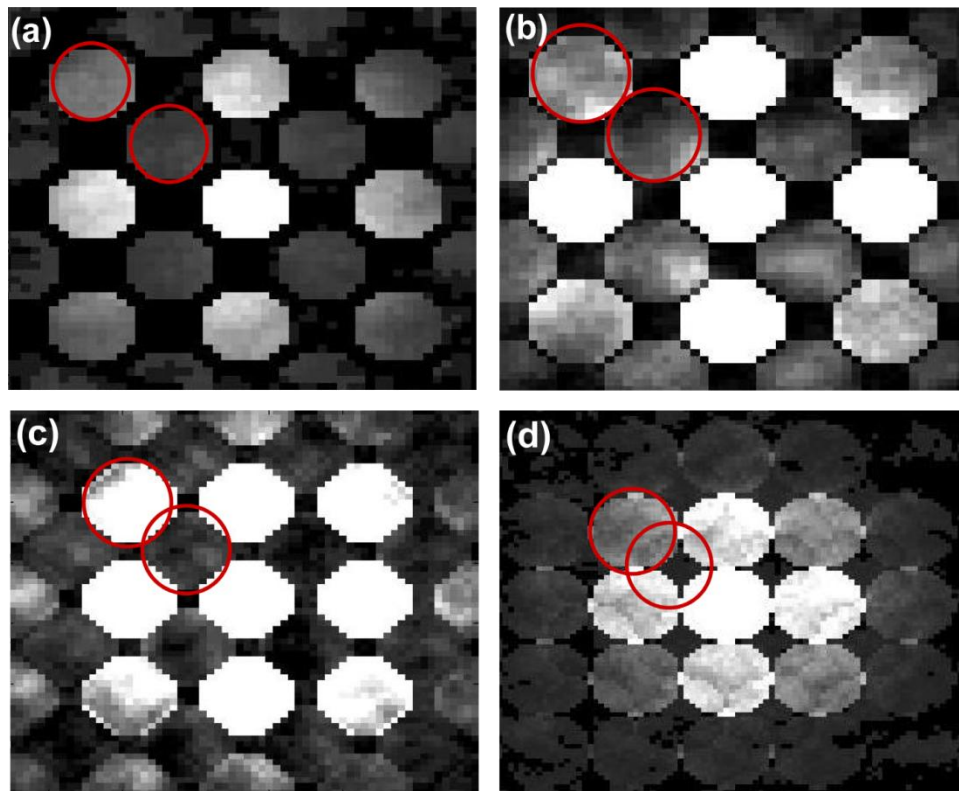


Figure 5. 5. CBED patterns for accelerating voltages at (a) 120 keV (b) 160 keV (c) 200 keV and (d) 300 keV. The convergence angle is 8 mrad for all images. The disks significantly overlap in Figure 5(d).

After an accelerating voltage and correspondingly correct convergence angle was selected, the thickness of the simulated specimen was chosen. Recall, the intensity of the (110) and (220) type reflections fluctuate with respect to thickness (see Figure 5.1). A CBED pattern for each S was required to determine the ratio of intensities of a film with a specified composition and thickness. With a large number of simulations required for S determination, sampling and pixel size of the wave function was increasingly significant. Table 5.1 shows the influence of pixel size for a CBED pattern of a 4.5 nm and 20 nm $\text{Fe}_{50}\text{Pt}_{50}$ film with $S=0.7$. For the thin specimen, using a lower pixel density was adequate. The computational time for a 128 x 128 image was significantly less than that of the 1024 x 1024 image with little loss in intensity for the lower pixel density. However, for the 20 nm sample a significant loss in intensity was observed for an image with less than 512 x 512 pixels. Using a higher pixel density requires longer computational times. Thus, a balance between intensity losses and computational time was required to determine appropriate sampling size. The intensity value shown has no physical significance. Rather, it was an internal check to ensure the simulations were correct since the total number of electrons should be conserved in elastic scattering. Thus, observation of the total integrated intensity of the electron wave function as it progressed through the specimen was an easy methodology. A loss in total integrated intensity indicates the sampling size in real or reciprocal space was inadequate. Electrons were scattered outside the maximum allowed angle and were effectively lost.

Table 5. 1. The influence of pixel size on CPU time for 4 nm and 20 nm films. Simulations were performed on a 32 bit system with an Intel Atom processor.

	Pixel Size	CPU Time (s)	Intensity
4 nm	128 x 128	3.3	0.91
	256 x 256	10.2	0.93
	512 x 512	40.8	0.985
	1024 x 1024	162.9	0.996
20 nm	128 x 128	24.1	0.58
	256 x 256	59.6	0.71
	512 x 512	190.3	0.92
	1024 x 1024	738.6	0.978

The composition of the simulated film was also shown to be significant in S determination. Figure 5.6 illustrates the ratio of intensities for three compositions for equivalent number of unit cells. Note, as the composition changes, for the same number of fixed unit cells, the lattice parameter changes and causes small deviations in the total thickness between specimens making equivalent thicknesses comparison difficult. In a 4 nm $\text{Fe}_{55}\text{Pt}_{45}$ film, pseudo-sinusoidal oscillations in the ratio of intensities were observed. However, a pseudo-monotonic increase in intensity ratio was observed for the $\text{Fe}_{50}\text{Pt}_{50}$. Finally, the $\text{Fe}_{45}\text{Pt}_{55}$ film exhibits a semi-flat intensity ratio. Clearly, composition has a dramatic effect on the observed intensity ratio as a function of S . If simulations are used to determine the degree of order experimentally, without prior knowledge of the material composition, several computations are required for all possible combinations of the aforementioned parameters. Even then, overlapping intensities between compositions provide points of ambiguity in quantifying the degree of order.

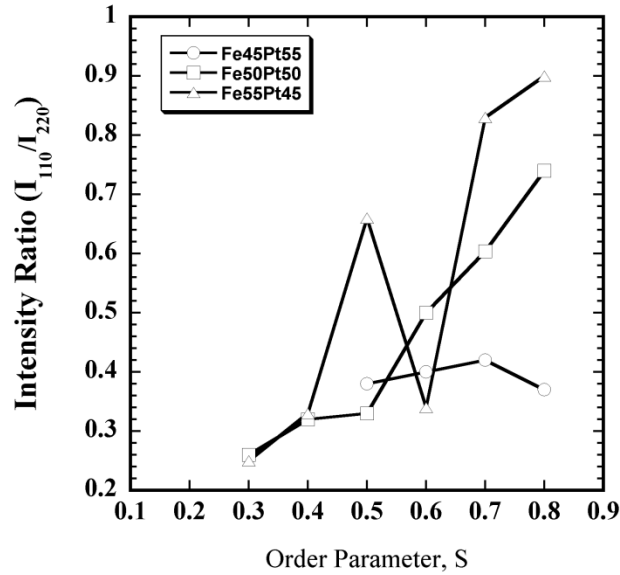


Figure 5. 6. Intensity ratio as a function of S. Three compositions for a 4 nm film are shown.

Orientation effects on the intensity ratio was studied using the {111} orientation. The intensity ratio as a function curves for the optic axis aligned parallel with the $\langle 111 \rangle$ direction and {111} plane normal are plotted in Figure 5.7. The curve associated with aligning the optic axis parallel to the $\langle 111 \rangle$ direction revealed an oscillatory nature. However, the curve associated with alignment to the {111} planes perpendicular to the optic axis exhibits a monotonic increase in the intensity ratio as a function of S.

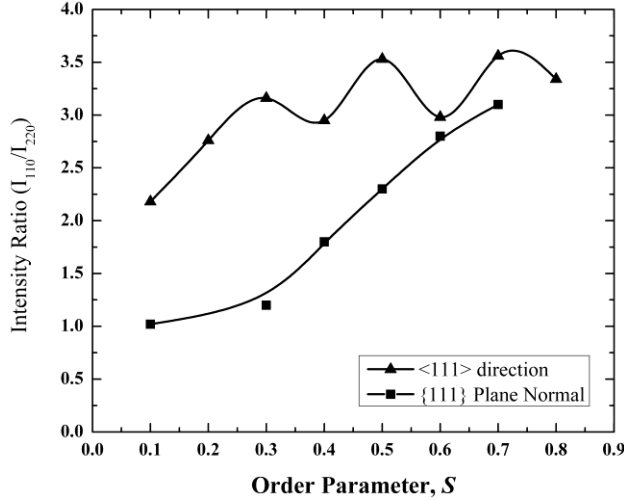


Figure 5. 7. The intensity ratio as a function of S for a 20.4 nm film. The optic axis was aligned with either the $\{111\}$ plane normal or $\langle 111 \rangle$ direction. Oscillations were observed in the shape of the curve for the $\langle 111 \rangle$ direction. The shape of the curve was monotonic in nature with alignment of the optic axis with the $\langle 111 \rangle$ direction.

Thermal effects result in slight shifts of the atoms in and out of the x-y plane, which was the designated slice in z for the simulation. Consequently, several thermal configurations were conducted to acquire an average diffracted intensity. For a 7.2 nm film, five configurations were determined to be the minimum number necessary to sufficiently account for thermal effects. Several simulations were done for $S= 0.2, 0.5,$ and 0.9 for the 7.2 nm film to determine the minimum thermal configurations required. The minimum number was determined by the convergence of the intensity ratio to a constant value per configuration sequence, as seen in Figure 5.8.

The difference in SAED and CBED pattern simulation was the entrance wave function used for propagation through the specimen. In CBED pattern formation, a focused probe was used rather than the plane wave used for SAED patterns. The intensity ratios for the same specimen at a specified S using either technique were similar. Differences in the values were

attributed to processing of the diffraction pattern. In a SAED pattern a single spot was formed for the reflections of interest; whereas in a CBED pattern large disk were formed. Therefore, acquisition of the intensity in an SAED pattern requires little effort. Conversely, CBED intensity ratios require summing the intensity values within a disk. Only the center portion of the disk was summed in this study. Computationally, the SAED was faster when evaluating the intensity ratio. CBED may be required experimentally when determining S from small features. The probe must be converged to interact with only the feature of interest. Experimentally, a user may find SAED work more convenient for S determination when available. Though, the specimen requires constants thickness in the region of interest.

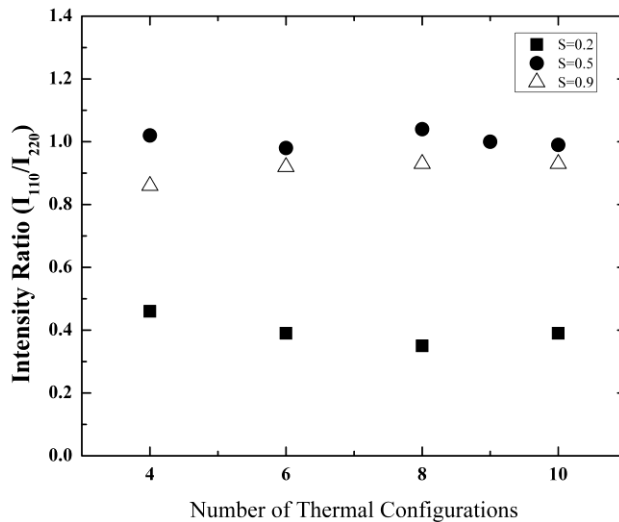


Figure 5. 8. Trends of thermal configurations for $S= 0.2, 0.5,$ and 0.9 for a 7.2 nm film thickness.

5.4 Conclusion

The magnetic property K_u is strongly dependent on the long-range order parameter. Quantification of S in FePt thin films and nanoparticles is essential to the fundamental understanding of these materials. Electron scattering is more amenable for diffraction studies of

small volumes, though the strong interaction of electrons with the thin film results in multiple scattering events. However, S determination is more complex and requires simulations of electron transmission in crystalline specimens including dynamical scattering. A multislice approach was used to simulate CBED patterns of FePt films with various thicknesses, compositions, orientations, and S values. SAED patterns were also simulated to compare with the CBED simulated patterns. The intensity ratios were similar for both diffraction conditions. Processing of the diffraction pattern after simulation was more involved for a CBED pattern than that of an SAED. No trends were found for S in relation to thickness, composition, or orientation. Thus, computation times increase for each unknown parameter. Evaluation of thickness and composition of a film prior to simulation drastically decreases the computation time of the simulation process. Furthermore, evaluating the minimum requirements for pixel size, sampling size, and thermal configurations was necessary to reduce computation times. A comparison of the experimental results to simulations is provided in a subsequent publication.

5.5 References

- [1] D. Weller and M.F. Doerner, Annual Review Material Science 30 (2000) 611.
- [2] S. Mitani, K. Takanashi, M. Sano, H. Fujimori, A. Osawa, and H. Nakajima, Journal of Magnetic Materials, 148 (1995) 163.
- [3] H. Kanazawa, G. Lauhoff, and T. Suzuki, Journal of Applied Physics 87 (2000) 6143.
- [4] S. Okamoto, N. Kikuchi, O. Kitakami, T. Miyazaki, Y. Shimada, and K. Fukamichi, Physical Review B, Condensed Matter 66 (2002) 02 4413-1.
- [5] B.E. Warren, X-ray diffraction Dover, New York, 1990, 208-210.
- [6] R.V. Petrova, R.R. Vanfleet, D. Richardson, B. Yao, and K.R. Coffey, IEEE Transactions On Magnetism 40 (2005) 3202.
- [7] R.V. Petrova, R.R. Vanfleet, D.R. Richardson, B. Yao, and K.R. Coffey, Microscopy Microanalysis 11 (2005) 782.

- [8] E.J. Kirkland, *Advanced Computing in Electron Microscopy*, New York: Plenum (1998).
- [9] J.M. Cowley and A.F. Moody, *Acta Crystallographica* 10 (1957) 609.
- [10] J.M. Cowley and J.C.H. Spence, *Ultramicroscopy* 3 (1979) 433.
- [11] D.E. Laughlin, K. Srinivasan, M. Tanase, and L. Wang, *Scripta Materialia* 53 (2005) 383.
- [12] S. Yuasa, H. Miyajima, and Y. Otani, *Journal of the Physical Society of Japan* 63 (1994) 3129.
- [13] R.J. Joseyphus, K. Shinoda, Y. Sato, K. Tohji, and B. Jeyadevan, *Journal of Material Science* 43 (2008) 2402.
- [14] K. Barkmak, J. Kim, D.C. Berry, W.N. Hanani, K. Wierman, E.B. Svedberg, and J.K. Howard, *Journal of Applied Physics* 97 (2005) 024902-1.
- [15] J. Lyubina, O. Isnard, O. Gutfleisch, K.-H. Müller, and L. Schultz, *Journal of Applied Physics* 100 (2006) 094308-1.
- [16] A.R. Denton and N.W. Ashcroft, *Physics Review A* 43 (1991) 3161.

CHAPTER 6

COMPARISON OF SIMULATED AND EXPERIMENTAL ORDER PARAMETERS IN FEPT⁵

Abstract

Quantification of order parameter in FePt thin films and nanoparticles is essential in the fundamental understanding of the material. The magnetocrystalline anisotropy constant K_u is dependent on the long-range order parameter S . Traditional analysis methods for determining S in ultra thin films are not adequate for quantification of the parameter. However, electron diffraction is sufficiently sensitive to collect diffraction information from thin films and nanoparticles. The strong interactions of electrons with even small volumes result in multiple scattering events. This requires the implementation of multislice simulations to determine order parameter. In this study, eight specimens are analyzed to determine the viability of electron diffraction for S quantification.

⁵ A manuscript has been prepared for the work in this chapter for publication in *Microscopy and Microanalysis* as: K.L. Torres, R.R. Vanfleet, and G.B. Thompson, "Comparison of simulated and experimental order parameters in FePt."

6.1 Introduction

In our previous paper, the simulation conditions and resultant diffracted intensity outputs as a function of degree of long-range order, S , composition, thickness, orientation and thermal effects in $L1_0$ FePt were addressed. Simulations were required to determine the order parameter in electron diffraction because of the dynamical diffraction events [1]. Validation of simulations was essential in assessing the viability of electron diffraction in the quantification of order parameter.

Thin films provide ideal systems to perform these controlled experiments. The crystallographic orientation can be controlled through proper substrate selection, the degree of order can be controlled by the annealing temperature during or post growth, and the composition controlled by the rate of sputtering from elemental targets. Collectively, this provides the tunable variables to study the conditions that contribute to the variations observed in the dynamical electron diffraction events.

Although an order parameter was determined through comparison of simulation and experimental results, to assess the results and validate the approach, the order parameter was compared to an independent measurement. X-ray diffraction, because of its simplicity in determining order parameter, was adopted. Experimental X-ray diffraction intensities from small volumes can be difficult to quantify because of the low diffracted intensities. This concern can be reduced or eliminated by using a synchrotron source.

In this paper, eight different specimens at various orientations, thicknesses, compositions and order parameters were used to compare experimental electron diffraction intensity ratios to simulated values. The results were then compared to X-ray diffraction to assess the electron diffraction-based methodology.

6.2 Materials and Methods

6.2.1 Specimen Preparation

Fe_xPt_{1-x} (where x = 50 to 55) thin films were co-sputter deposited using commercially pure elemental Fe and Pt targets in an AJA ATC 1500-F chamber. Prior to deposition, the sputter chamber was evacuated to a base pressure of $< 6 \times 10^{-6}$ Pa. Ultra-high purity Ar was flowed into the chamber at 10 standard cubic centimeters per minute to a pressure of 0.27 Pa to serve as the working gas for sputtering. To promote the [001] or [111] orientation of the thin film, an MgO $<001>$ or MgO $<111>$ substrate was heated at an elevated temperature during deposition. In a similar manner, a single Fe₅₀Pt₅₀ film was deposited onto a Si $<001>$ substrate at room 300K. Post deposition, several films were annealed in an Ar/4%H₂. The parameters for deposition and *ex-situ* annealing for the eight specimens used in this work were tabulated in Table 6.1.

Table 6. 1. The nominal compositions and thicknesses for the FePt films used in this study. The substrate temperature, T_s, the *ex situ* annealing temperature, T_A and time were also tabulated.

Specimen ID	Thickness (nm)	Composition (at %)	Substrate Material	T _s (K)	T _A (K)	Anneal Time (min)
Specimen A	7.1	Fe ₅₅ Pt ₄₅	MgO $<001>$	673	873	30
Specimen B	7.7	Fe ₅₄ Pt ₄₆	MgO $<001>$	773	873	30
Specimen C	11.7	Fe ₅₀ Pt ₅₀	MgO $<001>$	773	873	30
Specimen D	11.7	Fe ₅₀ Pt ₅₀	MgO $<001>$	773	1073	30
Specimen E	14.2	Fe ₅₁ Pt ₄₉	MgO $<111>$	773	--	--
Specimen F	18.6	Fe ₅₁ Pt ₄₉	MgO $<001>$	773	873	30
Specimen G	21.1	Fe ₅₁ Pt ₄₉	MgO $<111>$	773	--	--
Specimen H	21.1	Fe ₅₁ Pt ₄₉	Si $<001>$	300	873	60

Transmission electron microscopy (TEM) foils were prepared by ultrasonically cutting 3 mm discs using a SiC abrasive. The discs were then mechanically ground to approximately 120 μm and subsequently dimple polished using 3 μm diamond paste to a final thickness of 15 μm. Each sample was cleaned sequentially in acetone and methanol prior to ion beam thinning. The

foil was ion milled in a Gatan PIPS at 4.0 keV from the substrate side of the specimen until perforation and/or electron transparency. The milling process produces holes which have tapered thicknesses around the edge. This can contribute to uncertainty in the film thickness from which the diffraction was acquired. To alleviate this issue in the MgO specimens, the foil was placed in phosphoric acid at 315 K [2]. The acid dip etched the MgO substrate leaving pits where the intact film covered the pit or window, as shown in Figure 6.1. To stop the acid etching, the specimen was dipped in distilled water followed by an ethanol rinse.

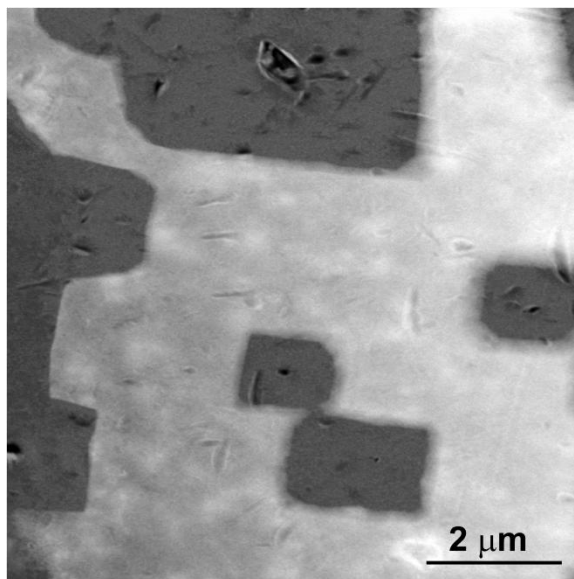


Figure 6. 1. STEM image of intact regions of FePt film surrounded by the MgO substrate. The MgO windows are etched with hot phosphoric acid.

6.2.2 *Experimental Methods*

As noted in the preceding simulation-based paper, knowledge of the film's composition and thickness were required for order parameter determination. The film thicknesses, tabulated in Table 6.1, were determined from cross-sectional foils, prepared by focus ion beam (FIB) milling in a dual beam FEI Quanta 3D FIB [3]. The cross-sections were analyzed in an FEI Tecnai F20 (S)TEM operated at 200 keV. The foil was tilted down the $\langle 010 \rangle$ MgO zone axis to

ensure the film thickness measurement was taken edge on. The film thicknesses were in agreement with the projected thicknesses determined by the sputtering deposition rates. The composition of each film was confirmed by Rutherford backscattering spectrometry (RBS) and was in agreement with the compositions determined by the individual sputtering rates of each elemental target, see Table 6.1. The convergent-beam electron diffraction (CBED) patterns taken down the respective zone axis of the MgO specimens was in the plan-view imaging orientation using the Tecnai F20 (S)TEM at 200 keV. The spherical aberration coefficient C_s for the instrument at this accelerating voltage was 1.35 mm. A convergence semi-angle, α , of 4 mrad was focused on the specimen to obtain the CBED pattern at a camera length of 200 mm. This semi-convergence angle was chosen to give the minimal overlap between the diffracted disks as shown in Figure 6.2. Prior to collecting SAED patterns from the Si specimen, a scanning TEM-XEDS Pt-L and Si-K intensity line profile was used to confirm constant thickness [4], as seen in Figure 6.3. The x-ray absorption in the film of Pt was negligible since the atomic number of Pt was larger than that of Fe. The location where the Pt-L line was flat was an indication of a region with constant thickness [5]. This region was selected for the diffraction study. The SAED patterns collected from the MgO specimen were taken from regions with film windows. To reduce the thermal contributions to the background level intensity during the experiment, the specimens were cooled in a Gatan double-tilt cryoholder to 94 K. The CBED patterns were recorded using a 1k charge-coupled device (CCD) camera using an integration time of 0.5 seconds. Images were later quantitatively analyzed. The selected area electron diffraction (SAED) pattern intensities were captured and quantified using Ditabis imaging plates.

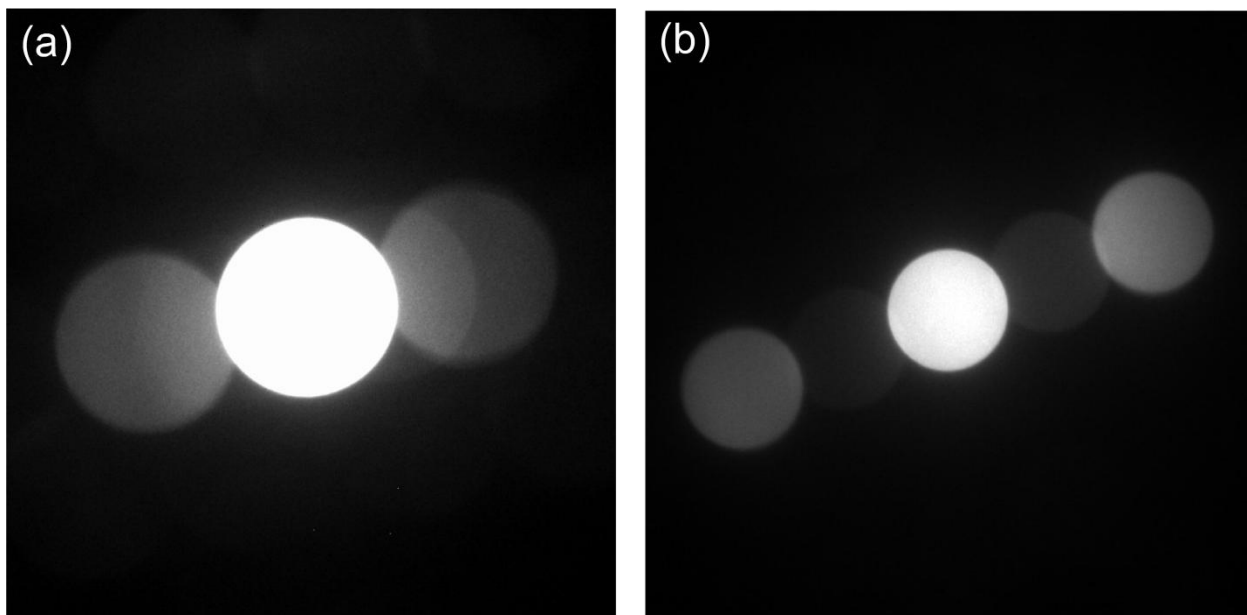


Figure 6. 2. (a) CBED patterns with overlapping disks where the semi-convergence angle was greater than 4 mrad. (b) CBED patterns without overlapping disks with a semi-convergence angle of 4 mrad.

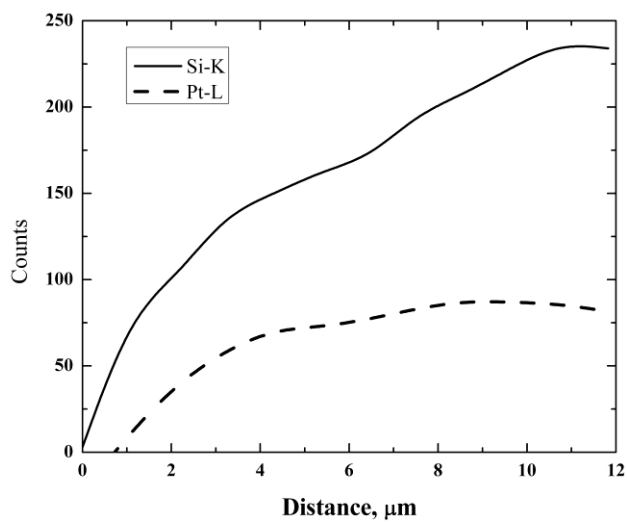


Figure 6. 3. The Si-K line and Pt-L line plotted as a function of distance. The Si-K was plotted with a solid line and the Pt-L line was plotted with a dashed line.

The long-range order parameter, S , measures the degree of chemical order and is given by

$$S = r_\alpha + r_\beta - 1 = \frac{r_\alpha - x_A}{y_\beta} = \frac{r_\beta - x_B}{y_\alpha} \quad (1)$$

where x_A and x_B are the atom fractions of the two components, y_α and y_β are the fraction of the lattice site types α and β in the ordered structure, and r_α and r_β are the fraction of each type of lattice sites occupied by the correct type of atom [6]. In x-ray diffraction, the kinematical nature of the scattering allows the integrated intensity ratio of the superlattice-to-fundamental reflections to be directly measured and compared to the theoretical intensities, which are readily available from JCPDS cards. To eliminate the possibility of texture contributions, the superlattice and fundamental reflections were taken in the same direction, i.e. [110] and [220], in this study. As eluded to previously, for small volumes, the x-ray scattering intensities can be difficult to measure using standard laboratory-based diffractometers. Thus, the XRD order parameter was obtained using the National Synchrotron Light Source at Brookhaven National Laboratory in a Bragg-Brentano orientation.

Unlike x-rays, electrons scatter much more strongly and can be more amenable to acquiring diffracted intensities from small volumes. However, the strong interaction because of dynamical effects makes the S obtained by the integrated intensity ratio incorrect. To account for the multiple scattering events, the multislice method as described by Kirkland [1] was used to simulate CBED patterns to predict the intensities for a given order parameter, thickness, and composition, as noted in the preceding Paper I. The (110) superlattice and (220) fundamental electron diffracted reflections (I_{110}/I_{220}) were acquired experimentally to estimate the S value of $L1_0$ FePt thin films. The experimentally determined intensity ratio was then compared to

simulated intensity ratios to determine the order parameter. These results were then verified with traditionally determined order parameter by XRD described above.

The experimental parameters of thickness, composition, orientation, lattice parameter, and temperature, for each film were assigned to the multislice simulation inputs. The simulation parameters of the number of unit cells (sampling size), pixel size, and number of thermal configurations were also assigned. For all specimen data, four thermal configurations and a pixel size of 512 x 512 were used to produce the simulated patterns. These parameters reduced computational time and mitigated intensity losses. For the simulated CBED patterns, a focused probe with a semi-convergence angle of 4 mrad was used as the initial wave function entering the specimen. The SAED patterns were simulated using a plane wave function rather than the focused probe. Thermal effects were included using the frozen phonon approximation [1]. Each atom was given a random displacement based on the Debye-Waller factors of Fe and Pt found in the international table for X-ray crystallography [7]. The root-mean-square displacement amplitude σ of 0.14 as determined by Barmak *et al.* [8] was used in this work. The final diffraction pattern was the intensity averaged over several thermal configurations of atoms with different random offsets.

6.3 Results and Discussion

A complex dependence of the I_{110}/I_{220} ratio on specimen thickness was observed for $L1_0$ FePt in the [001] orientation as shown in Figure 6.4. This dependence was observed in specimens A and B. An experimental intensity ratio of 0.53 ± 0.04 for specimen A and 0.52 ± 0.03 was estimated after the background subtraction of the images in Figure 6.5. From the simulations of specimen A in Figure 6.5(c), the order parameter was 0.19 ± 0.01 . Whereas, in Figure 6.5(d) the simulated results for the order parameter of specimen B was of 0.43 ± 0.07 .

The order parameter S was determined from where the measured intensity ratio crossed the simulated curve. The simulated CBED patterns for the two specimens were shown in Figure 6.6. Although the intensity ratio was the same for the two specimens, the estimated order parameter was dissimilar because of the difference in thickness of the specimen. This was an example that clearly demonstrates the importance of accurate thickness measurements as an input parameter for the simulation to determine the order parameter; intensity ratio values were not individually indicative of the order parameter in the film. In this case, the films differed in thickness by less than 1 nm. The intensity ratio as a function of S curve was also dissimilar for the two specimens. Oscillations at $S > 0.4$ were observed for specimen A. However, a monotonic curve was observed for specimen B. These results were verified by the traditional x-ray diffraction methods conducted at Brookhaven National Laboratory. The order parameter for specimen A was 0.1 ± 0.03 and 0.43 ± 0.01 for specimen B.

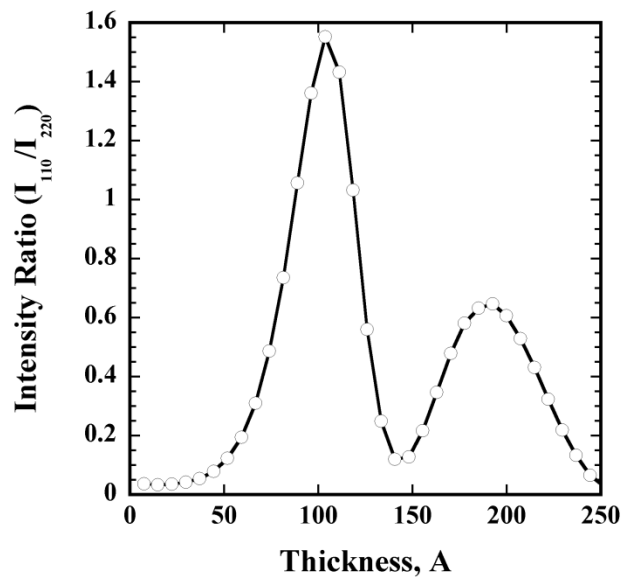


Figure 6. 4. Intensity ratio as a function of thickness for [001] orientation for $S=0.3$.

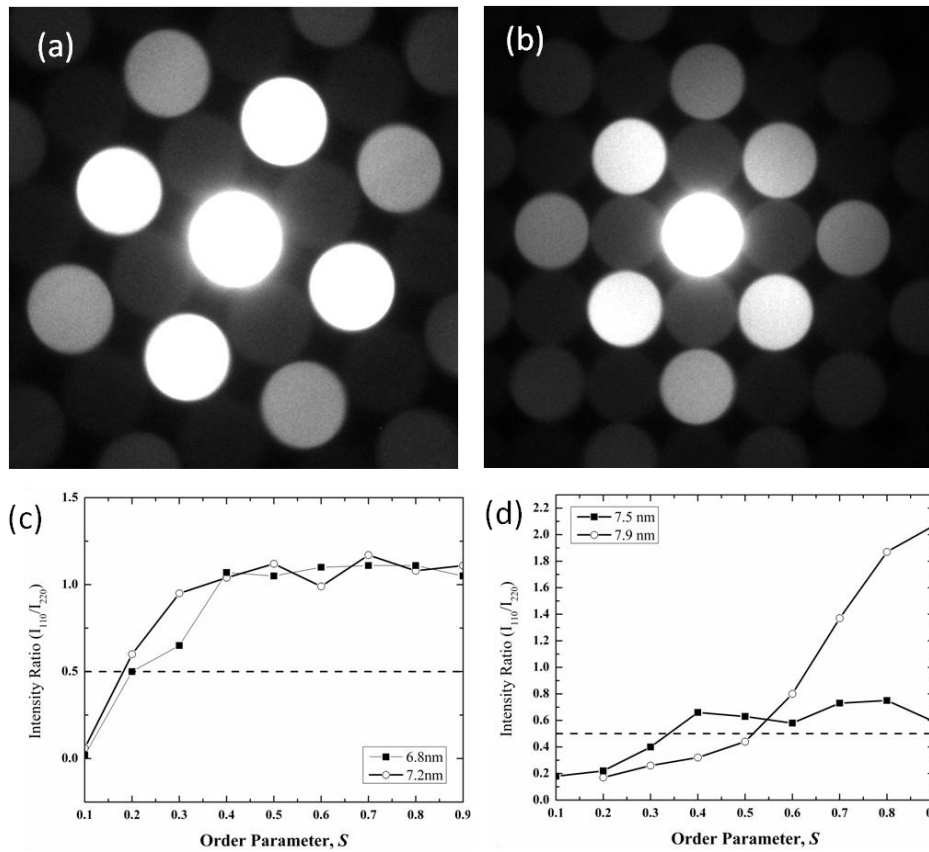


Figure 6. 5. The Experimental CBED patterns for (a) specimen A and (b) specimen B. The intensity ratio as a function of S for (c) specimen A and (d) specimen B. The dashed line indicates the experimentally obtained intensity ratio for the specimen. The curves were determined by multislice simulations.

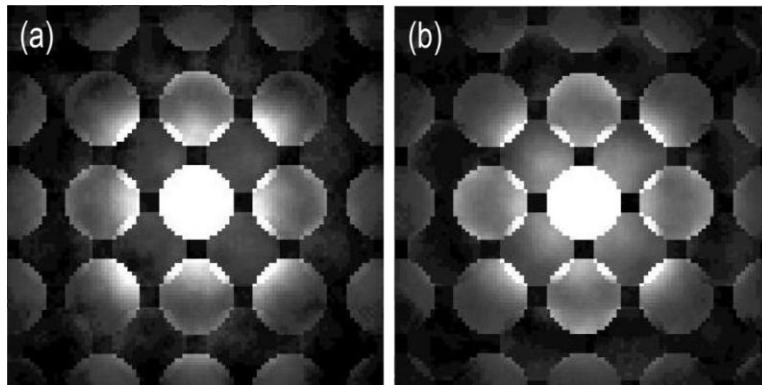


Figure 6. 6. The simulated CBED patterns for (a) specimen A at $S=0.2$ and (b) specimen B at $S=0.4$.

The simulated I_{110}/I_{220} intensity ratio as a function of order parameter (S) in Figure 6.7 illustrates the dependence of the intensity ratio on the specimen thickness close to the measured thickness. Small oscillations of the intensity ratio were observed for $S < 0.5$. Conversely, at $S > 0.7$, large deviations of S were observed. The oscillations arise from the complex nature of the electron scattering where the diffracted beams are dynamically scattered between the multiple diffraction peaks. The experimental intensity ratio for each specimen was estimated after background subtraction of the images in Figures 6.8(a) and 6.8(b). For specimen C, the intensity ratio was 0.6 ± 0.08 and for specimen D it was 1.34 ± 0.4 . In Figure 6.7, the simulated results associated with the thickness measurement error limits for the 11.7 nm mean thickness film were plotted. For this specimen, the experimental order parameter was 0.48 ± 0.02 . For the same specimen, the order parameter was increased by annealing it *ex situ* for a longer time. For this particular condition, this resulted in an increase in the intensity ratio with an experimentally determined order parameter of 0.61 ± 0.03 . The values were in good agreement with XRD determined S values of 0.46 ± 0.03 for specimen C and 0.59 ± 0.01 for specimen D. Furthermore, the change in order parameter resulted in fewer oscillations in this order parameter region, as seen in Figure 6.7.

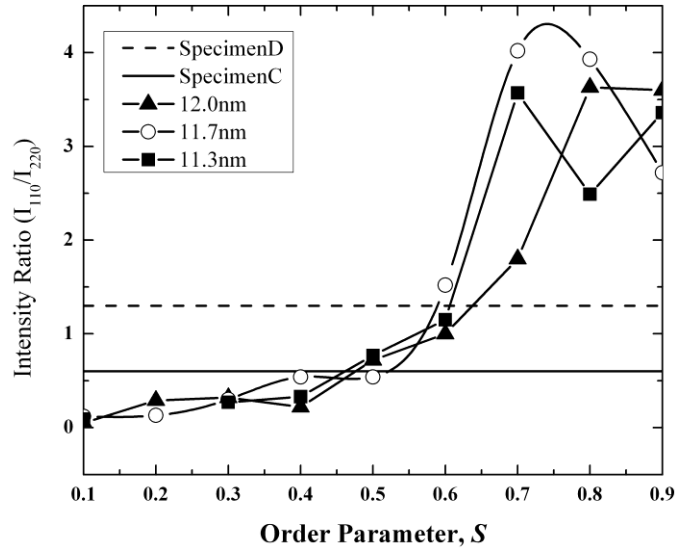


Figure 6. 7. Intensity ratio as a function of S , determined by multislice simulation, for specimens C and D. Three film thicknesses close to the film thickness are shown to account for error in measurement. The horizontal lines correspond to experimentally obtained intensity ratios.

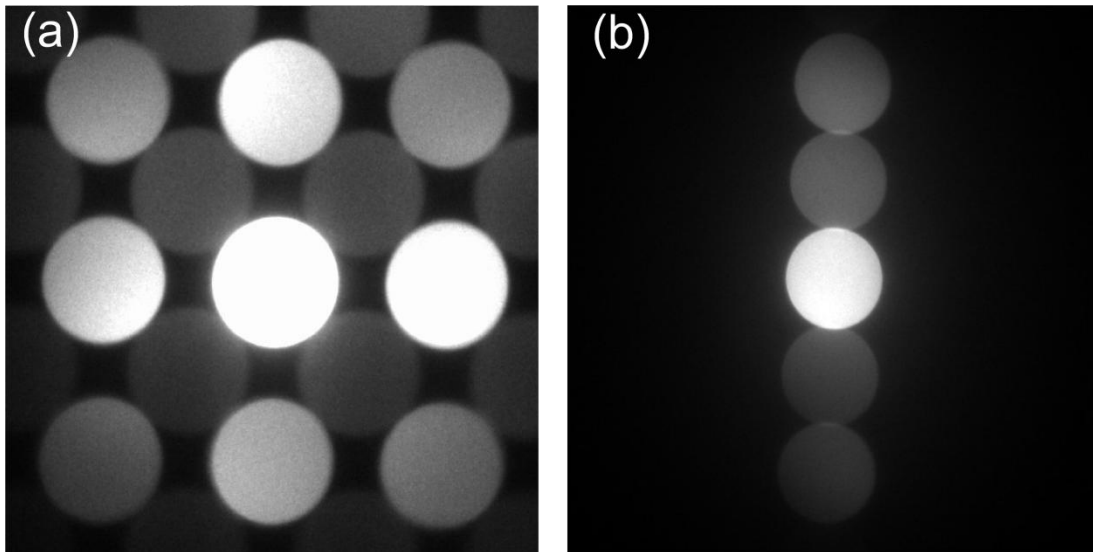


Figure 6. 8. An experimental CBED pattern for (a) specimen C and (b) specimen D.

The simulation results of Paper I showed that the shape of the intensity ratio curve as a function of S depended on the thickness, order parameter, and orientation of the film. In the case of LI_0 FePt, the slicing scheme also played a role in the shape of the curve in the $\langle 111 \rangle$

orientation. In the preceding paper [9], two slicing schemes were presented for this orientation in the tetragonal crystal structure. One slicing scheme aligned the optic axis parallel with the $\langle 111 \rangle$ direction while the other aligned the optic axis perpendicular to the $\{111\}$ planes (see Figure 6.9). Both simulated orientations were compared to experimentally collected CBED patterns in this work. In Figure 6.10, the simulated curves for the two orientation options were shown bounded by the error associated with the experimental thickness measurements. The curves associated with aligning the optic axis parallel to the $\langle 111 \rangle$ direction in Figure 6.10(a) for this thickness and composition revealed the oscillatory nature observed previously with the $[001]$ orientation. Additionally, the frequency of the oscillation changed over the thickness limit values plotted. However, the curve associated with alignment to the $\{111\}$ planes perpendicular to the optic axis, Figure 6.10(b), exhibited a monotonic increase in the intensity ratio as a function of S . The intensity ratio estimated of specimen E from the experimentally collected CBED pattern was 4.4 ± 0.84 . Because of the oscillatory nature observed in the simulated results obtained with $\langle 111 \rangle$ direction, the intensity ratio crosses two S values hence giving an order parameter range from 0.4 to 0.6 for this film. The monotonic nature of the $\{111\}$ plane orientation narrowed S between 0.53 and 0.57. This difference in the range of S was contributed to the plane tilt in the two orientations. Alignment of the $\{111\}$ planes perpendicular to the optic axis were more amenable to the multislice method. In this orientation, the atomic planes were flat in-depth which was favorable for slicing the specimen appropriately. Furthermore, the monotonic nature of this orientation provides higher confidence in the order parameter estimate using CBED patterns. The results of traditional x-ray analysis estimated an $S = 0.58 \pm 0.02$.

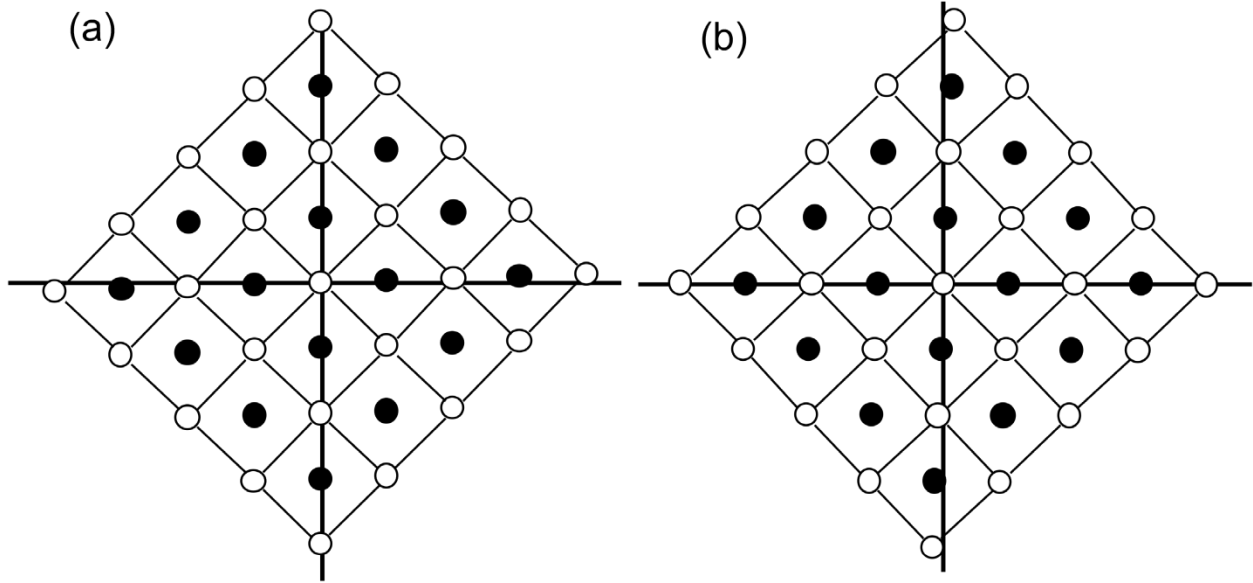


Figure 6.9. Possible slicing schemes for the (111) orientation. **(a)** The optic axis is aligned with the [111] direction. Note the atoms align in-depth for this orientation. However, the atomic layers are tilted. **(b)** The optic axis is aligned perpendicular to the (111) planes. The atomic layers are flat along the optic axis. However, the atoms do not align in-depth.

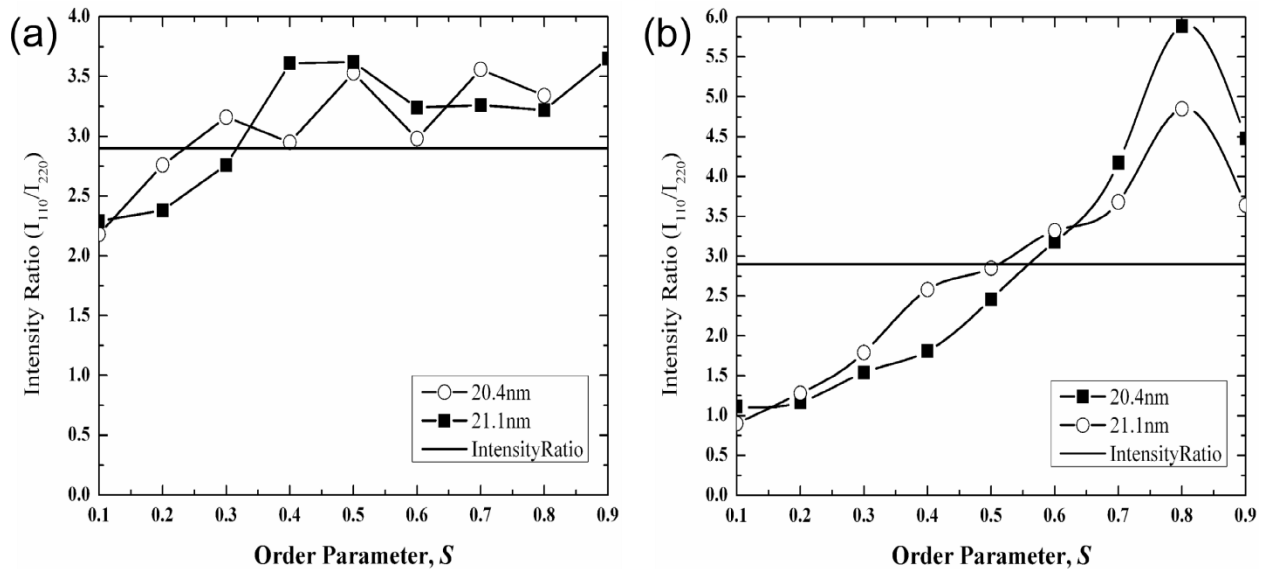


Figure 6.10. The intensity ratio as a function of S for specimen E with the optic axis **(a)** along the [111] direction and **(b)** perpendicular to the (111) planes.

Now consider the case of a film with near equivalent order parameters but different orientations. Specimen F has a film thickness of 18.6 nm and an experimental intensity ratio of 0.82 ± 0.23 . The order parameter determined from the simulated results in Figure 6.11(a) was $S=0.47 \pm 0.01$, which was in good agreement with the X-ray estimate $S=0.5 \pm 0.01$. Specimen G was 21.1 nm thick with an experimental intensity ratio of 2.39. From simulation CBED patterns in Figure 6.11(b), the estimate of S was 0.43 ± 0.05 . This was in agreement with the X-ray determined S of 0.5 ± 0.02 . Although the specimens have similar order parameters, the intensity ratios are significantly different, 0.82 vs. 2.39. The difference was contributed to the orientation and thickness of the films reiterating the importance of these parameters in the simulations.

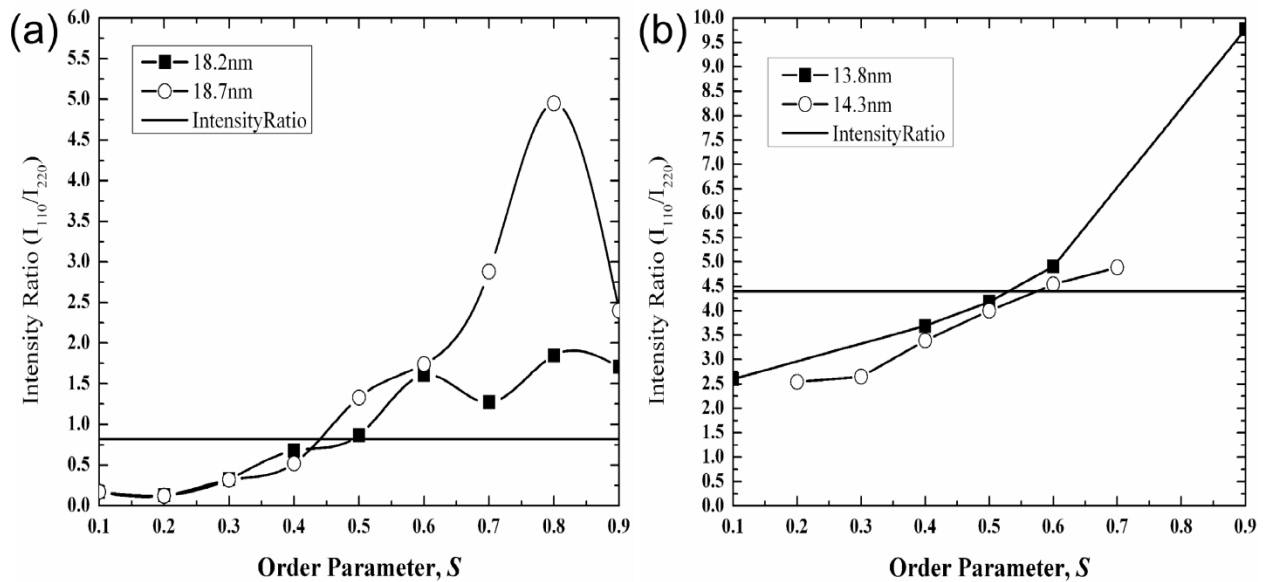


Figure 6. 11. The intensity ratio as a function of S for (a) specimen F and (b) specimen G. The curves were determined by multislice simulations.

Finally, a comparison of simulated and experimental selected area electron diffraction patterns was performed. The SAED patterns for specimen F and specimen H in Figure 6.12 illustrate the challenge of using these conditions. The intensity contributions from the single

crystal substrates saturate the images. The estimated intensity ratio of 0.23 was taken away from the single crystal reflections. This intensity ratio corresponded to an $S=0.23 \pm 0.02$. For specimen H, an intensity ratio of 0.86 corresponded to an $S=0.3 \pm 0.01$. Although the simulation process was straightforward for SAED patterns, experimentally the acquisition of these patterns proved more challenging than CBED. The larger region of interest for SAED patterns incorporated the effects of the substrate for both specimen B and specimen H. The use of a small focused probe on a region of interest was more amenable to quantifying S in this study.

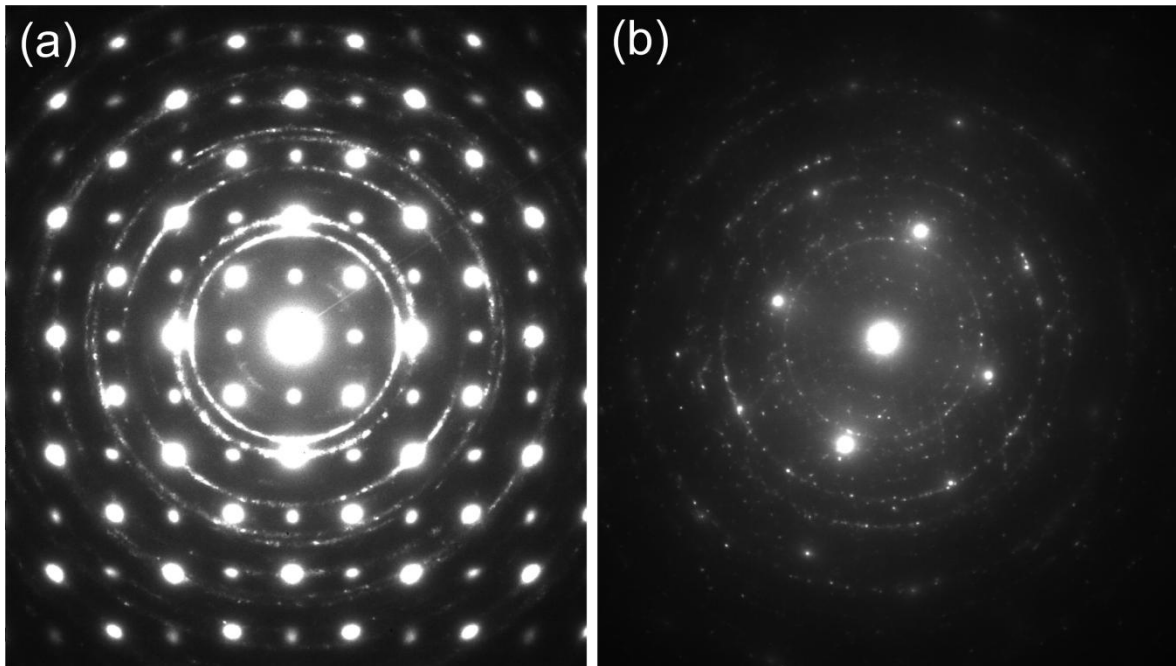


Figure 6. 12. (a) The experimental SAED pattern for specimen F. The pattern included reflections from the FePt film and MgO substrate. (b) The experimental SAED pattern for specimen G with reflections from the FePt film and Si substrate.

6.4 Conclusions

The complexities of electron scattering limit the ability to obtain order parameter by taking the ratio of total integrated peak intensities of the superlattice and fundamental reflections. However, order parameter was attainable through electron diffraction provided the parameters of

thickness, composition, and orientation were available for multislice simulations. A method for order parameter determination for $L1_0$ FePt thin films was presented. In this study, eight films were analyzed to assess the viability of electron diffraction for order parameter estimates. For the seven specimens analyzed with CBED conditions, the order parameter as determined by electron diffraction closely matched the order parameter as determined by the traditional methodology. However, the two specimens analyzed by SAED conditions did not reproduce the same results. The effects of substrate contributions experimentally hindered the ability to accurately quantify the intensity values of the superlattice and fundamental reflections. It should be noted, the exact shape of the simulated curves depends most significantly on the orientation and thickness of the specimen. A different zone axis or an off-axis orientation had a significant effect on the simulated results. In this low symmetry crystal, the complexity of the multislice method was increased in the $\{111\}$ orientation. Evaluation of the intensity ratio curve as a function of S was necessary to determine the confidence in order parameter. The oscillatory behavior exhibited in several films constrained the ability to measure order parameter. In general, electron diffraction provides a technique to determine order parameter of small volumes through the implementation of multislice simulations.

6.5 References

- [1] E.J. Kirkland, *Advanced Computing in Electron Microscopy*, Plenum, New York, 1998.
- [2] J.K. Ferrer, M.T. Johnson, J. Bentley, and C.B. Carter, *Surface Science* 587 (2005) 205.
- [3] L.A. Giannuzzi, J.L. Drown, S.R. Brown, R.B. Irwin, and F.A. Stevie, *Microscopy Research and Technique* 41 (1998) 285.
- [4] Y. Inaba, K.L. Torres, A. Cole, R.R. Vanfleet, R. Ott, T. Klemmer, J.W. Harrell, G. B. Thompson, *Journal of Magnetism and Magnetic Materials* 321 (2009) 2451.

- [5] M. Watanabe and D.B. Williams, *Journal of Microscopy* 221 (2006) 89.
- [6] B.E. Warren, *X-ray diffraction*, Dover, Mineola, 1990, p. 209.
- [7] C. MacGillavary and G. Rieck (Eds.), *International Tables for X-ray Crystallography*, Kynoch, Birmingham, 1962, vol III.
- [8] K. Barmak, J. Kim, L.H. Lewis, K.R. Coffey, M.F. Toney, A.J. Kellock, J.-U. Thiele, *Journal of Applied Physics* 98 (2005) 033904-1.
- [9] K.L. Torres, R.R. Vanfleet, and G.B. Thompson, (Unpublished results).

CHAPTER 7

CONCLUSIONS AND FUTURE WORK

The characterization of nanostructured materials to understand the structure-property relations is essential to the advancement of these materials in several applications. Subtle compositional fluctuations within a nanostructure can significantly influence the material properties. In this work, microanalysis techniques have been used to quantify composition, volume fraction, and long-range order parameter in magnetic nanostructures. Key findings are discussed in subsequent sections.

7.1 Data binning in atom probe tomography

In this work, the influence of voxel dimension on the volume fraction and composition of chemically partitioned phases was examined. A methodology for determining an optimal voxel dimension range was developed by using a model system for the experimental data set. The composition and volume fraction were determined from an experimental nanocomposite using this method. A breakdown of the analysis was observed at edge lengths of 0.6 nm or smaller because the large error in composition determination within the voxel. At voxel edge lengths of 2.2 nm or greater, errors in composition are observed because of a loss in fidelity identification of the interface. These errors result in incorrect phase compositions and erroneous volume fractions as determined by the lever rule. The APT determined volume fraction was compared to

a dark-field TEM analysis of the experimental crystallites and a compositional based lever rule approach. The optimized voxel length was in good agreement with the APT results. To extend this work, more complex model systems can be used to refine the methodology presented for a binary alloy.

7.2 Grain boundary enrichment

Electron diffraction and atom probe tomography was used to understand the influence of Pt enrichment at grain boundaries in the A1 to $L1_0$ polymorphic phase transformation in a series of $\text{Fe}_{54\pm 1}\text{Pt}_{46\pm 1}$ film. The as-deposited A1 phase indicated a preferential segregation of Pt to the grain boundaries of 2σ above that of the nominal 46 at.% Pt concentration within the film. This enrichment of Pt at the grain boundaries is in agreement to modeling predictions for Pt surface segregation. The atom probe data sets provide experimental verification of these modeling predictions. Upon phase transforming to $L1_0$, the Pt grain boundary enrichment decreased. The extent of Pt depletion from the grain boundaries was dependent upon the annealing times and temperatures, with longer times and higher temperatures resulting in less Pt at the boundary.

7.3 Field evaporation behavior of [001] FePt

Field ion microscopy and atom probe tomography were used to investigate the field evaporation behavior of the (001) planes in ordered FePt. During field evaporation, it was found that close to the (002) pole, the number density of Fe ions detected was significantly lowered because of ion trajectory aberration effects. Simulations incorporating a face center cubic structure have qualitatively reproduced the experimental findings without the inclusion of a

binding term or thermal effects. Both experimental and simulation results have shown that the difference in evaporation field between the two components of the alloy contributed to the trajectory aberrations near the (002) pole and zone axes. The modeled system used in this paper has shown that chemical order within a structure introduces aberrations in the reconstruction of the atomic planes limiting the spatial and chemical fidelity of characterizing such structures using current reconstruction methodologies. This work could be extended by changing the material phase to the ordered $L1_2$ Fe₃Pt intermetallic. The crystal structure would be changed from tetragonal to cubic. The influence of chemical composition and crystal structure on field evaporation of an intermetallic could be investigated with this alloy. Furthermore, thermal effects could be included in the simulation algorithm for field evaporation. The results of this addition could be compared to DC evaporation and laser assisted evaporation conditions. To improve reconstructions, the development of new algorithms is necessary to reduce the aberrations observed.

7.4 Electron diffraction order parameter determination

A comparison of the experimental results to simulations was used to assess the viability of electron diffraction in the quantification of S in FePt thin films and nanoparticles. Electron scattering is more amenable for diffraction studies of small volumes, though the strong interaction of electrons with the thin film results in multiple scattering events. However, S determination is more complex and requires simulations of electron transmission in crystalline specimens including dynamical scattering. A multislice approach was used to simulate CBED patterns of FePt films with various thicknesses, compositions, orientations, and S values. SAED patterns were also simulated to compare with the CBED simulated patterns. The intensity ratios

were similar for both diffraction conditions. Processing of the diffraction pattern after simulation was more involved for a CBED pattern than that of an SAED. No trends were found for S in relation to thickness, composition, or orientation. Thus, computation times increase for each unknown parameter. Evaluation of thickness and composition of a film prior to simulation drastically decreases the computation time of the simulation process. Furthermore, evaluating the minimum requirements for pixel size, sampling size, and thermal configurations was necessary to reduce computation times.

Eight specimens were analyzed in this study. For the seven specimens analyzed with CBED conditions, the order parameter as determined by electron diffraction closely matched the order parameter as determined by the traditional methodology. However, the two specimens analyzed by SAED conditions did not reproduce the same results. The effects of substrate contributions experimentally hindered the ability to accurately quantify the intensity values of the superlattice and fundamental reflections. It should be noted, the exact shape of the simulated curves depends most significantly on the orientation and thickness of the specimen. A different zone axis or an off-axis orientation had a significant effect on the simulated results. In this low symmetry crystal, the complexity of the multislice method was increased in the $\{111\}$ orientation. Evaluation of the intensity ratio curve as a function of S was necessary to determine the confidence in order parameter. The oscillatory behavior exhibited in several films constrained the ability to measure order parameter. In general, electron diffraction provides a technique to determine order parameter of small volumes through the implementation of multislice simulations. The electron diffraction studies presented can be extended to other intermetallic materials such as CoPt and AlMn. Off-axis orientations could be investigated to determine the robustness of the multislice simulation technique.

REFERENCES

- [1] M.A. Willard and M. Daniil, Nanostructured Soft Magnetic Materials, in : J.P. Liu, E. Fullerton, O. Gutfleisch, and D.J. Sellmyer (eds.), *Nanoscale Magnetic Materials and Applications*, Springer Science+ Business Media, New York, 2009, 373- 398.
- [2] P.R. Ohodnicki Jr., Y.L. Qin, D.E. Laughlin, M.E. McHenry, M. Kodzuka, T. Ohkubo, K. Hono, and M.A. Willard, *Acta Materialia* 57 (2009) 87.
- [3] K. Barmak, J. Kim, D.C. Berry, W.N. Hanani, K. Wierman, E.B. Svedberg, and J.K. Howard, *Journal of Applied Physics* 97 (2005) 024902-1.
- [4] X.H. Li, B.T. Liu, W. Li, H.Y. Sun, D.Q. Wu, and X.Y. Xhang, *Journal of Applied Physics* 101 (2007) 093911-1.
- [5] K.L. Torres and G.B. Thompson, *Ultramicroscopy* 109 (2009) 606.
- [6] R. Petrova, R.R. Vanfleet, D. Richardson, B. Yao, and K.R. Coffey, *IEEE Transactions on Magnetism* 41 (2005) 3202.
- [7] R. Goswami and M.A. Willard, *Scripta Materialia* 59 (2008) 459.
- [8] S. Joshi, S.D. Yoon, A. Yang, N. X. Sun, C. Vittoria, V.G. Harris, R. Goswami, M. Willard, and N. Shi, *Journal of Applied Physics* 99 (2006) 08F115-1.
- [9] C. Srivastava, G.B. Thompson, J.W. Harrell, and D.E. Nikles, *Journal of Applied Physics* 94 (2006) 054304.
- [10] Y. Inaba, K.L. Torres, A. Cole, R.R. Vanfleet, R. Ott, T. Klemmer, J.W. Harrell, G. B. Thompson, *Journal of Magnetism and Magnetic Materials* 321 (2009) 2451.

- [11] T.J. Klemmer, C. Liu, N. Shukla, X.W. Wu, D. Weller, M. Tanase, D.E. Laughlin, and W.A. Soffa, *Journal of magnetism and magnetic materials* 266 (2003) 79.
- [12] T.F. Kelly and M.K. Miller, *Review of Scientific Instruments* 78 (2007) 031101.
- [13] M.P. Moody, L.T. Stephenson, A.V. Ceguerra, and S.P. Ringer, *Microscopy Research and Technique* 71 (2008) 542.
- [14] E.A. Marquis and F. Vurpillot, *Microscopy and Microanalysis* 14 (2008) 561.
- [15] B.E. Warren, *X-ray diffraction*, Dover, Mineola, 1990, 209.
- [16] H. Xu, H. Heinrich, and J.M.K. Wiezorek *Intermetallics* 11 (2003) 963.
- [17] B. Zhang and W.A. Soffa *Scripta Metallurgica* 30 (1994) 683.
- [18] T.J. Klemmer, D. Hoydick, H. Okumura, B. Zhang, and W.A. Soffa, *Scripta Metallurgica et Materialia* 33 (1995) 1793.
- [19] E.J. Kirkland, *Advanced Computing in Electron Microscopy*, Plenum Press, New York (1998).
- [20] M.E. McHenry and D.E. Laughlin, *Acta Materialia*. 48 (2000) 223.
- [21] R. Skomski, *Journal of Physics: Condensed Matter* 15 (2003) R841.
- [22] K. Watanabe, M. Kashiwagi, S. Kawashima, Y. Ono, Y. Yamashita, C. Yamazaki, M. Hanadam, T. Inoue, M. Taniguchi, Y. Okumra, and K. Sakamoto, *Nuclear Fusion* 46 (2006) S332.
- [23] J. Numazawa and H. Ohshima, *Journal of Magnetism and Magnetic Materials* 176 (1997) 1.
- [24] M. Mallary, A. Torabi and M. Benakli, *IEEE Transactions on Magnetism* 38 (2002) 1719.
- [25] D. Weller, A. Moser, L. Folks, M.E. Best, W. Lee, M.F. Toney, M. Schwickert, J.U. Thiele, and M.F. Doerner, *IEEE Transactions on Magnetism* 36 (2000) 10.
- [26] C.-M. Kuo, P.C. Kuo, and H.-C. Wu, *Journal of Applied Physics* 85 (1999) 2264.
- [27] D.E. Laughlin, K. Srinivasan, M. Tanase, and L. Wang, *Scripta Materialia* 53 (2005) 383.
- [28] B. Yang, M. Asta, O.N. Mryasov, T.J. Klemmer and R.W. Chantrell, *Scripta Materialia* 53 (2005) 417.
- [29] R.V. Chepulskii and W.H. Butler, *Physical Review B* 72 (2005) 134205.
- [30] C. Srivastava, J. Balasubramanian, C. Turner, J. Wiest, H. Bagaria, and G. Thompson, *Journal of Applied Physics* 102 (2007) 104310-1.

- [31] W.A. Soffa and D.E. Laughlin, *Acta Materialia* 37 (1989) 3019.
- [32] Y.K. Takahashi and K. Hono, *Scripta Materialia* 53 (2005) 403.
- [33] P.G. Shewmon, *Transformations in Metals*, J. Williams Book Co. (1983) 267-274.
- [34] R.F.C. Farrow, D. Weller, R.F. Marks, M.F. Toney, S. Hom, G.R. Harp, and A. Cebollada, *Applied Physics Letters* 69 (1996) 1166.
- [35] D.A. Porter and K.E. Easterling, *Phase Transformations in Metals and Alloys*, CRC Press, Boca Raton (2004) 98.
- [36] B. Gault, M.P. Moody, F. de Geuser, G. Tsafnat, A. La Fontaine, L.T. Stephenson, D. Haley, and S.P. Ringer, *Journal of Applied Physics* 105 (2009) 034913-1.

APPENDICES

APPENDIX A
MULTISLICE SIMULATION GUIDE

The following steps are necessary to form a diffraction pattern using Kirkland's multislice algorithm [19]. The use of Matlab and c prompt are required to complete these steps.

1. Crystal description

The crystal description is formed in Matlab using the file MKXYZseriesS1.m and the following input parameters:

Input filename: The base file for the crystal oriented in the [001]
FePtL10base.xyz

Unit cell: These are experimentally determined lattice parameters for the crystal
a=3.86 c= 3.73 for FePt

Desired atomic fraction for the highest Z element: This can incorporate composition
X=0.50

Order parameter: The desired order parameter for the crystal
S=0.50

Normal direction: The plane normal aligned parallel with the optic axis
0 0 1

X direction: The direction should be orthogonal to the plane normal designated
1 0 0

X,Y,Z supercell size = This is the size of the supercell of the crystal

Repeats of z supercell = The thickness of the crystal to be simulated

Output filename: The filename for the final crystal description
FePtXX

If 10 Z supercells were required to generate the crystal thickness, the output file of the final crystal will be FePtXX10.xyz

2. Electron Probe

Two choices for an electron probe are possible. Either a plane wave function can be chosen to simulate selected area electron diffraction (SAED) patterns or a focused wave function can be chosen to simulate a convergent-beam electron diffraction (CBED) pattern. If a CBED pattern is needed the following steps are necessary to form the probe:

C:\TEMSIM > Probe

Name of file to get focused probe wave function: Test

Desired size of output image in pixels: 512 512

Size of output image in Angstroms ax,by: 40 40

Beam voltage in kilovolts: 200

Spherical aberration in mm (measured experimentally): 1.35

Defocus in Angstrom (Scherzer conditions): 700

Aperture in mrad (semi-convergence angle): 4

Type 1 for smooth aperture: 0

Probe position in Angstroms: 20 20

If a SAED pattern is required the electron probe is a wave function and will be implemented in the autoslic algorithm which will be described in the subsequent section.

3. Multislice algorithm

The following steps will generate the exit wave function that can be Fourier transformed into the diffraction pattern. First, a plane wave function will be demonstrated. This will be followed by the implementation of a focused wave function.

C:\TEMSIM > autoslic

Name of file with input atomic potential in x,y,z format: (The final crystal description from 1.)

FePtXX10.xyz

Replicate unit cell by NCELLX,NCELLY,NCELLZ: (If the supercell was originally generated in Matlab the unit cell will not need to be increased here.)

1 1 0

Name of file to get binary output of multislice result: FePtout.tif

Do you want to include partial coherence (y/n) : n

Do you want to start from previous result (y/n) : n (for SAED)

Incident beam energy in kev: 200

Wavefunction size in pixels, Nx,Ny: 512 512

Crystal tilt x,y in mrad.: 0 0

Slice thickness (in Angstroms this should be an atomic layer in z): 1.851

Do you want to record the (real,imag) value of selected beams vs. thickness (y/n) : n

Do you want to include thermal vibrations (y/n) : y

Type the temperature in degrees K (experimental parameter): 100

The parameters for the generation of a CBED pattern. A focused wave function is used.

C:\TEMSIM > autoslic

Name of file with input atomic potential in x,y,z format: (The final crystal description from 1.)

FePtXX10.xyz

Replicate unit cell by NCELLX,NCELLY,NCELLZ: (If the supercell was originally generated in Matlab the unit cell will not need to be increased here.)

1 1 0

Name of file to get binary output of multislice result: FePtout.tif

Do you want to include partial coherence (y/n) : n

Do you want to start from previous result (y/n) : y (for CBED)

Name of file to start from: Test

Crystal tilt x,y in mrad.: 0 0

Slice thickness (in Angstroms this should be an atomic layer in z): 1.851

Do you want to record the (real,imag) value of selected beams vs. thickness (y/n) : n

Do you want to include thermal vibrations (y/n) : y

Type the temperature in degrees K (experimental parameter): 100

4. Image Formation

The formation of the diffraction pattern (SAED or CBED) requires the use of the image program written by Kirkland.

C:\TEMSIM > image

Name of file with input multislice result:

feptout.tif

Type 0 for coherent real space image,
or 1 for partially coherent real space image,
or 2 for diffraction pattern output:

2

Name of file to get diffraction pattern:

Feptdiff.tif

Several thermal configurations are necessary to incorporate thermal effects in the experiment. After each thermal configuration has been transformed into an image the images must be summed and averaged. This is completed with the sumpix program.

C:\TEMSIM > sumpix

Type number of input image files (this is an example):

2

input 0 : feptdiff1.tif

input 1 : feptdiff2.tif

Type name of output file: feptdiffsum.tif

Do you want to display on log scale (y/n) : n

Do you want to convert to a power spectra (y/n): n

Finally, the image must be processed in the display program. This will be the final image used to evaluate the intensities.

C:\TEMSIM > sumpix

The available image output modes are:

1 print single (1D) line of image data as text

2 ASCII text file of 2D image

3 postscript (EPS) greyscale in file

4 postscript (EPS) contour plot in file

Enter code number: 2

Name of file that has binary data to display: feptdiffsum.tif

Name of output file: feptdiffsum

5. Intensity Ratio Evaluation

The intensity ratio is evaluated in Matlab. The final output file is loaded in Matlab. For CBED patterns, the intensity of the superlattice and fundamental reflections are summed over the entirety of the disk. For a SAED pattern the spot for each reflection is identified and this is the intensity for the reflection.

APPENDIX B

EXPERIMENTAL CBED PATTERNS

The following procedure outlines how to obtain CBED patterns experimentally in the Tecnai TEM F20 operating in (S)TEM mode.

- 1.** Align the beam in standard TEM mode at an accelerating voltage of 200keV. The C_2 aperture is at aperture location 1, the smallest aperture available. The alignment of the C_2 is critical in obtaining quality CBED patterns. Thus, manually center the aperture on the screen at 34,000 X magnification. Converge the beam to crossover and center the beam. Then defocus the beam until the C_2 aperture is visible on the screen. Again, manually center the aperture on the screen. This process is repeated until the beam converges and diverges around the center of the screen.
- 2.** After the C_2 aperture is aligned, correct for astigmatism in the C_2 . The condenser stigmators are used to correct for the distortion in the beam. To begin, underfocus the beam so the effect can be seen. Then adjust the stigmators so the image becomes circular. Next go through crossover and overfocus the beam. If the image is not circular, again adjust the stigmators. Repeat this process until the image is circular on both sides of crossover.
- 3.** Next, find the eucentric plane. This is important for reproducing the experiment. During this step also find the zone axis for the experiment.
- 4.** Open Tia and Digital Micrograph.
- 5.** In the Tecnai user window highlight the STEM button in the STEM Imaging window as shown in Figure B.1.

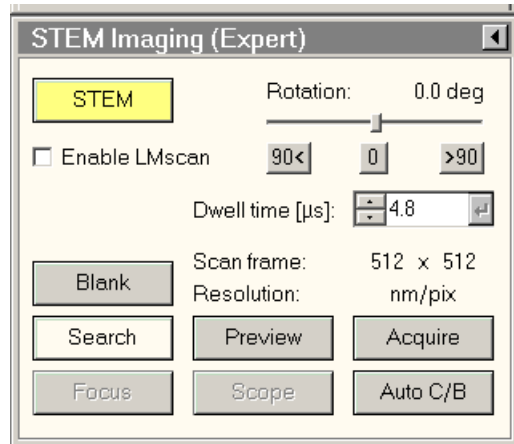


Figure B.1. The STEM button is highlighted in yellow. This button is toggled to activate and deactivate STEM mode in the Tecnai F20.

6. Next, select the FEG register for a (S)TEM probe of spot size nine.

7. Alignment of the C_2 is essential for the experiment. The physical location of the aperture is aligned in step 1. However, the astigmatism is different for (S)TEM mode than for TEM mode. To properly align the C_2 , deselect diffraction on the user interface. Increase the magnification to 400 kX. Next use the focus knob on the user interface to converge the beam to create a halo with a bright spot in the center. Use the condenser stigmators to make the halo circular. A diagram is provided in Figure B.2a to demonstrate the proper shape of the probe. If the halo is circular, but the hot spot is off centered as shown in Figures B.2b and B.2c the physical location of the C_2 aperture should be adjusted to place the hot spot in the center of the illuminated halo.

8. After adjusting the condenser stigmators to form a symmetric probe, the image is focused. This procedure is performed in the standard (S)TEM mode. Images of the region of interest should be taken. As shown in Figure B.3 the disks of the CBED pattern overlap in the standard conditions for the FePt crystal at 200 keV and the smallest aperture available on the Tecnai F20.

To decrease the semi-convergence angle and separate the disks, a non-standard mode is required. The following steps allow for the non-standard operation of the Tecnai F20.

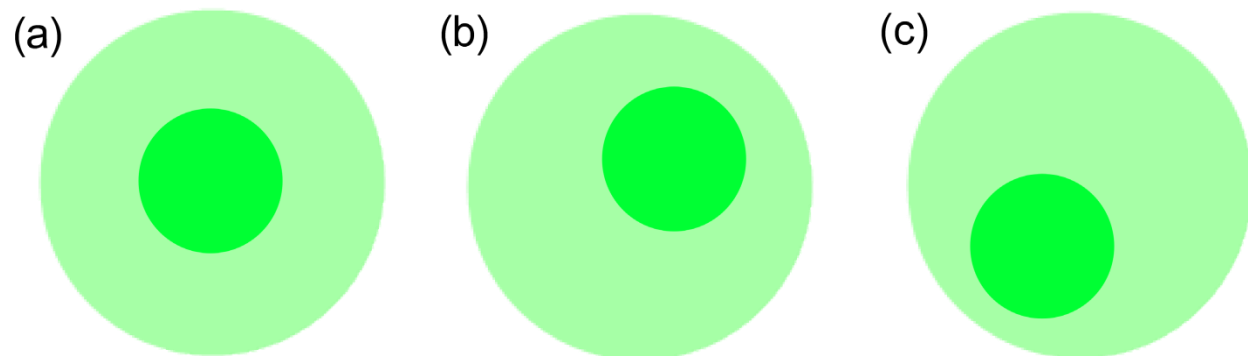


Figure B.2. (a) Proper alignment of the probe with the hot spot located at the center of the circular halo. (b) An example of a misaligned aperture. The illuminated halo is symmetric. (c) Another example of a misaligned aperture. The probe is astigmatic with a circular halo.

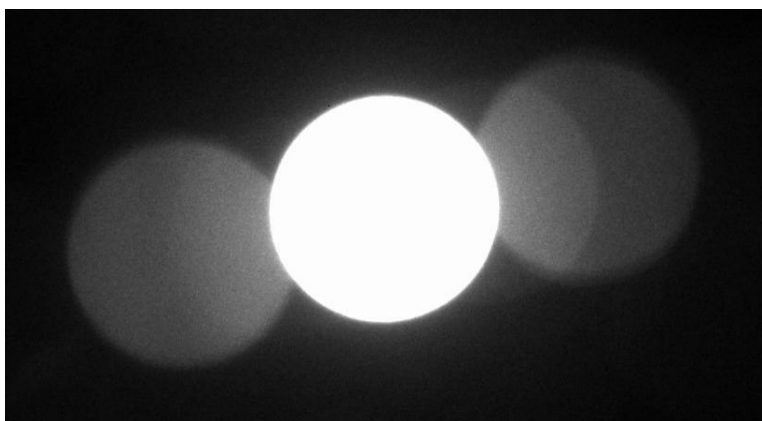


Figure B.3. An example of aCBED pattern where the reflection disks overlap.

9. In the STEM Imaging tab, select the flap-out tab in Figure B.4 outlined by the red box. Under the focus tab, select the drop-down list *Focus using*, highlighted in blue in Figure B.4. In standard operating conditions Intensity is used. However, for the non-standard operating conditions Intensity and Objective are needed.

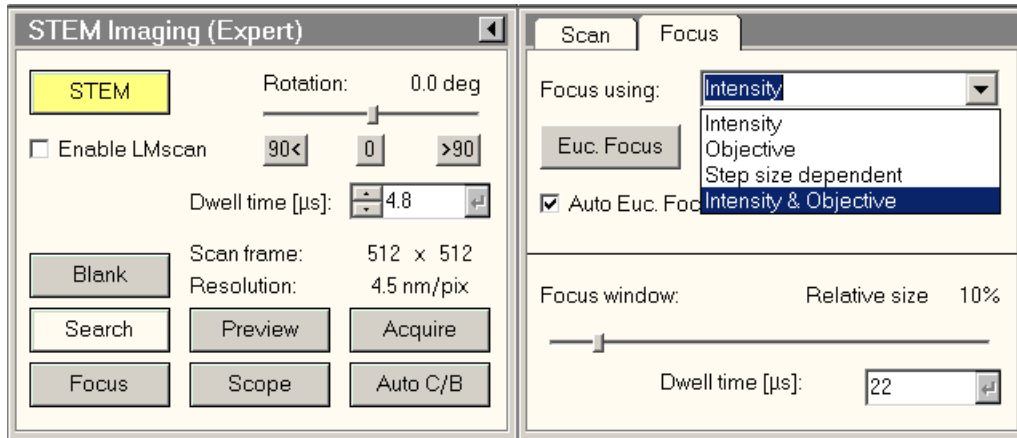


Figure B.4. The flap-out tab is used to change the operating conditions from standard to non-standard. Under the focus tab, the Intensity & Objective focus is selected for non-standard operation.

10. In the non-standard conditions, the focus and intensity knobs should be used to adjust the size of the disks. For FePt at these operating conditions, the C_2 is set to 40% and the Objective is at 99%. The STEM image should be focused. Condenser stigmatism may be required after finding the appropriate C_2 and objective settings to obtain separated disks.

11. A camera length of 200 mm was used for these experiments. Caution should be used when changing the camera length. A change in camera length can increase the intensity on the CCD camera and could result in permanent damage of the CCD camera.

12. Prior to collecting a CBED pattern, the Search button in the STEM imaging window shown in Figure B.4 should also be toggled off. This will stop the scanning of the probe across the surface of the specimen. The HAADF detector should also be removed to view more of the pattern on the CCD camera. This is done by toggling the HAADF yellow button in Figure B.5. The button should turn gray when the detector is removed. To obtain an averaged CBED pattern over an area, use the focus box located in the STEM imaging window. The box can be placed over the region of interest.

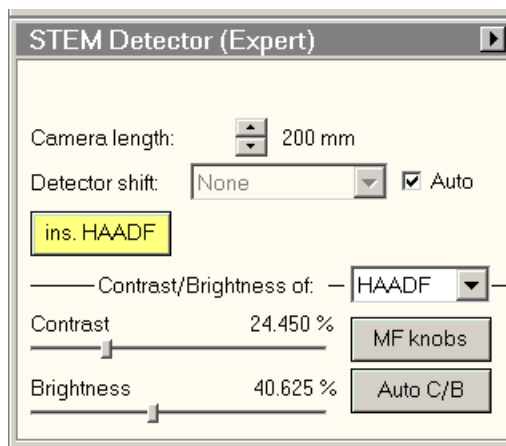


Figure B.5. The STEM detector tab controls the insertion and removal of the HAADF detector. The button highlighted in yellow is toggled to perform this process. The camera length can also be changed in this tab.

Prior to acquiring a CBED pattern on the CCD camera, the three options for image acquisition should be considered. Search, preview, and acquisition are three imaging choices. Search is a low resolution option and should be used initially with a short integration time (~0.1 sec) for only a single frame. This will mitigate the possibility of damaging the camera. If the counts for the central disk are sufficiently low, a single frame can be taken with a longer integration time in acquire mode. This will increase the intensity and the resolution. The increase of the integration time depends on the intensity from the search image. The intensities should not be more than 10,000 counts.

13. Before collecting a CBED pattern with the CCD camera, an image with the phosphorous screen down at the integration times selected for search and acquisition mode should be taken. This will be the reference for the next image taken. This step should be performed before each acquisition.

14. After the patterns are collected, save the pattern in the dm3 file format. This will maintain the quantitative intensity information with the image. The intensity values within a disk are summed using the digital micrograph analysis tools.

APPENDIX C

ATOM PROBE TOMOGRAPHIC RECONSTRUCTION

The following steps are for the reconstruction of an atom probe tomography data set when crystallographic information (i.e. poles) is visible in the event histogram. The procedure follows steps similar to Gault *et al.* [36].

- 1.** Open the RHIT file to start the reconstruction in Imago's visualization and analysis software (IVAS).
- 2.** Proceed to the detector event histogram. Click in the region within the red box shown in Figure C.1. This will bring up the Select Hit Class dialog box. Check the unsample data box to display all the events detected during the acquisition of the data.
- 3.** The x- and y- coordinates of the visible major poles need to be identified. This is achieved by placing the cursor over each pole. The corresponding x- and y- coordinates will be displayed below the event histogram. This region is highlighted blue in Figure C.1. A minimum of 3 poles not on the same zone axis should be identified for a proper reconstruction.
- 4.** The diagram in Figure C.2 is created to identify the poles throughout the reconstruction process. The x- and y- coordinates for the poles are tabulated in Table C.1. The distance and angle between pole 1 and each pole is also tabulated.

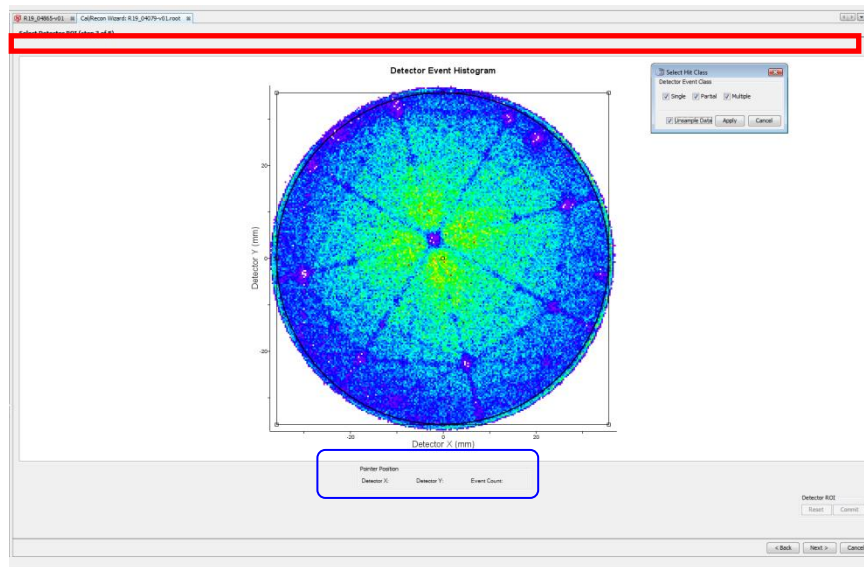


Figure C.1. The detector event histogram for an Al specimen. The region highlighted in red will allow a user to unsample the data. This will display all events detected during acquisition. The region highlighted in blue displays the x- and y- coordinates of the cursor position.

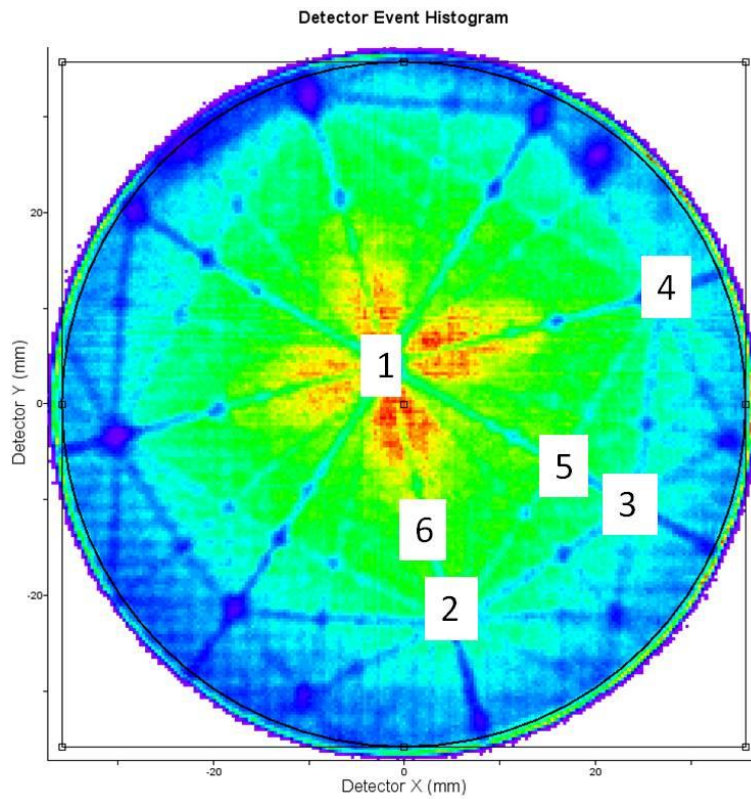


Figure C.2. A diagram of the poles where the x- and y- coordinates were identified.

Table C.1. The x- and y- coordinates for each pole identified from the detector event histogram. The distance and angle between pole 1 and the other poles are also tabulated.

Pole Number	X mm	Y mm	Distance mm	Angle deg.
1	-2.02	4.06		
2	5.04	-22.06	27.0573	16.7327
3	23.53	-10.57	29.4421	18.1147
4	26.56	11.54	29.5426	18.1725
5	16.14	-6.34	20.9272	13.0900
6	2.35	-13.17	17.7755	11.1725

5. After the coordinates of the major poles have been identified, proceed to the reconstruction explorer in Step 7 of 8 in IVAS. This is an advanced option located at the bottom of the display which is highlighted red in Figure C.3.



Figure C.3. Step 7 of 8 display with the reconstruction explorer highlighted by the red box.

6. Once in the reconstruction explorer, enter the x and y position of a pole in the detector portion of the display highlighted by a red box in Figure C.4. Also in this area, reduce the outer radius to

a value between 2 and 5 mm. At this time, the ion sequence range should be set to 100%. The X and Y projection center values highlighted by a blue box should be set to the pole center values. After entering the appropriate values generate the z- spatial distribution map (SDM). The initial value of 1.65 for the image compression factor (ICF) and 3.3 for K are used to generate the first SDM. An SDM should be generated for each pole identified. This is done by inserting the appropriate values for the X and Y centers. The plane spacing for each pole identified is tabulated in Table C.2.

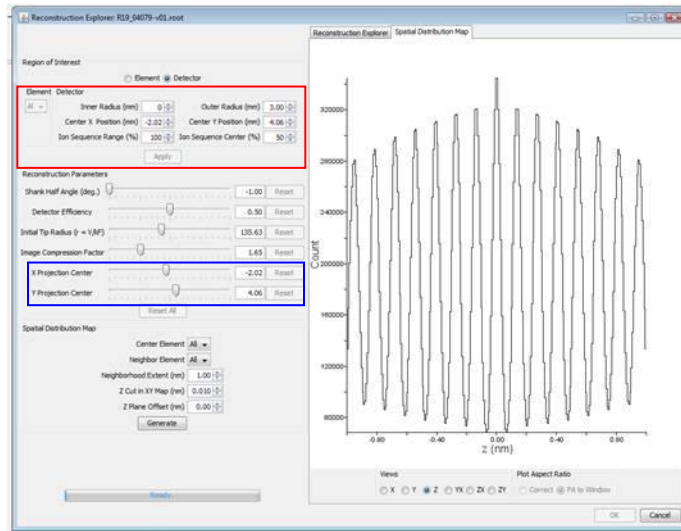


Figure C.4. The z-SDM for an ICF value of 1.65 and a value of 3.3 for K . The spacing for Pole 1 is 0.135 nm for these reconstruction values.

Table C.2. The plane spacing for each pole using the initial values for ICF and K are tabulated. The pole combination used for this sample is also provided. The theoretical angle between the 002 pole and each pole identified is given along with the new calculated ICF value.

Pole Number	Pole	d-spacing nm	θ_{theory} deg.	θ_{observed} deg.	ICF
1	(002)	0.137			
2	(311)	0.0908	25.2	16.7	1.51
3	(420)	0.0704	26.6	18.1	1.47
4	(31 $\bar{1}$)	0.096	25.2	18.2	1.39
5	(620)	0.0464	18.4	13.1	1.41
6	(511)	0.0544	15.8	11.2	1.41

7. The orientation of the sample is next identified. Stereographic projections of the crystal system should be used for this step. Table C.2 demonstrates the potential pole combination for this sample. The calculated angles between pole 1 and all other poles are also tabulated.

8. An ICF value is calculated by taking the ratio of the theoretical angle and the observed angle. An averaged ICF value of 1.43 from Table C.2 is used to calculate a new plane spacing for each pole in the reconstruction explorer. The new plane spacing, d_1 , for each pole is tabulated in Table C.3. The ratio between the theoretical and observed d-spacing for the (002) pole is 0.088. This value is used to calculate the adjusted d-spacing shown in Table C.3. A new K value, K_1 , is calculated from

$$K_1 = \sqrt{\frac{d_{theory}}{d_1}} K_0 \quad (C.1)$$

where K_0 is the most recent K value used and d_1 is the last d-spacing calculated. For this iteration the initial value for K is used. Note no values are reported for pole 5 and 6. This is because an SDM is not available at the pole after adjusting the ICF value.

Table C.3. The d-spacing observed using the new ICF value of 1.43 and corresponding K is tabulated along with the theoretical value for the pole.

Pole Number	Pole	d_{theory} nm	d_1 nm	K_1	d_2 nm	K_2
1	(002)	0.2024	0.1784	3.52	0.1844	3.51
2	(311)	0.1221	0.1192	3.34	0.1232	3.34
3	(420)	0.0906	0.0920	3.27	0.0952	3.27
4	(31 $\bar{1}$)	0.1221	0.1256	3.25	0.1302	3.24
5	(620)	--	--	--	--	--
6	(511)	--	--	--	--	--

9. The averaged K value of 3.35 is taken from Table C.3. The d-spacing, d_2 , of each pole is calculated using a value of 1.43 for ICF and the new K_1 . Step 8 is reiterated to obtain K_2 . These

values are tabulated in Table C.3. Eventually, the value for K will converge. This is achieved after 2 iterations in this sample. This may vary from sample to sample. The final SDM for the (002) pole is shown in Figure C.5.

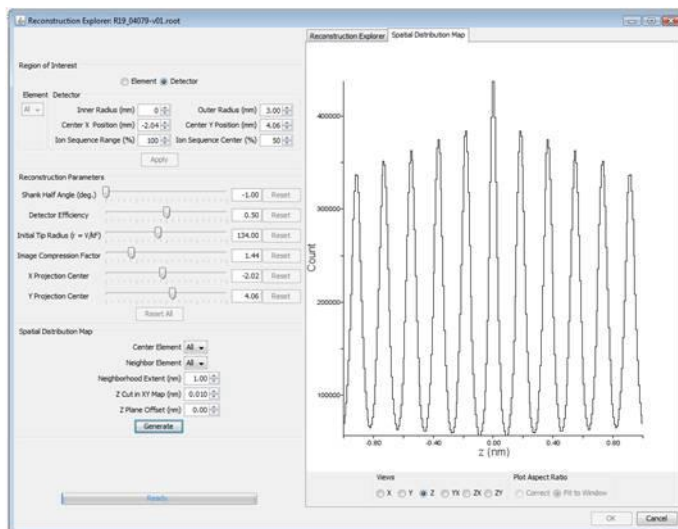


Figure C.5. The final SDM for the (002) pole using a value of 1.43 for ICF and 3.35 for K .

10. A small cube, Figure C.6, is extracted after completing the reconstruction wizard. The image illustrates the visualization of planes at a pole.

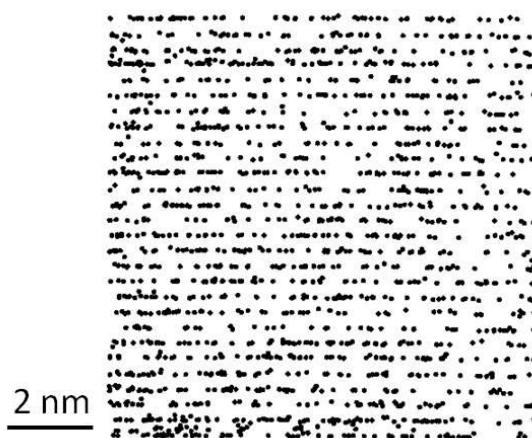


Figure C.6. The figure is an extracted cube from the (002) pole to illustrate the visualization of planes at the (002) pole.